

Copyright
by
Evan Paul Perillo
2017

**The Dissertation Committee for Evan Paul Perillo Certifies that this is the approved
version of the following dissertation:**

**Nonlinear Microscopy Methods for Imaging and Particle Tracking in
Thick Biological Specimen**

Committee:

Andrew Dunn, Supervisor

Hsin-Chih “Tim” Yeh, Co-Supervisor

Thomas Milner

Yuebing Zheng

**Nonlinear Microscopy Methods for Imaging and Particle Tracking in
Thick Biological Specimen**

by

Evan Paul Perillo, B.S.M.E

Dissertation

Presented to the Faculty of the Graduate School of

The University of Texas at Austin

in Partial Fulfillment

of the Requirements

for the Degree of

Doctor of Philosophy

The University of Texas at Austin

May 2017

Dedication

I dedicate this dissertation to my family, Marcella, and my French bulldog Leopold.

Acknowledgements

I would like to thank my advisor Dr. Andrew Dunn, and co-advisor Dr. Tim Yeh for their invaluable guidance and advice throughout my graduate study. They always provided an open discussion about research ideas, no matter how unlikely or farfetched the idea. In addition, they allowed me to forge my own path and take risks with ambitious projects. Without their advising, I would have not been able to carry through with any of the major accomplishments and publications of this study. I would like to thank the other two members of my committee, Dr. Thomas Milner and Dr. Yuebing Zheng, for their helpful comments and advice during my study that improved the quality of this work.

Thanks to all of my lab members in both Dunn and Yeh labs for their help throughout my research. I am especially grateful for Allen Liu and all of the hard work be put into the cell culture and sample preparation for my work. His constant motivation, positive thinking pushed me to work hard and overcome obstacles in research. I am also thankful for the help and knowledge of Cong Liu on the topic of Single Particle Tracking. Thanks to Dr. Jeremy Jarrett, David Miller and Dr. Flor Medina for their help and discussions with in vivo two-photon microscopy. I would like to thank my whole team of undergraduate researchers over the years; Khang Hyunh for his work on TSUNAMI, Justin McCracken for his work on the ytterbium fiber oscillator, Daniel Fernée, John Goldak, and Andrei Bonteanu for their work on the ytterbium fiber amplifier and the diamond Raman laser. Thanks to Phyllis Ang for her ongoing work with dual particle tracking TSUNAMI. I would also like to thank my summer students, Eric Borrego and Rishi Satpathy for their contributions to two-photon microscopy. Aside from making the lab more lively, my undergrads provided valuable input to each project, without their efforts we would not have achieved so much.

I am grateful for Bharath Rajeeva for working with me on fluorescence lifetime imaging for his nanomaterials projects. His conversations about research were always enlightening and amusing. His work in materials science expanded my viewpoint on microscopy. Additional thanks to Dr. Linhan Lin and Mingsong Wang for their work in lifetime imaging of materials.

Thank you to Dr. James Werner and Dr. Doug Shepherd for allowing me to work in their lab during a summer internship at Los Alamos Lab. Their conversations about microscopy and biological research helped to shape my research path and made me a better problem solver. I am hugely grateful to Dr. Chuck DiMarzio and Dr. Andrew Gouldstone for taking time out of their schedule to advise me in undergraduate research; it was through that opportunity that I became interested in biological imaging. Additional thanks to Chuck for mentoring me through the process of graduate applications and opening my world to biomedical optics. I want to thank Dr. Neil Goldstein and Dr. Jason Cline for their excellent mentoring during my two coop experiences at Spectral Sciences Inc., they taught me to be exhaustingly meticulous, and never settle for mediocre work. Thanks to my high school computer science teacher Dan Anderson for introducing me to programming, it has forever changed the way I think.

Finally, I would like to thank my family for their love, and encouragement throughout my life and especially during this study. My Mom and Dad helped shape me into the engineer that I am now, thanks for all the Legos! Thank you Grandma and Grandpa for teaching me to be inquisitive and always ask questions. Thanks to my brother, Alan for his encouraging and humorous conversation. Lastly, thanks to Marcella for always supporting me through both exciting moments and highly frustrating parts of my work. You have always encouraged me to do the best work that I can, and I am endlessly grateful to have you in my life.

Nonlinear Microscopy Methods for Imaging and Particle Tracking in Thick Biological Specimen

Evan Paul Perillo, Ph.D.

The University of Texas at Austin, 2017

Supervisor: Andrew K. Dunn

Co-Supervisor: Hsin-Chih “Tim” Yeh

Optical microscopy techniques such as single-particle tracking and high-resolution (<500 nm) imaging are critical tools for the advancement of biological research. However most high-resolution optical techniques utilize a camera-based or confocal-based detection scheme, which limits the working distance into samples to approximately 10 μm due to light scattering. Nonlinear excitation methods, such as two- and three-photon microscopy, have enabled imaging in thick and scattering samples due to their longer excitation wavelengths and absence of spatial filtering. However, nonlinear excitation is rarely utilized for single-particle tracking as it traditionally offers slightly worse resolution than the aforementioned methods. This dissertation presents the progress made towards adapting nonlinear excitation for high-resolution biological study at scales ranging from single-molecules up to entire tissues. We describe a novel single-particle tracking microscope based upon multiplexed nonlinear illumination, coined TSUNAMI. Single-particle tracking with nanometric resolution using TSUNAMI is demonstrated in live cells and spheroid tumor models to unprecedented depths of 200 μm . Several new long wavelength excitation laser sources are detailed which provide superior image penetration depth compared with traditional sources. Furthermore, we detail a newly discovered form

of nonlinear excitation, based upon a two-color, three-photon absorption process, and discuss potential benefits of this new excitation regime. The systems and methods developed in this work will provide life scientists with a powerful toolset for the future of biological research.

Table of Contents

List of Tables	xiii
List of Figures	xiv
Chapter 1: Introduction	1
1.1 Optical Microscopy.....	1
1.2 Nonlinear Excitation	2
1.3 Two-Photon Instrumentation	3
1.4 Limits to Resolution and Localization.....	5
1.5 Overview of Dissertation Study.....	6
1.6 References.....	8
Chapter 2: Tracking Single-particles Using Nonlinear And Multiplexed Illumination (TSUNAMI).....	10
2.1 Introduction.....	10
2.2 Instrumentation	12
2.2.1 Concept	13
2.2.2 Acquisition Hardware	15
2.2.3 Acquisition Software	17
2.3 Optical Design	19
2.3.1 Beam Multiplexer Design	19
2.3.2 Scanning Optics	20
2.3.3 Collection Optics	22
2.3.4 Filters	23
2.4 Characterization	25
2.4.1 Localization Precision.....	25
2.4.1 Calibration.....	26
2.4.2 Temporal Resolution.....	28
2.4.3 Tracking Depth	30
2.4.4 Localization versus Photon Signal.....	32
2.4.5 Measurement of Lifetime.....	33

2.5 References.....	36
Chapter 3: Tracking Endothelial Growth Factor (EGF) Complexes in Live Cells with TSUNAMI	39
3.1 Introduction.....	39
3.2 EGF Tracking in Live Cells.....	39
3.2.1 Preparation of samples for EGF tracking.....	39
3.2.2 EGF Monolayer Live Cell Trajectories	42
3.3 Deep EGF 3D Tracking in Spheroid Models.....	43
3.3.1 Spheroid formation and initiation protocol for A431 cells	43
3.3.2 Deep EGF 3D Tracking in Spheroid.....	44
3.3.3 Additional Deep EGF Trajectories in Spheroids	46
3.4 EGF Control Experiments.....	48
3.4.1 EGF Induces internalization of EGFR.....	49
3.4.2 Inhibited Spheroid Trajectories.....	50
3.5 Trajectory Data Processing and Visualization.....	51
3.6 Trajectory Segmentation Analysis.....	51
3.7 Discussion.....	56
3.8 References.....	59
Chapter 4: Improvements to TSUNAMI and Dual Particle Tracking	61
4.1 Improved Beam Multiplexer Design	61
4.2 Enhanced Localization with Maximum Likelihood Algorithm.....	63
4.2.1 Axial localization with arithmetic method.....	64
4.2.2 Implementation of MLE	67
4.2.3 Comparison between localization methods	70
4.3 Simultaneous Tracking and Imaging with STED Microscopy	72
4.4 Two-color dual particle tracking microscopy	76
4.4.1 Multiple Particle Localization.....	77
4.4.2 Dual particle tracking of DNA in solution.....	80
4.5 Discussion.....	82
4.6 References.....	83

Chapter 5: Fiber Lasers for Two-photon Microscopy	85
5.1 Introduction.....	85
5.2 Ytterbium Fiber Oscillator.....	87
5.2.1 Instrumentation	87
5.2.2 Characterization	89
5.2.3 Build Protocol	90
5.3 Deep In vivo imaging with Fiberlaser	92
5.3.1 Animal Procedure	92
5.3.2 Chronic preparation	93
5.3.3 Imaging session.....	93
5.3.4 Two-Photon Microscope.....	94
5.3.5 Vasculature Imaging	95
5.4 Discussion	99
5.5 References.....	101
Chapter 6: Two-color two-photon Excitation with a Diamond Raman Laser	104
6.1 Introduction.....	104
6.1.1 Existing Commercial Products	105
6.2 Dual Output Laser System for Two Color Excitation	106
6.3 Ytterbium Fiber Amplifier.....	108
6.3.1 Instrumentation	108
6.3.2 Parabolic Amplifier Design	111
6.3.3 Optical Design	112
6.3.4 Characterization	113
6.4 Diamond Raman Laser	115
6.4.1 Instrumentation	116
6.4.3 Mode Matching Design.....	117
6.4.2 Characterization.....	118
6.5 Two-color Two-photon Excitation Microscopy	120
6.5.1 Dual output laser system.....	120
6.5.2 Two-color excitation efficiencies for common fluorophores ...	123

6.6 Two-color Multiphoton Excitation Imaging	124
6.6.1 Two-color Three-photon Excitartion of Spheroids.....	124
6.6.2 Deep Two-color Multiphoton Imaging in a Living Mouse Brain	127
6.7 Discussion	131
6.8 References.....	133
Chapter 7: Conclusion.....	137
7.1 Summary	137
7.1.1 Single Particle Tracking with Nonlinear Excitation	137
7.1.2 Near-Infrared Lasers for Nonlinear Microscopy	138
7.2 Future Directions	139
7.2.1 Combined Superresolution and 3D Tracking	140
7.2.2 Dual Particle Tracking Microscopy.....	140
7.2.3 Tunable Long Wavelength lasers for Deep Imaging	141
7.3 References.....	141
References.....	143

List of Tables

Table 2.1 Filters used in two-photon microscope	24
Table 3.1 Comparison of tracking errors from different estimation algorithms ..	69
Table 5.1 Summary of select components used in laser build	91
Table 6.1 Summary of select components used in fiber amplifier build	110
Table 6.2 Diamond Laser Optical Components	117

List of Figures

Figure 1.1 Comparison between imaging methods.....	2
Figure 1.2 Two-photon microscopy.....	4
Figure 2.1 Comparison of Microscopy Techniques.....	13
Figure 2.2 3D Tracking Instrumentation.....	14
Figure 2.3 TSUNAMI control schematic.....	16
Figure 2.4 Photograph of TSUNAMI Microscope	19
Figure 2.5 TSUNAMI Scan Lens Design	21
Figure 2.6 Scanning Wavefront Error.....	22
Figure 2.7 Collection Optics Design.....	23
Figure 2.8 Single-particle Localization in TSUNAMI	26
Figure 2.9 Characterization of directed motion and free diffusion.	27
Figure 2.10 50 μ s Time resolution	29
Figure 2.11 TSUNAMI Depth Characterization.....	31
Figure 2.12 Photon-limited localization precision.	33
Figure 2.13 Simultaneous Measurement of Lifetime while Tracking	34
Figure 3.1 Preparation of specimen for EGF Tracking.....	40
Figure 3.2 EGF Tracking in Live Monolayer Cells	42
Figure 3.3 Spheroid Formation Protocol.....	44
Figure 3.4 Deep single particle tracking of EGFR in spheroid model.....	45
Figure 3.5 Additional deep single particle tracking in spheroid model.	47
Figure 3.6 Intra-cellular transport in spheroid model.	48
Figure 3.7 EGF induces internalization of EGFR.....	49
Figure 3.8 Inhibited spheroid trajectory.....	50

Figure 3.9 Procedure for segmentation and classification of trajectories	52
Figure 4.1 Independent Control Beam Multiplexer Schematic	62
Figure 4.2 TSUNAMI Error Profiles	65
Figure 4.3 Axial Error Signal as a Function of XY Position	65
Figure 4.4 Axial Error Profile Inconsistency	66
Figure 4.5 Representative z trajectories and tracking error distribution.....	69
Figure 4.6 Comparison between ESA and MLE Algorithms	71
Figure 4.7 Single Wavelength 2P STED Schematic.....	73
Figure 4.8 2P STED Preliminary Results	74
Figure 4.9 2P STED in a Fixed Cell	75
Figure 4.10 Raw Photon Count Data for Two-color TSUNAMI	77
Figure 4.11 Two-Color Localization	78
Figure 4.12 Co-localization of different separation distance bead pairs.....	79
Figure 4.13 Dual Particle Tracking of DNA Constructs in Free Diffusion	80
Figure 4.14 DNA Distance Fluctuations in Free Diffusion	81
Figure 5.1 Schematic of the mode-locked ytterbium fiber laser.....	88
Figure 5.2 Fiber Oscillator Characterization.....	89
Figure 5.3 Two-Photon Microscope	95
Figure 5.4 Deep <i>in vivo</i> Neuron and Vasculature Stack with Fiber Oscillator....	96
Figure 5.5 Deep <i>in vivo</i> neuron imaging comparison between Ti:S and fiber laser	98
Figure 6.1 Commercial dual output laser systems	106
Figure 6.2 Efficient excitation of far-red fluorophores with fiber-pumped diamond Raman laser.....	107
Figure 6.3 Ytterbium Fiber Amplifier Schematic.....	109
Figure 6.4 Fiber amplifier pump coupling design.....	112

Figure 6.5 Ytterbium fiber amplifier pulse-width.....	114
Figure 6.6 Fiber amplifier beam quality	114
Figure 6.7 Fiber Amplifier Pump Power Dependence and Stability	115
Figure 6.8 Diamond Raman Laser Schematic.....	116
Figure 6.9 Dual Output Laser Characterization	119
Figure 6.10 Diamond Laser Pump Power Dependence and Stability.....	120
Figure 6.11 Two-color Excitation Microscope	121
Figure 6.12 Two-color Excitation Power Ratio	122
Figure 6.13 Two-color excitation of far-red proteins	123
Figure 6.14 Two-color three-photon excitation of spheroids.....	125
Figure 6.15 Excitation dependency of tdKatushka2 and Hoechst 33342.	127
Figure 6.16 Deep <i>in vivo</i> microscopy with two-color excitation.	128
Figure 6.17 Neuron <i>in vivo</i> images with Fiber Amplifier.....	130

Chapter 1: Introduction

1.1 OPTICAL MICROSCOPY

Major advancements in biology are often enabled by improvements with imaging methods. For example, the detailed structure of the ribosome was found through advancements in cryo-EM¹, and the structure of neural axons was uncovered through superresolution optical microscopy². Fluorescence microscopy has been used in biology since the early 1900s. Yet, the basic wide-field microscope design which is still widely used today suffers from diffraction limited resolution, poor acquisition speed, and shallow penetration depth. Advancements in imaging technologies often improve upon these three key metrics, (1) resolution, (2) acquisition speed, and (3) penetration depth. In the past few decades, some novel optical microscopy techniques have emerged that extend the resolution and penetration depth into the sample. Recently emerging techniques such as optical coherence tomography (OCT) have extended our ability to see deep into scattering tissue samples³, while still providing resolution on the order of a few microns. And superresolution microscopy^{4,5}, which has become prominent only in the last decade, has extended the resolution of optical techniques well below the traditional diffraction limit.

One class of optical imaging techniques utilize nonlinear excitation to provide contrast in the sample. The most famous of these forms of nonlinear imaging techniques, known as two-photon excitation, allows for high resolution (~300 nm) optical investigation of tissues and live animals (**Figure 1.1**). Two-photon microscopy can reach depths of up to ~1.0 mm because of its long excitation wavelength and highly confined focus without the need for spatial filtering^{6,7}. Two-photon excitation has been instrumental in the advancement of neuroscience study as it provides resolution almost as good as a confocal microscope, but with a penetration depth of two orders of magnitude greater. The combination of high resolution and penetration depth is necessary to study, the micron

sized structure and functions of the living brain. The focus of this work will be outlining the microscopy and laser advancements that utilize nonlinear excitation to study biological samples with emphasis on tumor imaging for cancer, and deep brain imaging for neuroscience research.

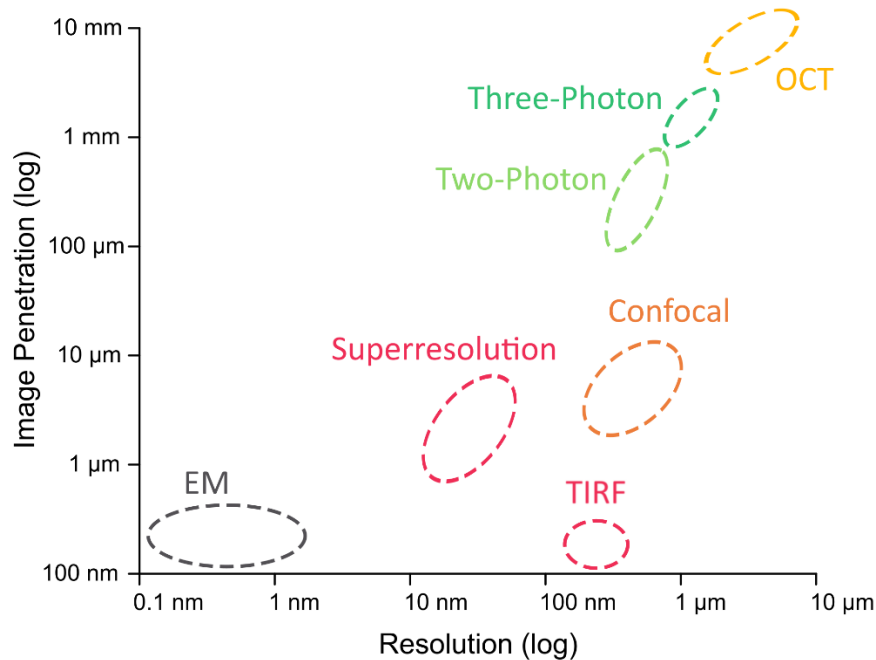


Figure 1.1 | Comparison between imaging methods

Nonlinear excitation techniques such as two- and three-photon microscopy (green circles) occupy an important place in the resolution vs. depth parameter space for high resolution study of living animal tissues. EM: electron microscopy, TIRF: total internal reflection fluorescence, OCT: optical coherence tomography

1.2 NONLINEAR EXCITATION

In traditional wide-field and confocal microscopy the fluorescence excitation is a one-photon absorption process, where the probability of absorption scales linearly with excitation intensity. The practical consequence of this linear relationship is that for imaging of thick samples there is a significant amount of out-of-focus fluorescence light from above and below the focal spot. The out-of-focus excitation in the sample leads to poor quality blurry images. Confocal microscopy mediates this limitation by spatially filtering the

emitted light through a pinhole placed in the conjugate plane of the microscope objective focus. This pinhole has the effect of removing any out-of-plane fluorescence, at the expense of slight loss in signal. Although, the pinhole becomes a limitation in confocal microscopy when imaging through progressively thicker specimen, the collected fluorescence diminishes due to light scattering. Nonlinear excitation microscopies, such as two- and three-photon, avoid this light scattering limitation entirely by using an ultrafast-pulsed laser to excite the sample in a nonlinear excitation process. In the case of two-photon excitation, the sample undergoes two-photon absorption (as opposed to one-photon in confocal) which has an excitation probability scaling with the intensity squared of illumination. This effectively creates a highly confined focus at the sample (approximately $300 \times 300 \times 1000 \text{ nm}^3$) without the need for spatial filtering. The two-photon absorption (2PA) process (**Figure 1.2a**), requires that two-photons from the laser source are in the same femto-liter volume at exactly the same time (<1 femtosecond), this process is highly unlikely to occur in nature. Only through the use of ultrashort pulsed laser with very high peak power (>50 kW) can the two-photon absorption event be made practical. In two-photon absorption, the excitation photons each carry roughly half the energy (twice the wavelength, $\sim 800 \text{ nm}$) as the required bandgap to excite the fluorophore ($\sim 400 \text{ nm}$), the resulting emission process is identical to one-photon fluorescence (**Figure 1.2a**). The effect of confined excitation can be seen in **Figure 1.2b** where linear excitation generates a large cone of light before and after the focus, and the nonlinear (2P) excitation only excites a small focal volume.

1.3 TWO-PHOTON INSTRUMENTATION

The basic instrumentation required for two-photon microscopy is an ultrafast laser, beam scanner, microscope objective, and detector (**Figure 1.2c**). The technique is based on laser scanning microscopy, similar to confocal. In laser scanning microscopy, the image

is built up sequentially in a point-by-point fashion by rapidly moving the beam with an xy scanner (typically galvanometric mirrors) across the sample and measuring the signal on a single pixel detector.

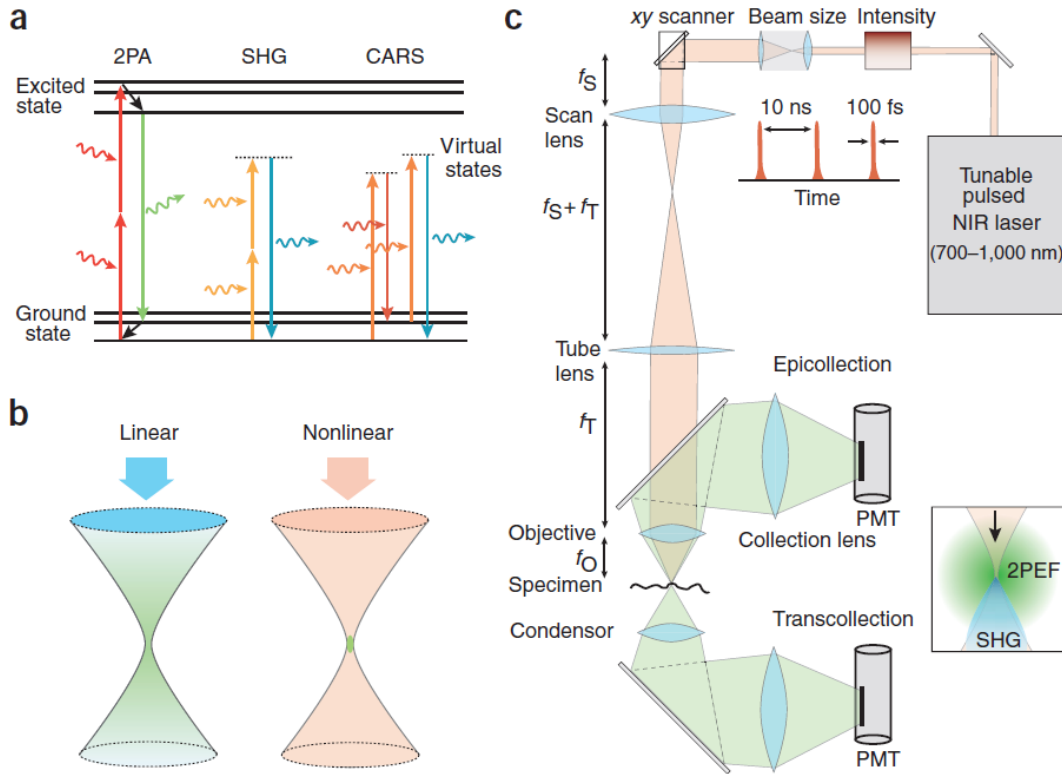


Figure 1.2 | Two-photon microscopy

(a) Jablonski diagram of nonlinear excitation processes (b) Linear vs. nonlinear excitation spatial confinement (c) two-photon microscopy instrumentation.⁸

Photomultiplier tubes (PMT, **Figure 1.2**) are commonly used as detectors because of their large area and high sensitivity to the emitted fluorescence light (400-700 nm). The large area of the PMT facilitates a non-descanned detection scheme, whereby all of the emitted fluorescence light exiting the objective is relayed onto the detector, without passing back through the scanning module and without spatial filtering from a pinhole. This lack of spatial filtering allows efficient collection of fluorescence even if the photons are scattered several times through the sample before exiting the objective.

The most critical piece of instrumentation in nonlinear microscopes is the ultrashort pulsed laser. The most common type of ultrashort pulsed laser for two-photon microscopy is the titanium:sapphire laser which is tunable between 700-1000 nm, typically has a pulse width of 150 fs (10 nm bandwidth), and pulse repetition rate of ~80MHz. These lasers are ubiquitous in biological imaging applications because of their relatively large tuning range, stable operation, and high power output (>2 W). However, Ti:S lasers suffer some drawbacks, primarily with their relatively short wavelengths which lead to loss of signal when imaging deeper than ~600 μm through scattering tissue, such as brain.^{9,10} Laser sources that improve upon this limitation are a primary focus of this work (**Chapters 5 & 6**).

1.4 LIMITS TO RESOLUTION AND LOCALIZATION

The resolution of an optical microscope is limited to diffraction of light and can be defined as,⁸

$$\delta = \frac{1.22 \lambda}{2 NA} \quad (1)$$

Where λ is the wavelength, and NA is the numerical aperture of the objective lens. This fundamental limitation for far-field diffraction of light poses a challenge for any microscopy technique, as the NA of the objective can only be increased so much, and common fluorophores limit the wavelength of light to roughly the visible range (400-700 nm). For a visible confocal microscope with 1.5 NA objective, the resolution can be no better than ~200 nm in the xy direction.

Although diffraction of light limits the ability to resolve two or more emitters in close proximity, the ability to localize a single emitter can still be significantly better than the diffraction limit of light, even with the same illumination sources and optics. Localization refers to the ability to know with statistical certainty where the centroid of an

emitter lies in a sample. Since it is a stochastic process, it relies primarily on how many events (photons) can be collected in a given exposure time. To a lesser extent, it also relies on wavelength and NA of the objective to form the upper bounds for the localization area. The localization precision follows the relationship,

$$\sigma = \frac{s}{\sqrt{N}} \quad (2)$$

Where, s is the PSF extent in square nanometers, and N is the number of photons collected from the single emitter during the exposure period⁴. This stochastic localization process indicates that, for a given PSF size, the localization precision of single emitters only depends on the number of photons collected. A precision of 10 nm is achievable if roughly 1000 photons are collected from the emitter, while up to ~2-3 nm is achievable if 10,000 photons are collected. This process holds true for any localization based technique, including light sheet microscopy¹¹, and multiplexed confocal detection^{12,13}. More generally, with the localization scales as $\sigma \propto N^{-1/2}$, with the geometric term, s , being different for each form of microscopy. In **Chapter 2** I discuss a novel approach to localize emitters to ~30 nm precision using multiplexed nonlinear excitation, and apply the approach to tracking of single particles.

1.5 OVERVIEW OF DISSERTATION STUDY

The goals of this study are to provide detailed advancements in nonlinear microscopy to study thick biological samples. The advancements include, a novel microscope platform for 3D single particle tracking based upon nonlinear excitation, novel long wavelength infrared lasers emitting in the range of 1050-1240 nm for two- and three-

photon excitation, and the discovery of a new nonlinear excitation process (two-color, three-photon excitation).

First, the novel optical microscope design that enables high resolution single particle tracking in thick samples is discussed in **Chapters 2-4**. **Chapter 2** covers the specific instrumentation involved with emphasis on characterization and calibration of the technique. The technique, coined TSUNAMI, works by spatiotemporal multiplexing of excitation light from an ultrafast laser to create 4 spatially confined volumes that can be independently read out. The signal from each of the four excitation volumes can then be used to estimate a particle's position based on a localization approach, and then used to correct the misalignment to keep the excitation centered on the particle. By recording the output from the localization algorithm at each time step it is possible to reconstruct a three-dimensional trajectory of the particle's path through the sample. The detailed characterization in **Chapter 2** contains analysis of the tracking depth limits, localization precision, speed, and ability to record additional information such as fluorescence lifetime. **Chapter 3** covers the current applications using TSUNAMI in live cell particle tracking. Several representative trajectories are discussed, and a trajectory characterization algorithm is outlined. Further improvements to the TSUNAMI technique are mentioned in **Chapter 4** with an emphasis on the flexibility of TSUNAMI for a wide variety of application areas. Specifically, combination with super-resolution microscopy and dual particle tracking are discussed in **Chapter 4**. The homebuilt lasers for nonlinear excitation are covered in **Chapters 5 & 6**. A homebuilt ytterbium fiber oscillator is detailed in **Chapter 5**, which covers the thorough details of the design, characterization, and application to deep *in vivo* microscopy. The focus of the ytterbium fiber laser work is to provide the biological community with a homebuilt laser solution offering longer wavelength excitation compared to Ti:S lasers, at a fraction of the price (~\$13,000 for all

components). The longer wavelength excitation of the ytterbium laser (1060 nm vs. 800 nm) allows for deeper imaging than what is achievable with Ti:S lasers. Imaging neurons in a live mouse to a depth of 900 μm is demonstrated. In **Chapter 6** a homebuilt dual output laser source is discussed. The dual output source consists of a ytterbium fiber amplifier (1055 nm) and a diamond Raman laser (1240 nm), both lasers in combination are used to create a relatively less common form of nonlinear excitation known as two-color two-photon excitation. In two-color excitation, a photon from each laser is absorbed simultaneously in a similar way to one-color two-photon absorption, the sum of their energies allow excitation of a bandgap not achievable with either laser alone. The effective wavelength of two-color excitation is 1140 nm for the novel dual output laser system. I further discuss a newly discovered nonlinear excitation process known as two-color three-photon excitation. Potential benefits and applications of two-color three-photon are described in **Chapter 6**.

This work details several key advancements to nonlinear microscopy techniques, with a heavy emphasis towards direct biological applications. The systems and methods described herein are intended to add to the ever evolving toolset of optical microscopy techniques to study biology and neuroscience. Following the breakthrough advancements in super-resolution microscopy of the past decade, the next step will be to move towards imaging thicker samples ($>100 \mu\text{m}$) with better than diffraction limited resolution ($<200 \text{ nm}$), at time scales relevant to biology (1 ms – 1 s).

1.6 REFERENCES

1. Khatter, H., Myasnikov, A. G., Natchiar, S. K. & Klaholz, B. P. Structure of the human 80S ribosome. *Nature* (2015). doi:10.1038/nature14427
2. Xu, K., Zhong, G. & Zhuang, X. Actin, Spectrin, and Associated Proteins Form a Periodic Cytoskeletal Structure in Axons. *Science* (80-.). 452–457 (2013).
3. Fujimoto, J. G., Pitris, C., Boppart, S. A. & Brezinski, M. E. Optical Coherence

Tomography : An Emerging Technology for Biomedical Imaging and Optical Biopsy 1. *Neoplasia* **2**, 9–25 (2000).

4. Rust, M. J., Bates, M. & Zhuang, X. imaging by stochastic optical reconstruction microscopy (STORM). **3**, 793–795 (2006).
5. Betzig, E. *et al.* Imaging Intracellular Fluorescent Proteins at Nanometer Resolution. *Science (80-.)*. **x**, 1642–1646 (2006).
6. Denk, W., Strickler, J. H. & Webb, W. W. Two-photon laser scanning fluorescence microscopy. *Science* **248**, 73–76 (1990).
7. Zipfel, W. R., Williams, R. M. & Webb, W. W. Nonlinear magic: multiphoton microscopy in the biosciences. *Nat. Biotechnol.* **21**, 1369–77 (2003).
8. Helmchen, F. & Denk, W. Deep tissue two-photon microscopy. *Nat. Methods* **2**, 932–40 (2005).
9. Oheim, M., Beaurepaire, E., Chaigneau, E., Mertz, J. & Charpak, S. Two-photon microscopy in brain tissue: parameters influencing the imaging depth. *J. Neurosci. Methods* **111**, 29–37 (2001).
10. Theer, P., Hasan, M. T. & Denk, W. Two-photon imaging to a depth of 1000 microm in living brains by use of a Ti:Al₂O₃ regenerative amplifier. *Opt. Lett.* **28**, 1022–1024 (2003).
11. Chen, B.-C. *et al.* Lattice light-sheet microscopy: Imaging molecules to embryos at high spatiotemporal resolution. *Science (80-.)*. **346**, 1257998–1257998 (2014).
12. Sahl, S. J., Leutenegger, M., Hilbert, M., Hell, S. W. & Eggeling, C. Fast molecular tracking maps nanoscale dynamics of plasma membrane lipids. *Proc. Natl. Acad. Sci.* **107**, 6829–6834 (2010).
13. Wells, N. P. *et al.* Time-resolved three-dimensional molecular tracking in live cells. *Nano Lett.* **10**, 4732–7 (2010).

Chapter 2: Tracking Single-particles Using Nonlinear And Multiplexed Illumination (TSUNAMI)¹

2.1 INTRODUCTION

Nonlinear microscopy methods such as two-photon microscopy are routinely utilized for thick samples to overcome the limitation with scattered light in spatial filtering techniques such a confocal. However, two-photon excitation is not often used for single particle applications, as it requires complex instrumentation, and orders of magnitude higher excitation power. Although, to study single particle dynamics in thick tissues (beyond $\sim 20 \mu\text{m}$) two-photon excitation must be used. Here we describe a novel two-photon base single-particle tracking microscope for imaging within thick specimen.

Single-particle tracking (SPT) has enabled the direct observation of dynamic behaviors of particles (here a particle can be a single biomolecule, a molecular complex, a vesicle, a lipid granule, or a viral capsid) inside complex biological systems,¹⁻⁴ with particle localization precision better than the diffraction limit of light.^{5,6} Through trajectory analysis SPT has provided insight into motor protein kinetics,^{7,8} cellular membrane dynamics,⁹⁻¹¹ mRNA transport^{12,13} and virus internalization processes.^{14,15} As the basis of passive microrheology, SPT has also shed light on the local environments of tracked particles through the observation of changes in particles' random movements.^{16,17}

Whereas SPT is becoming a powerful research tool, all current techniques suffer from one or more of the following problems: shallow penetration depth (arising from the use of one-photon excitation¹⁸⁻²⁰), limited z-tracking range (e.g. TIRF microscopy), poor

¹ Portions of this chapter were adapted from: E.P. Perillo, Y.-L. Liu, K. Huynh, C. Liu, C.-K. Chou, M.-C. Hung, H.-C. Yeh, A. K. Dunn, "Deep and high-resolution 3D Tracking of Single Particles Using Nonlinear And Multiplexed Illumination," *Nature Communications*, 6, 7874 (2015). E.P.P., H.-C.Y. and A.K.D. conceived the project; E.P.P. designed and built the microscope, and developed control software. E.P.P. and Y.-L.L. performed the experiments and analysed the results. E.P.P., H.-C.Y. and A.K.D. wrote the manuscript.

temporal resolution (e.g. frame-by-frame analysis in camera-based methods^{21,22}), and low information content (e.g. no information on the fluorescence lifetime²³). As two-photon (2P) microscopy has become a standard method for deep tissue imaging,²⁴ a few reports demonstrated 3D tracking based on two-photon excitation. One of the earliest demonstrations of 2P tracking used an orbital scanning motion of the focused laser beam to track particles using a single detector,^{5,25,26} but was limited to a temporal resolution of 20~32 ms due to mechanical scanning and signal demodulation. More recently, 3D tracking of gold nanorods with 2P excitation was demonstrated by exciting multiple foci and detecting fluorescence with an EMCCD,²² but the 3D temporal resolution was limited to ~0.5 s. Moreover, the use of a camera in multifocal 2P laser scanning microscopy (2P-LSM) limits the working depth of SPT in scattering samples.²⁷ Although SPT with superior temporal resolution (bounded mainly by the emission rate of the fluorescent label) and simultaneous fluorescence lifetime measurements have been achieved using confocal setups with 3-5 single-element/photon-counting detectors (PMTs or APDs) for spatial filtering,¹⁸⁻²⁰ these methods not only have limited working depth (not using 2P excitation for tracking) but also suffer from loss of signals due to the non-overlapping excitation and collection efficiency peaks in spatial filtering.²⁸ Other confocal based microscopes have been developed using only 2 detectors which are capable of simultaneous spectroscopy measurements,²⁹ however they still suffer from poor penetration depths in scattering samples such as tissues and multi-cellular structures, as well as low collection efficiency. Currently there is no single solution to all of the above issues.

To address this challenge, we have developed a 2P-3D-SPT method capable of tracking particles at depths up to 200 μm in scattering samples with 22/90 [xy/z] nm spatial localization precision and 1 ms response time. With bright fluorophores we can achieve a

temporal resolution down to 50 μ s. At shallow depths the localization precision can be as good as 35 nm in all three dimensions. The approach is based on passive pulse splitters used for nonlinear microscopy³⁰ to achieve spatiotemporally multiplexed 2P excitation and temporally demultiplexed detection³¹ to discern the 3D position of the particle. The z-tracking range is up to ± 50 μ m (limited by the objective z-piezo stage) and the method enables simultaneous fluorescence lifetime measurements on the tracked particles. Like some more recent techniques, this tracking method allows coupling trajectory data with traditional imaging to discern the local environment.^{18,32} However, a major advantage of this method over confocal approaches is that it requires only one detector for SPT and is compatible with multi-color two-photon microscopy. We describe our approach and demonstrate its capabilities by tracking single fluorescent beads in aqueous solutions that include scattering, as well as tracking prescribed motions in these controlled environments. We then demonstrate tracking of EGFR (epidermal growth factor receptor) complexes tagged with fluorescent beads in tumor spheroids, demonstrating deep 3D SPT in multicellular models. We have coined this technique **TSUNAMI** (Tracking Single-particles Using Nonlinear And Multiplexed Illumination).

2.2 INSTRUMENTATION

Tracking Single-particles Using Nonlinear And Multiplexed Illumination (TSUNAMI) is a novel microscopy technique developed to address the specific limitation with penetration depth present in all other single particle localization/tracking methods (**Figure 2.1**). We have shown that TSUNAMI is capable of tracking particles 20x deeper (up to 200 μ m) than confocal and image based particle tracking microscopes through the use of two photon excitation and non-descanned detection. The following subsections will detail the conceptual operation of TSUNAMI, detailed hardware design, and an overview of the software.

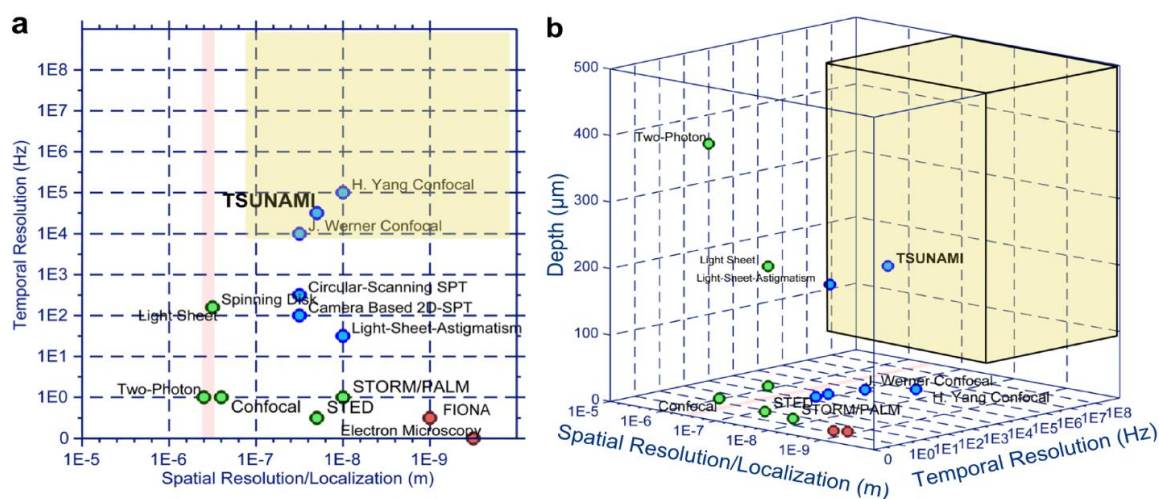


Figure 2.1 | Comparison of Microscopy Techniques

(a) 2D plot spatial vs. temporal resolution (b) 3D plot including depth. TSUNAMI is the only technique that performs well in all three metrics.

2.2.1 Concept

In the spatiotemporal multiplexed scheme, laser pulses emitted with a 13 ns period from a Ti:sapphire oscillator are separated into four beams, which are delayed by 3.3 ns each and focused through a high-N.A. objective at slightly offset xyz positions. The four resulting 2P-excitation volumes are arranged into a barely overlapped, tetrahedral geometry (**Figure 2.2c**), to generate selective excitation equivalent to the spatial filtering condition in the previous four-detector confocal tracking setup,¹⁹ with each 2P-excitation volume receiving laser pulses at a different time delay. For a fluorescent particle residing somewhere inside the excitation tetrahedron, its 2P emission is collected by a

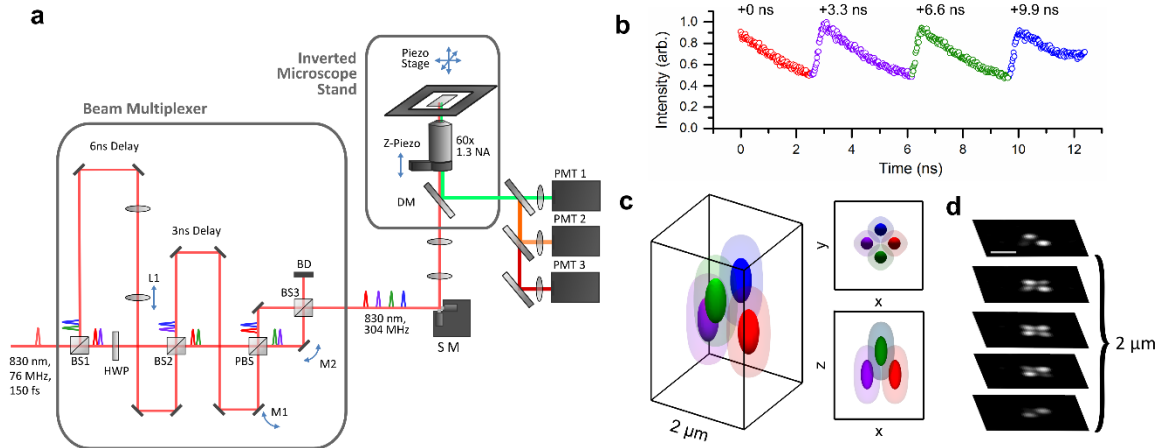


Figure 2.2 | 3D Tracking Instrumentation.

a. Schematic of the two-photon 3D tracking microscope. Spatiotemporal multiplexing is enabled through an optical system which utilizes 2 beam-splitters (BS1 and BS2) to generate 4 beams which can be quasi-independently controlled via mirrors (M1 and M2). Physical delay lines provide temporal separation. In this case, 6.6 ns (2 meters) and 3.3 ns (1 meter) path length delay lines create 4 beams with a period of 3.3 ns corresponding to an even division of the fundamental 13 ns period generated by the laser source (Mira 900, Coherent). Tracking actuation is performed using scanning mirrors (SM) and an objective focusing stage (Z-Piezo). **b.** Photon counting histogram of a particle centered in the middle of the four-excitation focus demonstrating temporal offsets and power balance between the independent excitation beams. **c.** An idealized image space projection of the tetrahedral PSF. **d.** Experimental laser scanning image of a single $\varnothing 100$ nm fluorescent bead with simultaneous 4 beam excitation. Scale bar is $1 \mu\text{m}$. HWP is half-wave plate, PBS is polarizing beamsplitter, DM is dichroic mirror, and BD is beam dump.

photomultiplier tube (PMT1 in **Figure 2.2a**). Through time-correlated-single-photon counting (TCSPC) detection, each detected photon is assigned to a specific time gate (G_1 - G_4 , here assuming the decay time is ~ 4 ns or less, **Figure 2.3**) in the fluorescence decay histogram (**Figure 2.2b**), and therefore attributed to an individual excitation volume. For a particle sitting at the center of the tetrahedron, the resulting photon counts are approximately equal in all four time gates. An offset of the particle from the tetrahedron center can be estimated from the normalized photon count differences in the four time gates (i.e. error signals E_x , E_y and E_z). Once the particle position offset is determined, a closed

feedback loop then steers galvanometer mirrors and the objective z-piezo stage to lock the tracking beams on the particle. A particle's 3D trajectory is therefore determined directly from the controller output sent to the galvanometer and piezo actuators.

Spatiotemporal multiplexing has previously been explored for diffusion measurements³³ and tracking,³⁴ but these methods rely on a picosecond pulsed laser for one photon excitation and therefore are not suitable for use in multicellular models or tissues. Furthermore, only one photomultiplier tube (PMT1 in **Figure 2.2**) is needed for SPT in our method, whereas 3~5 detectors are needed in confocal tracking setups¹⁸⁻²⁰. In addition, the fluorescence lifetime of the tracked particle can be determined from the time-resolved photon data so long as the emitter lifetime is shorter than each time gate (<3.3 ns).²⁶ As the laser beam is steered by active feedback to lock on the tracked particle, a large tracking range is achieved ($\pm 50 \mu\text{m}$ in z direction and $\pm 100 \mu\text{m}$ in xy) with minimal perturbation to the samples (whereas some confocal setups require the sample to be moved in order for SPT^{18,19}).

2.2.2 Acquisition Hardware

The spatiotemporal beam multiplexer (**Figure 2.2**) is created entirely from passive optics comprised of beam splitters, mirrors, and waveplates. A single pulse train from a modelocked Ti:Al₂O₃ laser (Mira 900, Coherent) tuned to 835 nm is used as the primary beam which then gets multiplexed into four beams offset in time and space. For temporal offsets, it was determined that to equally space four beams with an original 76 MHz repetition rate the delay time must be 3.3 ns which corresponds to approximately 1 m physical path length. For spatial offsets each beam is first co-aligned onto the primary optical axis. Adjusters which control x and y offsets are moved until a lateral spacing of approximately 500 nm is achieved in the image plane. Alignment repeatability is verified

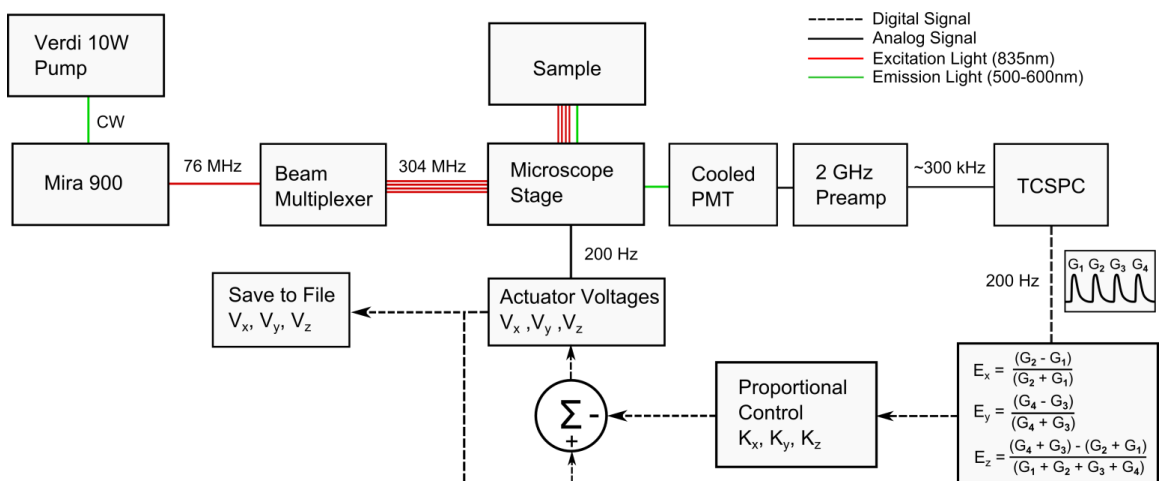


Figure 2.3 | TSUNAMI control schematic.

by projecting fiduciary marks onto the LSM image during alignment such that each beam's center is aligned to the same point in space to sub-100 nm repeatability. Axial spacing is controlled using a telescope assembly placed in the optical path of one beam pair to adjust their collimation. The alignment of axial spacing is verified using molecular detection function 3D scans until a spacing of 1 μm is achieved. Following the optical multiplexer the beams pass through a galvo scanning system (6125H, Cambridge Technology), before being focused through a 60x 1.3 NA silicone oil objective (UPLSAPO60X, Olympus).

Demultiplexing of fluorescence emission is done by time resolving the excitation contributions of each of the four multiplexed beams with fast photon counting electronics. The fluorescence signal detected is an interwoven stream of photons excited by all four excitation beams. That signal can be time gated with 3.3 ns increments to effectively isolate the signal contributions from each beam and consequently isolate the signal contribution in space as well. Emission demultiplexing is done electronically via time-correlated-single-photon counting (TCSPC) analysis (**Figure 2.3**). Fluorescence signals are detected by a cooled GaAsP photomultiplier tube with 5 mm square active area (H7422PA-40,

Hamamatsu) in non-descanned configuration. The current output from the PMT is amplified through a 2 GHz cutoff bandwidth preamplifier (HFAC-26, Becker and Hickl GmbH) and sent into a photon counting board (SPC-150, Becker and Hickl GmbH) to be counted and correlated to the 76 MHz reference clock of the laser oscillator. Given the electronics setup our fundamental timing resolution is on the order of the instrument response frequency which was measured to be 230 ps FWHM (**Figure 2.3**).

Every 1-5 ms a photon histogram is polled from the TSCPC module and processed in the software loop run entirely in LabVIEW (National Instruments). The tracking algorithm employs the simplest type of controller, a proportional control to convert the error signals to new stage positions. New voltages are sent out through a DAQ (PCIe-6353, National Instruments) to their respective actuators, scan mirrors for X and Y, piezo objective stage for Z.

Due to the time critical nature of this measurement technique it is imperative that the control loop operates at the desired frequency, typically 5 ms. To achieve this deterministic requirement in windows operating system the LabVIEW control loop was driven by an external hardware timed clock (counter from PCIe-6353 board) using this method deterministic loops can be achieved with rates up to 2 kHz without missing a hardware clock tick. For a typical 8 minute trajectory there are no missed loops out of 96,000 requested with a 5 ms (200 Hz) control loop period.

2.2.3 Acquisition Software

The tracking acquisition control loop is run entirely in LabVIEW (National Instruments) on the Windows 7 operating system. Time resolved signals from the TCSPC board can be read into LabVIEW by two methods, (1) histogram mode and (2) FIFO (time-tag) mode. In histogram mode the TCSPC board performs on board histogramming of the photons detected during a single control loop period (5 ms) and sends the data to LabVIEW

for processing into new control signals (**Figure 2.3**). In FIFO mode each photon event is recorded by the board and processed on the fly in the LabVIEW control loop. For a loop rate of 5 ms and typical particle count rate of 500 kHz this requires time binning 2,500 photons which are represented with 12-bit precision. This task is easily achievable with current computing hardware. The data on each photon event can be recorded for post processing and re-binning to achieve timing resolutions down to 50 μ s with sufficiently bright particles. Deterministic timing for the LabVIEW control loop is achieved by forcing the program to run on a hardware timed clock from a PCI based data acquisition board (PCIe-6353, National Instruments). Using this hardware timed loop method periods down to 1 ms can be requested with no missed cycles for up to 60 seconds. At 5 ms the timed loop can run indefinitely with no missed cycles up to 20 minutes.

Control signals are generated by taking the ratio of the summed photon counts in each of the 4 times gates. Following the below formulas,

$$E_x = \frac{G_2 - G_1}{G_2 + G_1} \quad (1)$$

$$E_y = \frac{G_4 - G_3}{G_4 + G_3} \quad (2)$$

$$E_z = \frac{(G_4 + G_3) - (G_2 + G_1)}{(G_1 + G_2 + G_3 + G_4)} \quad (3)$$

Where G_1 , G_2 , G_3 , and G_4 are the total photon counts in each time gate. Error signals E_x , E_y , and E_z are modified by a proportional controller before being sent out by the PCIe-6353 board as analog signals to their respective actuators (galvos for x and y, and objective piezo stage (P-726 PIFOC, PI) for z).

2.3 OPTICAL DESIGN

2.3.1 Beam Multiplexer Design

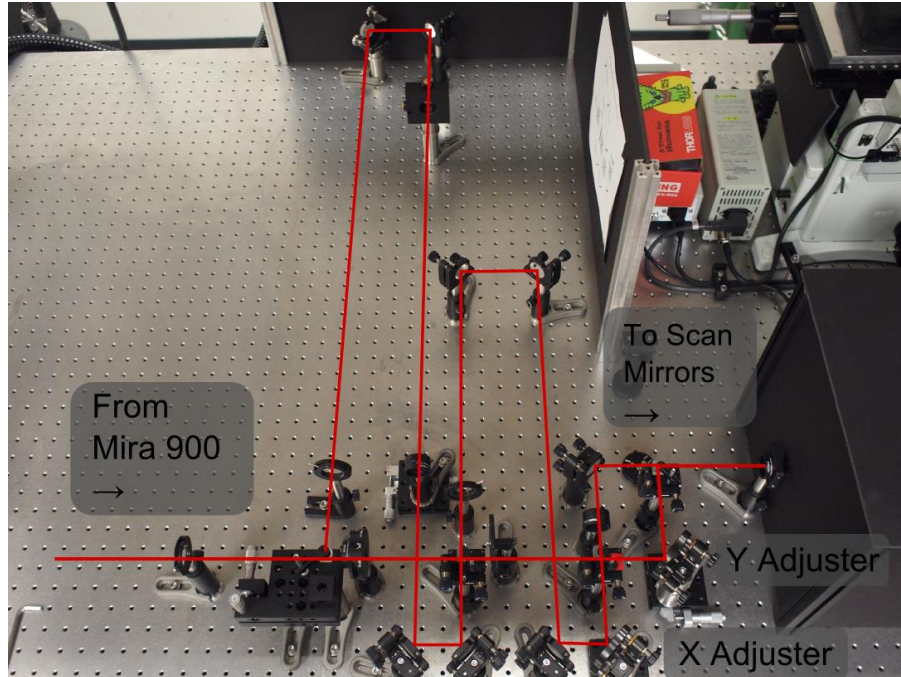


Figure 2.4 | Photograph of TSUNAMI Microscope

A photograph of the beam multiplexer optical system (**Figure 2.4**). A 76 MHz pulse train from a mode-locked Ti:Al₂O₃ (Mira 900, Coherent) is split into 4 beams and recombined onto a single optical axis. Beam spacing is tuned by mirrors marked as x and y adjusters. The design is such that the offset adjustments are made as close as possible to the scanning mirror module to reduce lateral offsets in the beams at the microscope back aperture. Although the angular deviation between beams is small (100-200 arcsec) over a great distance the offsets lead to significant power imbalance from aperture clipping. Another design consideration was to minimize beam divergence over such large delay distances (up to 3 m for the fourth excitation beam). Divergence was mitigated by way of a 4× beam expansion using a telescope assembly prior to entering the beam multiplexer

system. The beam diameter was expanded from 2 mm to 8 mm to reduce divergence proportionally. Following the multiplexer the beams are reduced back to 2 mm width with a telescope and relayed through a galvo scanning mirror system (6125H, Cambridge Technology). The relay design is such that the aperture of the beam multiplexer is imaged onto the galvo scan mirrors while the image formed by the galvo scan mirrors is relayed onto the back aperture of the microscope objective. If this condition is satisfied there will be minimal lateral shift on back aperture from both the image of the galvo scan and the image of the multiplexer.

2.3.2 Scanning Optics

The scanning optics in TSUNAMI follow the design of a traditional two-photon microscope³⁵. The primary considerations being minimal wavefront distortion over the desired field of view. In this case the field of view required is on the order of 100-200 μm at maximum to image the surrounding environment of cell clusters or tissue models. The field of view of the scanning optics also sets the maximum lateral tracking distance when using the microscope in TSUNAMI mode. To design the optimal scan lens system, a Zemax model was created, and an optimization was performed to minimize wavefront error at the extreme scan angles of $\pm 2^\circ$ in both x and y axes. Stock components were selected to reduce cost and because the design criteria was easily achievable.

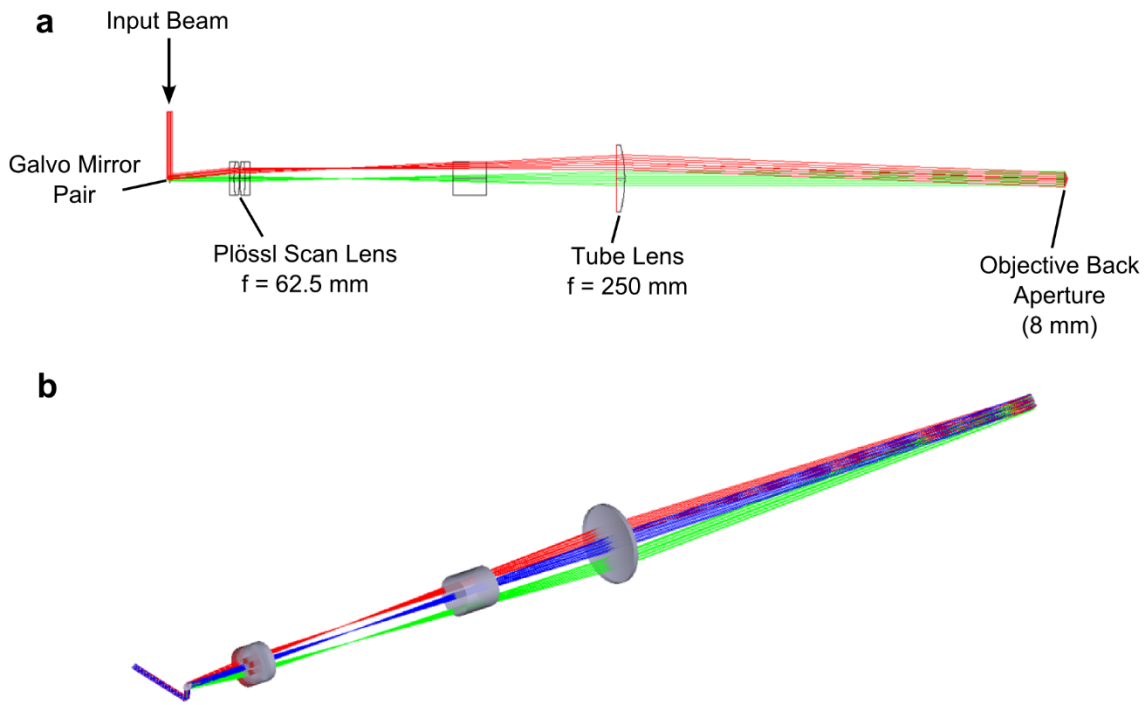


Figure 2.5 | TSUNAMI Scan Lens Design

(a) 2D plan view (b) 3D solid model. The scanning optics design allows for a $200\mu\text{m}$ field of view with minimal wavefront distortion and chromatic aberration.

The scanning optics consist of a galvo mirror pair (6125H, Cambridge Technology), with mirror separation of 10 mm, and mirror size to accommodate up to 3mm beam diameter. Following the galvo mirrors are a Plössl type scan lens pair (effective focal length = 62.5 mm) and a singlet tube lens (focal length = 250 mm). The total magnification is 4 times to create a final beam diameter of 8 mm with an input diameter of 2 mm (**Figure 2.5**).

The relatively long tube lens focal length was selected to minimize wavefront distortion when scanning and when aligning the beam multiplexer. The overall wavefront

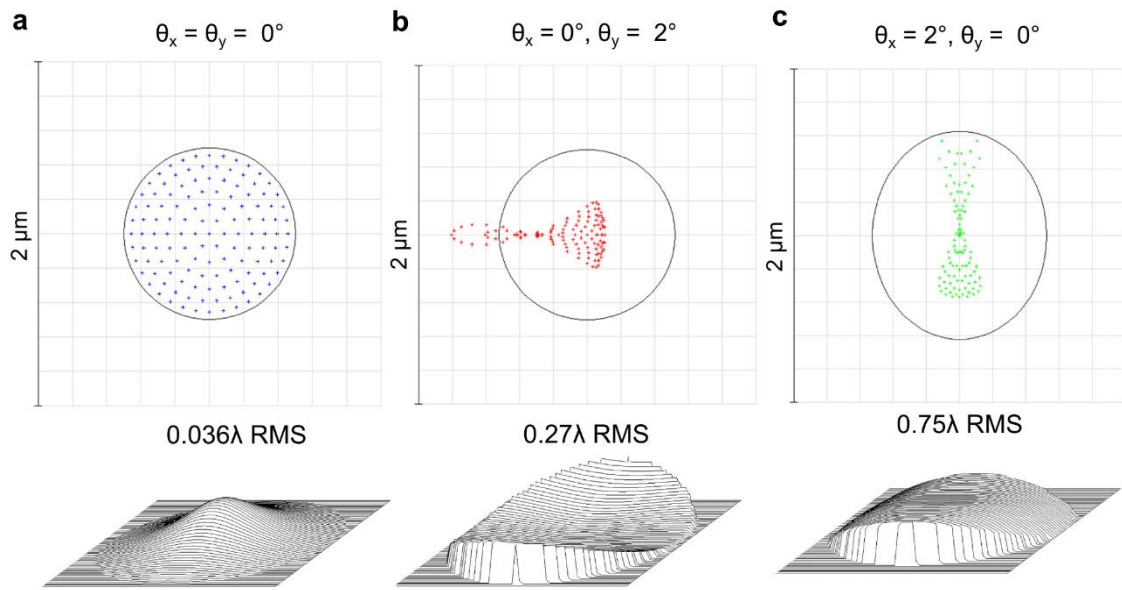


Figure 2.6 | Scanning Wavefront Error

(a) $[0^\circ, 0^\circ]$ (b) $[0^\circ, 2^\circ]$ (c) $[2^\circ, 0^\circ]$. The wavefront error is negligible in the center field of view, and moderate with very large field of view (200 μm).

distortion for the central field $[0^\circ, 0^\circ]$, is 0.036λ , which has a negligible impact on the point spread function (**Figure 2.6**). However, for the extreme angles, $\pm 2^\circ$, the wavefront error was found to be 0.27λ and 0.75λ in x and y, respectively. The wavefront error yields a distorted PSF that can moderately affect image quality and tracking performance (0.25λ is equivalent to the distortion introduced from a stock optical grade mirror). A 2° angle corresponds to a total field of view of 200 μm , which is significantly larger than the FOV used even for tracking in tissue models ($\sim 30 \mu\text{m}$).

2.3.3 Collection Optics

The collection optics were designed to efficiently collect light over the entire field of view of the scanning optics. The 5 mm active area of the H7422PA-40 detector is large enough that it allows for some loose design considerations. However, one major obstacle was the large distance between the detector and objective back aperture (300 mm) due to the inverted microscope design. Collection efficiency is directly proportional to the squared

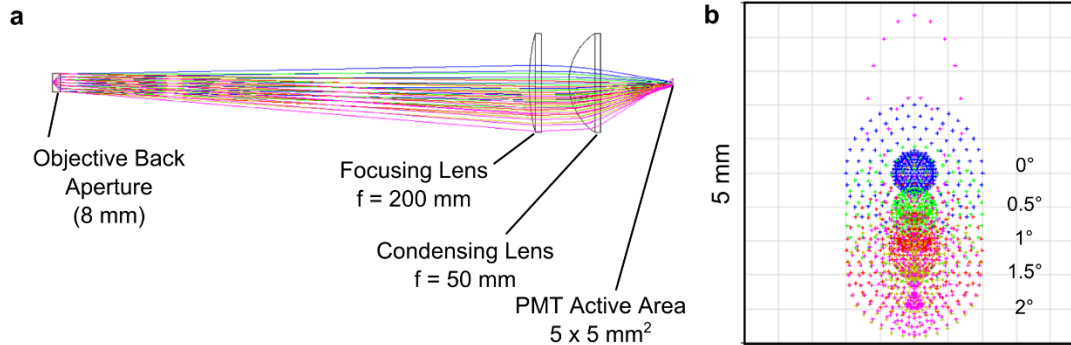


Figure 2.7 | Collection Optics Design

(a) 2D Raytrace (b) Fullfield spot diagram. All of the light can be efficiently collected onto the detector across a 200 μm cubic volume in the sample.

distance from the source aperture, so the large distance created a challenge to efficiently collect the light emitting from all angles of the field of view. Using a two lens pair, to collimate and subsequently condense the light onto the PMT active area allowed for full collection of the rays on to the detector for light emitted from the image plane (**Figure 2.7**). However, light that is heavily scattered, as from thick biological specimen, is not able to be fully collected onto the back aperture, leading to loss of efficiency and low signal-to-noise ration when imaging very deep ($>200 \mu\text{m}$). From empirical evidence, this system is only capable of imaging common brightness dyes approximately 200 μm deep in living mouse brain tissue. The only way to improve collection efficiency when imaging deep would be to use a different microscope body that allowed for closer placement of the detectors to the objective back aperture³⁶.

2.3.4 Filters

The TSUNAMI microscope has several filter options depending on the fluorophore used. There are two filter sets, one for excitation, and one for emission. The excitation filter set is usable over the range of 750-900 nm, and consists of a 715 nm longpass filter, 700 nm shortpass dichroic, and 720 nm shotpass filter. The 715 longpass filter removes residual

visible light in the laser path before entering the dichroic filter cube. This filter is especially critical in situations where the excitation light is shot <800 nm, and the emission signal is long >650 nm. The 720 nm shortpass is placed on the emission side after the dichroic to filter out any scattered laser light before entering the detector module.

Filter	Usage	Manufacturer	Part Number
715 LP	Block leaked visible light from laser	Semrock	FF01-715/LP-25
700 SP Dichroic	Excitation Dichroic	Semrock	FF700-SDi01-25x36
720 SP	Laser Blocking	Semrock	FF01-720/SP-25
550 LP Dichroic	Emission Splitter	Semrock	FF552-Di02-25x36
640 LP Dichroic	Emission Splitter	Semrock	FF640-FDi01-25x36
457/50 BP	DAPI, Hoechst 33342	Semrock	FF01-457/50-25
525/40 BP	Yellow-green FluoSpheres, YFP	Semrock	FF02-525/40-25
593/46 BP	Red FluoSpheres	Semrock	FF01-593/46-25
605/64 BP	mCherry, Texas Red	Semrock	FF01-605/64-25
641/75 BP	tdKatushka2	Semrock	FF02-641/75-25
675/67 BP	Dark Red FluoSpheres	Semrock	FF02-675/67-25
700/75 BP	CellMask™ Deep Red	Chroma	ET700/75m

Table 2.1 | Filters used in two-photon microscope

LP is longpass, SP is shortpass, BP is bandpass.

The emission filters consist of dichroic splitters, and bandpass filters. Since all detectors share the same optical path after the excitation cube, they all share the same

laser clean up filter and there is no need for secondary laser blocking filters. There are three detectors in the TSUNAMI microscope, that cover three primary visible regions (blue/green, 400-550 nm), (yellow/orange, 550-640 nm), and (red/NIR, 640-720 nm). Bandpass filters are selected for each PMT depending on the fluorophores used in the experiment (**Table 2.1**).

2.4 CHARACTERIZATION

2.4.1 Localization Precision

To calibrate our 3D localization technique $\varnothing 100$ nm fluorescent beads were immobilized in an agarose gel and imaged ~ 20 μm past the coverslip. 3D images were taken in 3 by 3 by 5 μm^3 stacks. At each voxel of the stack a photon counting histogram was recorded using 5 ms integration time. The raw waveform was and processed to yield error values along all three dimensions. The composite image of all 4 beams at the mean z focus. Blue lines denote the center x and y axes (**Figure 2.8a**). The X error map which is a calculation of x error weight E_x at every pixel in the image (**Figure 2.8b**). Y error map which is a calculation of the y error weight, E_y , at every pixel in the image (**Figure 2.8c**). A line profile through the x error map at the location drawn in Figure 2.8b. Precision target tracking is feasible over a 500 nm range (**Figure 2.8d**). Normalized error line profile through y error map Figure 2.8c showing near exact positional dependence on error as the x profile, as expected (**Figure 2.8e**). Normalized error through all images in the stack located at the mean intensity position denoted by the intersection of the blue lines in Figure 2.8a. To smooth the curve the error value was calculated with 2 adjacent pixels in each image, the slope remains the same. Scale bar is 1 μm (**Figure 2.8f**).

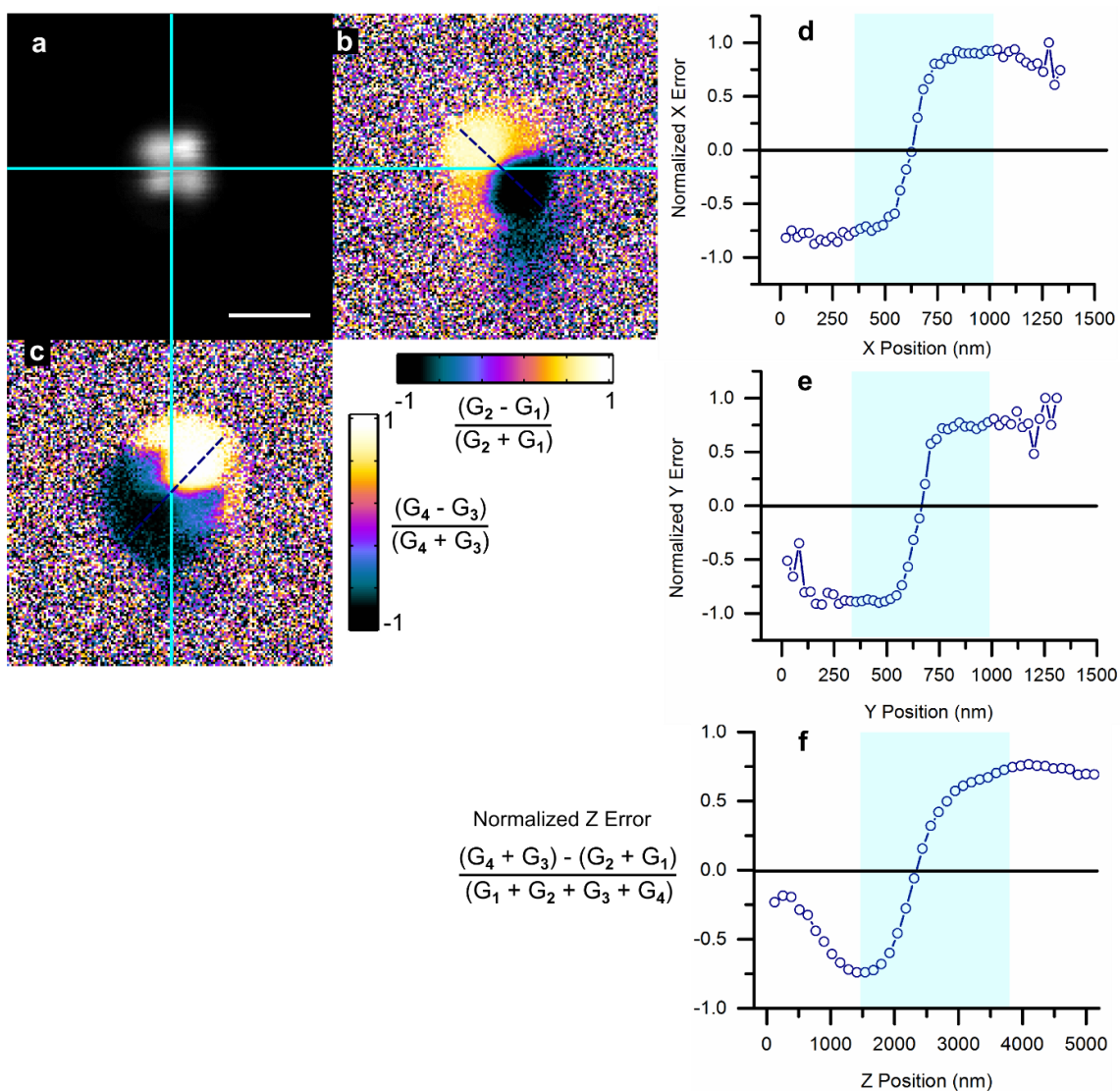


Figure 2.8 | Single-particle Localization in TSUNAMI

(a) Experimental image of single fluorescent bead (b) x error map (c) y error map (d) x error signal (e) y error signal (f) z error signal

2.4.1 Calibration

To validate our TSUNAMI microscope, we first tracked fluorescent beads ($\varnothing 100$ nm, decay time ~ 4.5 ns) in aqueous solution (**Figure 2.9c**) and in 9% gelatin gel with 1% intralipid (a highly scattering tissue mimicking environment). By following the artificial

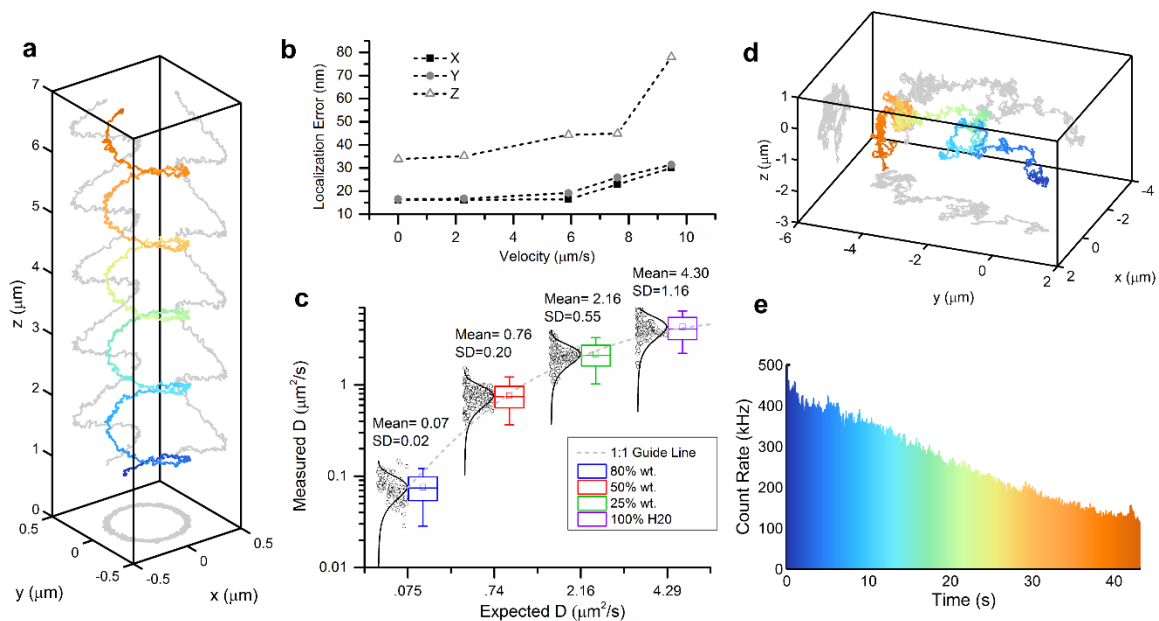


Figure 2.9 | Characterization of directed motion and free diffusion.

(a) Example helical trajectory of a $\varnothing 100$ nm fluorescent bead moved through a known path using an independent 3D piezo stage (P-733K130, PI). The path duration was 7 seconds with an average velocity of $2.1 \mu\text{m s}^{-1}$. The tracking system reproduced the true trajectory accurately with 16.5 nm uncertainty in x and y and 33.3 nm in z. Rainbow coloration corresponds to time with blue representing the beginning of the trajectory. (b) Several helical trajectories were performed with varying mean velocities. The particle localization uncertainty increases with increasing velocities up to $10 \mu\text{m s}^{-1}$, where the particle speed is too fast for the controller to target lock. (c) Box plot with histograms of measured versus theoretical diffusion coefficients for 80% wt. glycerol, 50% wt. glycerol, 20% wt. glycerol, and 100% water, respectively. The measured central tendency of the diffusion coefficients were found to agree with the Stokes-Einstein equation for wide range of values ($0.07 - 4.3 \mu\text{m}^2 \text{s}^{-1}$). The agreement with theory can be seen by how closely the data follow the 1:1 guide line (plotted on semilog scale) (d) An example trajectory of a $\varnothing 100$ nm fluorescence bead in an 80% wt. glycerol solution, free diffusion was observed over 43 seconds. (e) Particle photon count rate versus time, a monotonically decreasing count rate indicates that a single bead, or aggregate, is stably locked in the field of view for the entire duration of the trajectory with no other particles entering or leaving the field of view.

prescribed motions in these controlled environments,^{5,37} we successfully characterized the localization precision, tracking speed limits, temporal resolution, and tracking depth of our system.

From optical modeling, the optimal lateral and vertical separation distances between the two-photon excitation volumes were estimated to be 500 nm and 1,000 nm, respectively.²⁸ The alignment of the four excitation beams was verified by volumetric scanning of a fixed fluorescent bead (**Figure 2.8**). To determine particle localization uncertainty and maximum speed that our system can follow, we tracked a fixed fluorescent bead (\varnothing 100 nm, F-8803, Life Technologies) loaded on an independent xyz piezo stage (P-733K130, PI).^{5,37} The independent stage was programmed to move in a helical pattern (**Figure 2.9a**). At an average speed of $2 \mu\text{m s}^{-1}$, the estimated tracking errors (r.m.s.) were 16.2 nm in x, 16.7 nm in y, and 35.1 nm in z. The localization precision stayed below 45 nm when the particle speed was less than $8 \mu\text{m s}^{-1}$ (**Figure 2.9b**). It should be noted that the fastest molecular motor known today, FtsK, travels at $\sim 7 \mu\text{m s}^{-1}$.³⁸ Other than prescribed motions, we also tracked freely diffusing nanoparticles (\varnothing 100 nm, F-8803, Life Technologies) at various diffusion rates. Diffusion coefficients were estimated from fitting the mean-square displacement (MSD) and compared with the values predicted from the Stokes-Einstein equation. Excellent agreements were seen in a wide range of diffusion coefficients (0.07 - $4.3 \mu\text{m}^2 \text{s}^{-1}$ in **Figure 2.9c**). Whereas a previous 3D-SPT report has successfully tracked particles diffusing at $20 \mu\text{m}^2 \text{s}^{-1}$,¹⁸ we note that diffusion coefficient of a free receptor complex on the cell membrane is roughly on the order of $0.02 \mu\text{m}^2 \text{s}^{-1}$,³⁹ and the fast diffusion coefficient of proteins in cytosol is on the order of $5 \mu\text{m}^2 \text{s}^{-1}$.⁴⁰ Our system thus has no problem to probe rapid molecular transport dynamics inside cells.

2.4.2 Temporal Resolution

Temporal resolution of our tracking system is defined as how fast the particle position is discerned in 3D space with reasonable localization accuracy. Although our control loop period is 1-5 ms, we emphasize that our temporal resolution can be

significantly better than 1 ms by outputting the individual photon event data (Time Tag) from the TCSPC board

(while the control loop period remains at 1-5 ms). In offline analysis trajectories can be resampled with temporal resolution down to 50 μs if the particle has a sufficiently high brightness (**Figure 2.10**). In this condition the trajectory is plotted from a combination of the original control loop rate voltage outputs and n-samples of higher time resolution localizations relative to the current beam position. Localizations are performed using re-binned histograms with photons arriving only within the super-sampled time period.

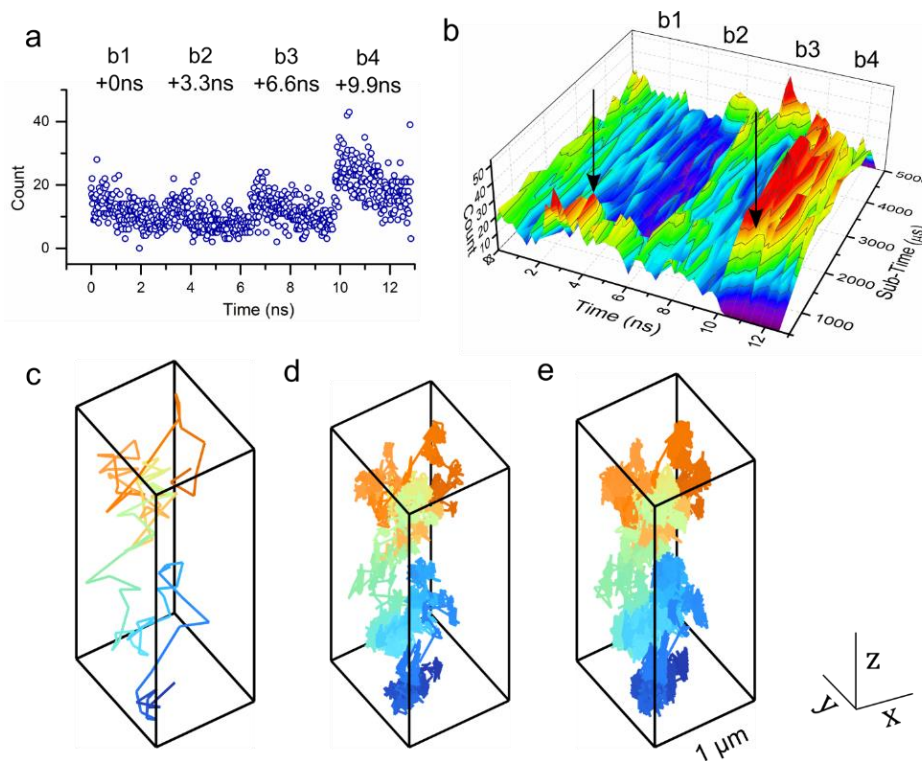


Figure 2.10 | 50 μs Time resolution

(a) Example photon count histogram sampled from a single control loop period of 5 ms. (b) The same photon count data resampled with 200 μs time bins and displayed as a 2D surface (c,d,e). A 0.5 second long trajectory sampled with 5 ms, 100 μs , and 50 μs time resolution, respectively.

To demonstrate resolution down to 50 μs bright nanoparticle trajectories were measured and reconstructed using individual photon count data. $\varnothing 40$ nm fluorescent microspheres (F8770, Life Technologies) were tracked in a 50% wt. glycerol solution under free diffusion. The individual photon count data stored in the FIFO was saved and analyzed in post-processing to reconstruct trajectories with higher temporal sampling. Using sufficient laser power (3 mW per beam) a photon count rate between 1-2 MHz was achieved, which corresponds to between 50-100 photons per localization at 50 μs time resolution. We have no problem to localize the particle with this number of photons as useful signal counts for each beam are 12-25 photons whereas background noise, even in the worst condition, is only 0.5 photons per beam (for 40 kHz background during live cell imaging). The 2D surface in Figure 2.10b has an x-axis with the micro-time in nanoseconds and y-axis is the resampled histogram time with 200 μs resolution. The black arrows denote a sudden shift in beam intensities resulting from the particle movement during the 5 ms integration period. A perfectly centered and stationary particle would appear as four ridges along the y axis of the 2D surface.

2.4.3 Tracking Depth

To mimic 3D tracking in a turbid tissue sample, $\varnothing 40$ nm fluorescent beads were fixed within a 9% gelatin gel with 1% intralipid (**Figure 2.11**). When tracking beads undergoing prescribed motion at ~ 10 μm depth, localization uncertainty stayed the same in xy direction but slightly increased in z direction (60 nm). Localization uncertainty further increased to ~ 89 nm at the depths of 100 through 200 μm , while localization uncertainty stayed below 22 nm in xy direction at both depths. This reduction in z localization precision may be due to an elongated molecular detection function (**Figure 2.8**) that occurs when light is focused through scattering samples which may blur the beams along the z dimension⁴¹ and lower the optical contrast signal required to lock onto the target. Despite this slight reduction in

z tracking accuracy at depth, TSUNAMI is capable of maintaining better than 100 nm axial localization through 200 μm of a scattering sample.

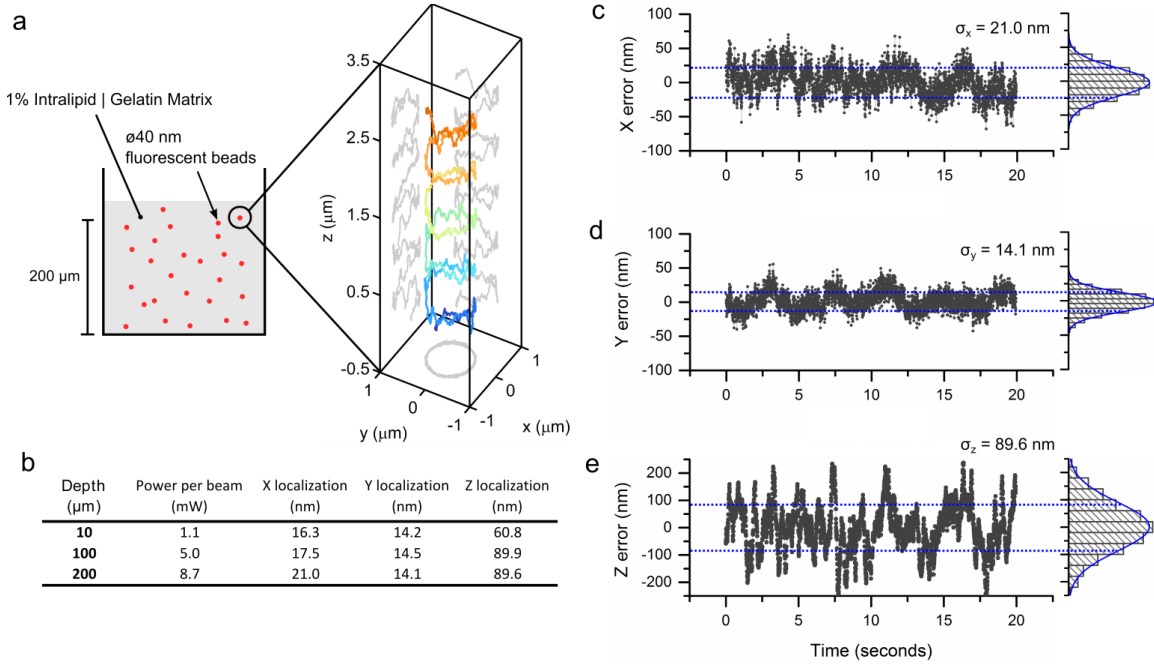


Figure 2.11 | TSUNAMI Depth Characterization

(a) $\varnothing 40$ nm fluorescent beads (F-8770, Life Technologies) were prepared in a matrix of 1% Intralipid and 9% gelatin to mimic a turbid tissue sample. Directed motion was performed as described previously (Figure 2.9) with an independently controlled 3D piezo stage (b) Helical directed trajectories were measured at three different depths all with a mean velocity of $1.0 \mu\text{m s}^{-1}$. Trajectories were recorded at 10 μm , 100 μm , and 200 μm past the coverslip. As expected required excitation power increases with increasing depth, while localization accuracy decreases. X and Y localization suffer only a minor decrease, from ~ 16 nm to ~ 21 nm rms whereas the Z localization experiences a slightly increased reduction in precision from ~ 60 nm to ~ 89 nm rms. This reduction in Z localization can be attributed to an elongated PSF that occurs when light is focused through scattering samples that effectively blurs the beams along z and lowers the optical contrast signal required to lock onto the target. (c,d,e) Localization error values recorded at 200 μm depth for x,y, and z dimensions respectively. Histograms are displayed to the right for each curve. It can be seen that these distributions can be fit very accurately to a normal distribution indicating that there are no systematic errors or instrument artifacts corrupting the localization even at a depth of 200 μm into the scattering sample.

2.4.4 Localization versus Photon Signal

A sample of $\varnothing 40$ nm fluorescent red beads fixed in agarose was used to evaluate localization precision as a function of number of detected photons (**Figure 2.12**). Laser power was increased (5 mW per beam) compared to live cell imaging (2 mW per beam) to increase photobleaching rate and capture the entire range of detectable signals (750 kHz to 100 kHz). A sliding window of 2 seconds width was used to generate the graph, dependent axis values are the mean photon count over the window. Fitting was done with a power function of the form, $\sigma \propto N^{-1/2}$.

Here a fixed bead sample was used as opposed to directed motion to eliminate any potential artifacts from an independent motion stage, and simplify the data analysis. The localization precision for a fixed bead is $\sim 50\%$ better than in the dynamic case ($> 2 \mu\text{m s}^{-1}$) for a given photon signal (**Figure 2.9**) however the power law relationship still remains true in both cases demonstrating that this localization process is photon-limited with an approximate cutoff at 500 detected photons per loop period (i.e. 100 kHz). The z axis suffers from increased localization uncertainty, due to xy spatially variant error function. Ways to improve upon this would be to use MLE based estimators²⁰. Future work will be to improve the z localization to reach a photon-limited precision.

It should be noted that for live cell experiments the photons used for localization starts in the range of 2000-4000 photons and over 10 minutes decays to ~ 1000 -2000 photons. Therefore, it is expected that a loss of accuracy of approximately 30% occurs over a typical live cell trajectory period. Generally, the localization accuracy will remain better than 20 nm in xy and better than 50 nm in z over the entire trajectory.

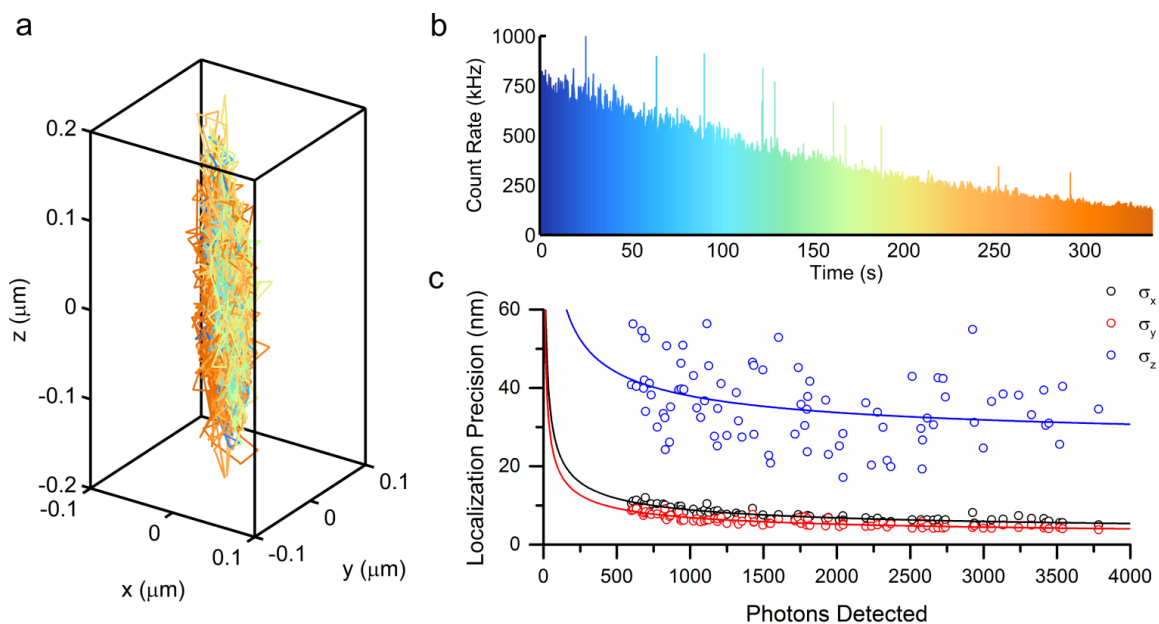


Figure 2.12 | Photon-limited localization precision.

(a) Trajectory of a fixed bead 20 μm past the coverslip tracked for 350 seconds. (b) photon count graph. (c) Scatter plot of localization accuracy in three dimensions for every time point in the trajectory, plotted as a function of detected photons, using a 4.5 ms collection time.

2.4.5 Measurement of Lifetime

Fluorescence lifetime can be simultaneously recorded during tracking by using every photon arrival event as described in **Figure 2.10**. Both excitation regimes were performed using the same laser power, gain, and concentrations (40 pM) in 40% Glycerol solution (**Figure 2.13**). For single excitation measurements 5 decays were recorded and separately fitted. The average lifetime of the Cy5 microspheres under single beam excitation was 1.18 ns. This data was used as a reference from which to measure lifetime accuracy with four excitation beams. A commercial fluorometer (FluoTime 300, PicoQuant) was also used as a reference measurement. Four beam excitation measurements were performed while tracking, the reported lifetime is an average of 25 separately fitted data points from a 2.5 second trajectory (lifetime bin of 100 ms and tracking loop period

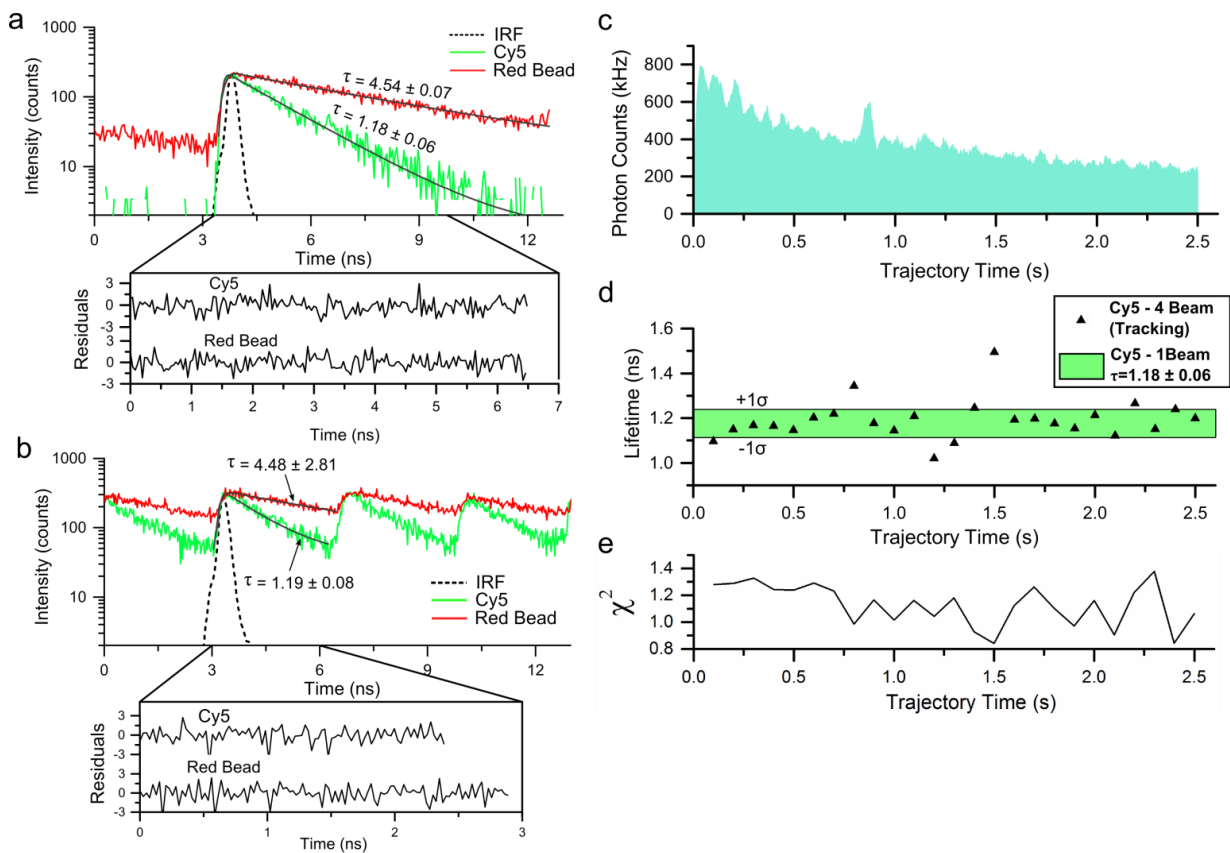


Figure 2.13 | Simultaneous Measurement of Lifetime while Tracking

(a) Single beam excitation and (b) 4 beam excitation measurements using time-correlated single-photon counting (TCSPC) with two different fluorophores, Cy5 labelled microspheres ($\varnothing 500$ nm, PS500-S5-1 NANOCS) and red fluorescent microspheres ($\varnothing 40$ nm, F8770, Life Technologies). (c) Photon counts for the 2.5 second Cy5 bead trajectory. (d) Lifetime fit versus time for 100 ms rolling window. (e) Chi squared values from the fit for each data point in the trajectory.

of 5 ms). Fitting was performed using a least-squares minimization method with a Gaussian convolved exponential model,⁴² the window size for fitting was the same for all data points in each trajectory. Figure 2.13 a and b expansion graphs show residuals for each fit within the windowed region.

Even for low excitation power (<1 mW total) photo-bleaching is rapid due to surface conjugation of the dye onto the microsphere, an oxygen scavenger could be used to reduce bleaching and extend trajectory length. (Figure 2.13c). Resulting lifetime fits from

a Cy5 bead trajectory (triangles) plotted against the lifetime measured using only 1 beam excitation showing that the results are statistically similar (**Figure 2.13d**). 75% of the lifetimes calculated from tracking fall within 1 standard deviation of the Cy5 reference data. Even with a 3 fold decrease in photon count signal, from 750 to 250 kHz, the Cy5 bead can be simultaneously tracked and report an accurate and consistent lifetime. The calculated lifetime was found to be 1.19 ± 0.08 ns which agrees with both the reference Cy5 measurement (1.18 ± 0.06 ns), and the fluorometer (1.11 ± 0.01 ns).

From comparing single beam and four beam excitation it is clear that tracking short lifetime fluorophores (< 2 ns) such as Cy5 is feasible, the lifetime extracted from tracking consistently matched reference measurements. However for fluorescence decays longer than the time gate (> 3.3 ns) such as red fluorescence beads, the tracking data is inconsistent. The lifetime from tracking red beads was found to be 4.48 ± 2.81 ns, compared with 4.54 ± 0.07 ns for a single excitation reference. The mean is close to the reference; however the standard deviation is two orders of magnitude higher. The measurement inaccuracy for long lifetimes arises primarily from fluorescence crosstalk in each of the four time gates. It should be noted that, although crosstalk is an issue for lifetime measurements, it has only a minor effect on tracking stability and accuracy even for long fluorescence decays greater than the time gate. During tracking a fluorescence correction factor is applied to subtract the contribution from each of the previous time gates. Since the tracking localization algorithm is based on a simple intensity ratio and proportional control the effect crosstalk can be removed with almost no loss in localization or controller stability. By contrast, least-squares based lifetime fitting methods are highly sensitive to signal artifacts,⁴³ and so applying a similar correction factor to measure fluorescence lifetime does not yield an accurate result. Methods to overcome this limitation for lifetime measurements using this tracking system would be to extend the time gate using a lower repetition rate laser source

in conjunction with longer physical delay lines, or to investigate computational methods for deconvolution of the TCSPC signal with four excitation beams.

The dead-time of the TCSPC board can result in pulse pileup artifacts. Typically this artifact is only a concern for high emission rates (enough to interfere with the dead-time). Our highest photon detection rate for 1 MHz count rate and 76 MHz laser repetition rate is 0.013, it has been shown that pulse pile-up effects will affect PMT measurements when the detection rate is above ~ 0.1 .⁴⁴ Our highest detection rate is still 10 times less than the threshold for dead time and pulse pileup effects to become significant, so we believe our system has no artifacts introduced at our current range of emission rates with our TCSPC system.

2.5 REFERENCES

1. Saxton, M. J. & Jacobson, K. Single-particle tracking: applications to membrane dynamics. *Annu. Rev. Biophys. Biomol. Struct.* **26**, 373–99 (1997).
2. Fakhri, N. *et al.* High-resolution mapping of intracellular fluctuations using carbon nanotubes. *Science* **344**, 1031–5 (2014).
3. Lowe, A. R. *et al.* Selectivity mechanism of the nuclear pore complex characterized by single cargo tracking. *Nature* **467**, 600–3 (2010).
4. Kusumi, A., Tsunoyama, T. a, Hirose, K. M., Kasai, R. S. & Fujiwara, T. K. Tracking single molecules at work in living cells. *Nat. Chem. Biol.* **10**, 524–32 (2014).
5. Levi, V., Ruan, Q. & Gratton, E. 3-D particle tracking in a two-photon microscope: application to the study of molecular dynamics in cells. *Biophys. J.* **88**, 2919–28 (2005).
6. Cang, H., Xu, C. S., Montiel, D. & Yang, H. Guiding a confocal microscope by single fluorescent nanoparticles. *Opt. Lett.* **32**, 2729–31 (2007).
7. Yildiz, A. *et al.* Myosin V walks hand-over-hand: single fluorophore imaging with 1.5-nm localization. *Science* **300**, 2061–5 (2003).
8. Gelles, J., Schnapp, B. & Sheetz, M. Tracking kinesin-driven movements with nanometre-scale precision. *Nature* **331**, 450–453 (1988).
9. Fujiwara, T., Ritchie, K., Murakoshi, H., Jacobson, K. & Kusumi, A. Phospholipids undergo hop diffusion in compartmentalized cell membrane. *J. Cell Biol.* **157**, 1071–81 (2002).
10. Dahan, M. *et al.* Diffusion dynamics of glycine receptors revealed by single-quantum dot tracking. *Science* **302**, 442–5 (2003).

11. Andrews, N. L. *et al.* Actin restricts FcεRI diffusion and facilitates antigen-induced receptor immobilization. *Nat. Cell Biol.* **10**, 955–63 (2008).
12. Park, H. Y. *et al.* Visualization of dynamics of single endogenous mRNA labeled in live mouse. *Science* **343**, 422–4 (2014).
13. Shav-Tal, Y. *et al.* Dynamics of single mRNPs in nuclei of living cells. *Science* **304**, 1797–800 (2004).
14. Huang, B., Jones, S. A., Brandenburg, B. & Zhuang, X. Whole-cell 3D STORM reveals interactions between cellular structures with nanometer-scale resolution. *Nat. Methods* **5**, 1047–1052 (2008).
15. Arhel, N. *et al.* Quantitative four-dimensional tracking of cytoplasmic and nuclear HIV-1 complexes. *Nat. Methods* **3**, 817–24 (2006).
16. Mason, T. G. & Weitz, D. A. Optical Measurements of Frequency-Dependent Linear Viscoelastic Moduli of Complex Fluids. *Phys. Rev. Lett.* **74**, 1250–1253 (1995).
17. Wirtz, D. Particle-tracking microrheology of living cells: principles and applications. *Annu. Rev. Biophys.* **38**, 301–26 (2009).
18. Welsher, K. & Yang, H. Multi-resolution 3D visualization of the early stages of cellular uptake of peptide-coated nanoparticles. *Nat. Nanotechnol.* **9**, 198–203 (2014).
19. Wells, N. P. *et al.* Time-resolved three-dimensional molecular tracking in live cells. *Nano Lett.* **10**, 4732–7 (2010).
20. Sahl, S. J., Leutenegger, M., Hilbert, M., Hell, S. W. & Eggeling, C. Fast molecular tracking maps nanoscale dynamics of plasma membrane lipids. *Proc. Natl. Acad. Sci.* **107**, 6829–6834 (2010).
21. Thompson, M. a, Lew, M. D., Badiestostami, M. & Moerner, W. E. Localizing and tracking single nanoscale emitters in three dimensions with high spatiotemporal resolution using a double-helix point spread function. *Nano Lett.* **10**, 211–8 (2010).
22. van den Broek, B., Ashcroft, B., Oosterkamp, T. H. & van Noort, J. Parallel nanometric 3D tracking of intracellular gold nanorods using multifocal two-photon microscopy. *Nano Lett.* **13**, 980–6 (2013).
23. Cang, H., Shan Xu, C. & Yang, H. Progress in single-molecule tracking spectroscopy. *Chem. Phys. Lett.* **457**, 285–291 (2008).
24. Helmchen, F. & Denk, W. Deep tissue two-photon microscopy. *Nat. Methods* **2**, 932–40 (2005).
25. Kis-Petikova, K. & Gratton, E. Distance measurement by circular scanning of the excitation beam in the two-photon microscope. *Microsc. Res. Tech.* **63**, 34–49 (2004).
26. McHale, K., Berglund, A. J. & Mabuchi, H. Quantum dot photon statistics measured by three-dimensional particle tracking. *Nano Lett.* **7**, 3535–9 (2007).
27. Kim, K. H. *et al.* Multifocal multiphoton microscopy based on multianode photomultiplier tubes. *Opt. Express* **15**, 11658–78 (2007).
28. Liu, C. *et al.* 3D single-molecule tracking using one- and two-photon excitation microscopy. *Proc. SPIE* **8950**, 1–9 (2014).

29. Cang, H., Wong, C. M., Xu, C. S., Rizvi, A. H. & Yang, H. Confocal three dimensional tracking of a single nanoparticle with concurrent spectroscopic readouts. *Appl. Phys. Lett.* **88**, 223901 (2006).
30. Ji, N., Magee, J. & Betzig, E. High-speed, low-photodamage nonlinear imaging using passive pulse splitters. *Nat. Methods* 1–6 (2008).
31. Cheng, A., Gonçalves, J. T., Golshani, P., Arisaka, K. & Portera-Cailliau, C. Simultaneous two-photon calcium imaging at different depths with spatiotemporal multiplexing. *Nat. Methods* **8**, 139–42 (2011).
32. Katayama, Y. *et al.* Real-time Nanomicroscopy via Three-Dimensional Single-Particle Tracking. *Chemphyschem* **10**, 2458–2464 (2010).
33. Dertinger, T. *et al.* Two-focus fluorescence correlation spectroscopy: a new tool for accurate and absolute diffusion measurements. *Chemphyschem* **8**, 433–43 (2007).
34. Germann, J. A. & Davis, L. M. Three-dimensional tracking of a single fluorescent nanoparticle using four-focus excitation in a confocal microscope. *Opt. Express* **22**, 9830–9834 (2014).
35. Negrean, A. & Mansvelder, H. D. Optimal lens design and use in laser-scanning microscopy. **5**, 11277–11291 (2014).
36. Zinter, J. P. & Levene, M. J. Maximizing fluorescence collection efficiency in multiphoton microscopy. **19**, 5480–5486 (2011).
37. Juette, M. F. & Bewersdorf, J. Three-Dimensional Tracking of Single Fluorescent Particles with Submillisecond Temporal Resolution. *Nano Lett.* 4657–4663 (2010).
38. Lee, J. Y., Finkelstein, I. J., Crozat, E., Sherratt, D. J. & Greene, E. C. Single-molecule imaging of DNA curtains reveals mechanisms of KOPS sequence targeting by the DNA translocase FtsK. *Proc. Natl. Acad. Sci. U. S. A.* **109**, 6531–6 (2012).
39. Pyenta, P. S., Schwille, P., Webb, W. W., Holowka, D. & Baird, B. Lateral Diffusion of Membrane Lipid-Anchored Probes before and after Aggregation of Cell Surface IgE-Receptors. *J. Phys. Chem. A* 8310–8318 (2003).
40. Griffin, E., Odde, D. & Seydoux, G. Regulation of the MEX-5 gradient by a spatially segregated kinase/phosphatase cycle. *Cell* **146**, 955–68 (2011).
41. Hayakawa, C., Venugopalan, V., Krishnamachari, V. & Potma, E. Amplitude and Phase of Tightly Focused Laser Beams in Turbid Media. *Phys. Rev. Lett.* **103**, 43903 (2009).
42. Warren, S. C. *et al.* Rapid Global Fitting of Large Fluorescence Lifetime Imaging Microscopy Datasets. *PLoS One* **8**, (2013).
43. Maus, M. *et al.* An experimental comparison of the maximum likelihood estimation and nonlinear least-squares fluorescence lifetime analysis of single molecules. *Anal. Chem.* **73**, 2078–86 (2001).
44. Pating, M., Wahl, M., Kapusta, P. & Erdmann, R. Dead-time effects in TCSPC data analysis. *Proc. SPIE* **6583**, 658307-658307–10 (2007).

Chapter 3: Tracking Endothelial Growth Factor (EGF) Complexes in Live Cells with TSUNAMI²

3.1 INTRODUCTION

Here we used the endocytosis and subcellular trafficking of Endothelial Growth Factor Receptor (EGFR) complexes in A431 monolayer culture and tumor spheroids as a model system for instrument validation of TSUNAMI¹. EGFR is a relevant model system to validate 3D single particle tracking (SPT) techniques, as the trafficking and motion patterns of EGF are often dysregulated in cancerous tissues,² requiring a high spatial and temporal resolution microscope to detect differences. The following sections will outline the experiments performed in live cells and spheroids. We choose spheroids as an additional model system to validate deep EGF tracking up to 100 μm through scattering cells. Finally, we demonstrate a trajectory segmentation algorithm to classify various motion patterns in the live cell trajectories with the aim to eventually detect cancerous cells based on 3D SPT trajectories³.

3.2 EGF TRACKING IN LIVE CELLS

3.2.1 Preparation of samples for EGF tracking.

EGFR-overexpressed A431 skin cancer cell was purchased from ATCC and cultured in DMEM (Dulbecco's Modified Eagle Medium, Cat. No. 11995-065, Life technologies) supplemented with 5% FBS (fetal bovine serum, Cat. No. SH30071, Thermo scientific). The cell cultures were kept in humidified atmosphere with 5% CO_2 in air at 37°C as previously described⁴. Single suspensions were prepared by mild enzymatic

² Portions of this chapter (section 3.6) were adapted from: Y.-L. Liu, E.P. Perillo, C. Liu, P. Yu, C.-K. Chou, M.-C. Hung, A.K. Dunn, H.-C. Yeh, "Segmentation of 3D Trajectories Acquired by TSUNAMI Microscope: An Application to EGFR Trafficking," *Biophysical Journal*, vol. 111, issue 10, p2214-2227 (2016). E.P.P. designed and built the tracking microscope. E.P.P. and Y.-L.L. carried out the experiments and processed the data.

dissociation using a trypsin/EDTA solution. For EGFR tracking in monolayer cells, A431 cells were seeded onto optical imaging 8-well chamber slides (Nunc™ Lab-Tek™ II Chamber Slide™, Cat. No. 154534, Thermo Scientific) with the cell density of 1×10^5 cells per well and allowed to adhere overnight (**Figure 3.1**). In spheroid model, A431 cells were seeded into agarose-coated 96-well plate with the cell density of 125 cells per well for 96 hours incubation. Both monolayer cells and spheroids were used for EGFR tracking in live cells.

A431 cells were expanded in flasks and the dissociated into single-cell suspension with trypsin treatment. For EGFR tracking in monolayer cells, the cells from suspension were directly seeded into chamber slides. For spheroids, the suspended single cells were seeded into agarose-coated and incubated for 96 hours to form spheroids. After serum starvation, the spheroids were transferred to chamber slides for membrane staining and EGFR labeling.

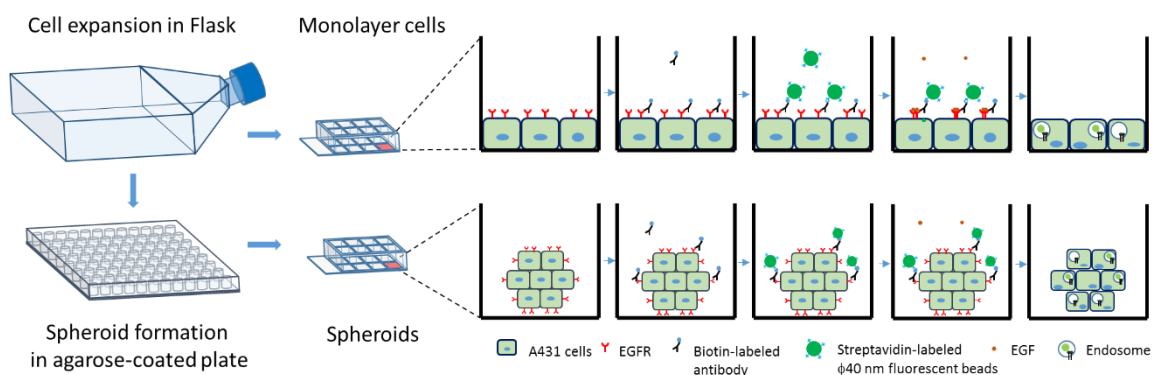


Figure 3.1 | Preparation of specimen for EGF Tracking

Both monolayer cells and spheroids were kept for additional 24 hours under serum-starvation condition before EGFR tracking. Plasma membrane was stained with CellMask™ and surface EGFRs were labeled with fluorescent nanoparticles (see

schematic processes in **Supplementary Fig. 8**). In monolayer samples, cells were labeled using CellMask™ Deep Red Plasma membrane Stain (1:1000 dilution in DMEM; Cat. No. C10046, Life technologies) for 10 minutes at 37°C. In spheroids, we carefully collected spheroids from 96-well plate using micropipettes and transferred them into 8-well chamber slides (8 to 10 spheroids per well). We stained spheroids with higher concentration of CellMask™ Deep Red (1:500 dilution) for 1 hour at 37 °C because of the compact structure of spheroids. To label EGFRs with fluorescence, the cells were incubated with 1.5% BSA solution (1.5% bovine serum albumin, Cat. No. S7806, in PBS) for 15 minutes at 37°C, and then EGFRs were recognized with biotin-labeled anti-EGFR antibodies (200 ng ml⁻¹ in 1.5% BSA solution; Epidermal Growth Factor Receptor Ab-3, Cat. No. MS-311-B, Thermo Scientific) for 15 minutes at 37°C. The antibody solution was removed and cells were washed twice using PBS. The stock solution of streptavidin-labeled \varnothing 40 nm fluorescent nanoparticles (FluoSpheres® Streptavidin-Labeled Microspheres, \varnothing 40 nm, red fluorescent, Cat. No. F8770, Life Technologies) was sonicated for 10 minutes and then diluted to 100 pM in DMEM. This solution was added into samples for 5 minutes at 37°C, and the antibody-recognized EGFRs were visualized with the fluorescent nanoparticles. The samples were washed twice with PBS to remove unbound fluorescent nanoparticles. After labeling plasma membrane and EGFRs, we immediately put slides on our microscope and initiated the endocytosis of EGFR with DMEM containing 10 ng ml⁻¹ EGF (recombinant human epidermal growth factor, Cat. No. PHG0311L, Life technologies). The internalization of fluorescent labeled EGFRs were observed after the stimulation of EGFs (**Supplementary Fig. 9**). Most of surface EGFRs were internalized into cytosol in 30 minutes after the stimulation of EGF⁵, so we typically measured 2 to 4 trajectories from each well in 20 minutes and switched to another initiated sample. The volumes of all solutions and washing buffers used in staining were 200 μ l per well. To inhibit endocytosis

of EGFR (**Supplementary Fig. 15**), the spheroids were treated with 2 mM sodium azide (Cat. No. S8032, Sigma-Aldrich) in DMEM medium for 1 hour before the staining processes. Furthermore, cells with fluorescent labeled EGFRs were kept at 4°C for 10 minutes before the stimulation of EGFs to inhibit EGFR internalization.

3.2.2 EGF Monolayer Live Cell Trajectories

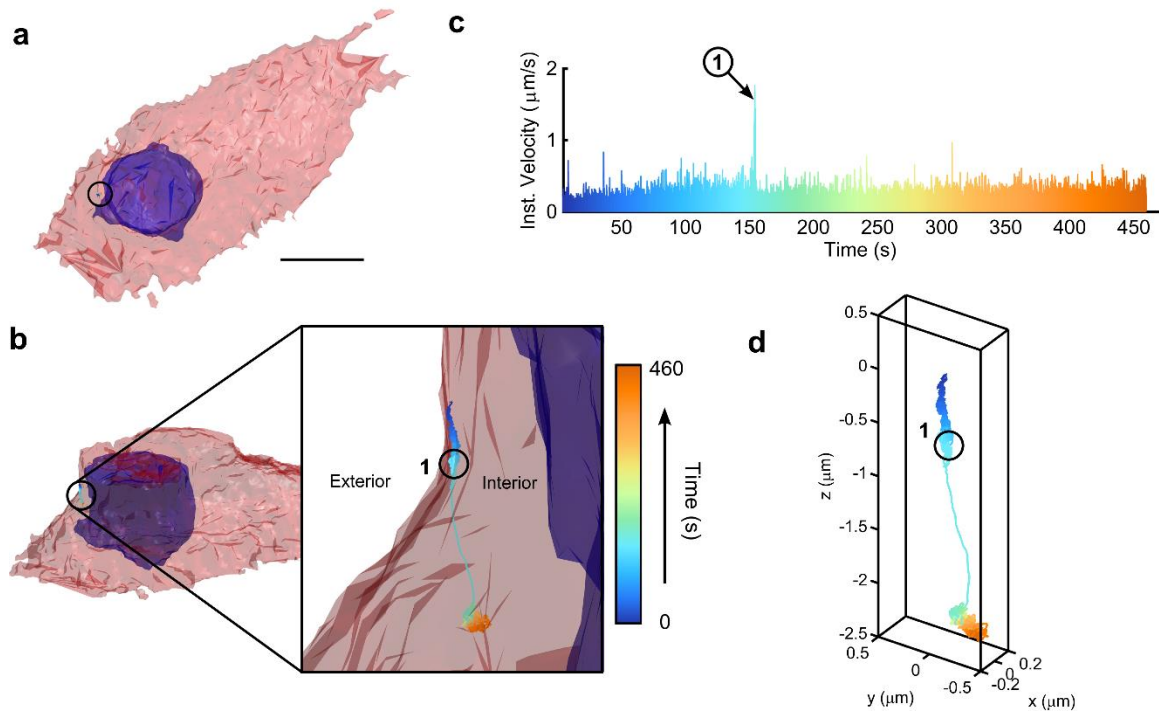


Figure 3.2 | EGF Tracking in Live Monolayer Cells

The capability to track singly-labelled EGF molecules is demonstrated in a live cell environment. **a.** 3D isocontour model of the cell structure with staining for plasma membrane (red) and nuclei (blue). Scale bar is 10 μm . **b.** Cell isocontour model plotted with trajectory overlaid (inset: zoomed view of the particle trajectory, a single fluorescent labelled EGF molecule was tracked for a duration of 460 seconds with rainbow coloration corresponding to time, where blue marks the beginning). **c.** Instantaneous velocity graph with corresponding color scheme. For the first 150 seconds the particle undergoes slow directed diffusion (mean velocity $\sim 0.4 \mu\text{m s}^{-1}$) along the exterior of the cell. A ramp in velocity is observed followed by a period of high average velocity (start denoted as point 1), $\sim 2 \mu\text{m s}^{-1}$, and unidirectional transport of 1 μm . This behavior indicates some form of internalization into the cell or transport within the cell. **d.** Trajectory plotted with no cell contour overlay.

We tracked single nanoparticle ($\varnothing 40$ nm, F-8770, Life Technologies) bound EGFR complexes in monolayer cell cultures (**Figure 3.2**) for periods up to 10 minutes. Prior to SPT, two photon fluorescence images were taken of the surrounding cellular environment. Staining of the plasma membrane and nucleus allows co-registration of the particle trajectory with cellular landmarks. In post processing the trajectory and cellular images are co-registered (**Figure 3.2b**) to visualize EGFR entry pathways.

We found that out of 100 trajectories ~80% of EGFRs had been internalized into the cells within ~6 minutes. We notice transport modes similar to those described in prior work,² (**Figure 3.2d**). The average velocity ($2 \mu\text{m s}^{-1}$) and total transport length (1-2 μm) during internalization are in good agreement with values previously reported.

3.3 DEEP EGF 3D TRACKING IN SPHEROID MODELS

3.3.1 Spheroid formation and initiation protocol for A431 cells

Agarose-coated 96-well plates were used to cultivate A431 spheroids. Each well of a 96-well plate (Cat. No. 130188, Thermo Scientific) was coated with 50 μL sterilized agarose solution (1.5% (wt. per vol.) agarose (Cat. No. A9539-100G, Sigma-Aldrich) in DMEM medium). The spheroids were prepared as previously described⁶ and the plates were incubated for 96 hours in a humidified atmosphere with 5% CO_2 in air at 37°C. To generate spheroids with various sizes, single-cell suspensions from liquid overlay culture were seeded into agarose-coated plates with different cell numbers: 125, 250, 500, 1000, 1500, 2000, 3000 cells per well. The imaging of spheroids after 96 hours incubation was shown in **Figure 3.3**. Considering the penetration of cell membrane dye (CellMask™ Deep Red) and working distance of objective lens, we chose the spheroids with diameter of 90

to 110 μm (cell-seeding density: 125 cells per well) after 96 hours incubation to get the 3D imaging of whole spheroids and trajectories of EGFR tracking.

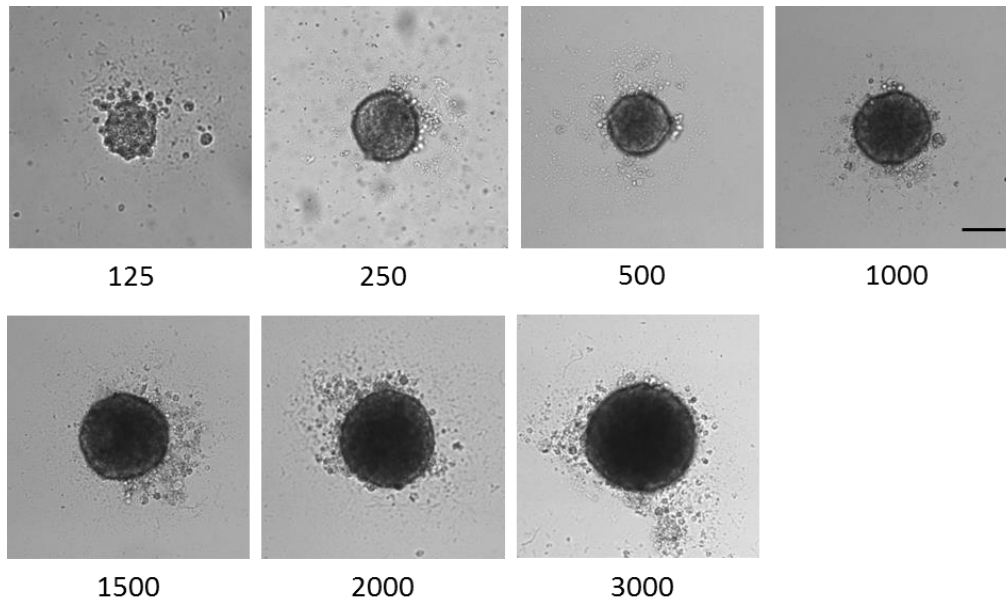


Figure 3.3 | Spheroid Formation Protocol

Bright field imaging of MCTSs formed in liquid overlay from dissociated, exponentially growing A431 skin epidermoid carcinoma cells after a 96-hr initiation interval in agarose-coated 96-well microliter plates. The seeding density was between 125 and 3000 per well in 200 μl of serum-conditioned high glucose standard medium. The concentration to routinely and reproducibly obtain spheroids with a diameter of 90-110 μm is 125 cells per well. Scale bar is 100 μm .

3.3.2 Deep EGF 3D Tracking in Spheroid

For spheroid models we measured EGFR entry pathways at a variety of depths from 20 μm to 100 μm past the coverslip (**Fig. 3.4c**) and found good agreement in terms of the speed and transport length during internalization (**Fig. 3.4d**). Although the required power to obtain clean spheroid images expectedly increased with imaging depth, the total signal count rate (500-800 kHz) and signal to noise remained well within a threshold required for target locking. EGFR trajectories were easily measured at a depth of 100 μm for up to 10 minutes with minimal photo-bleaching.

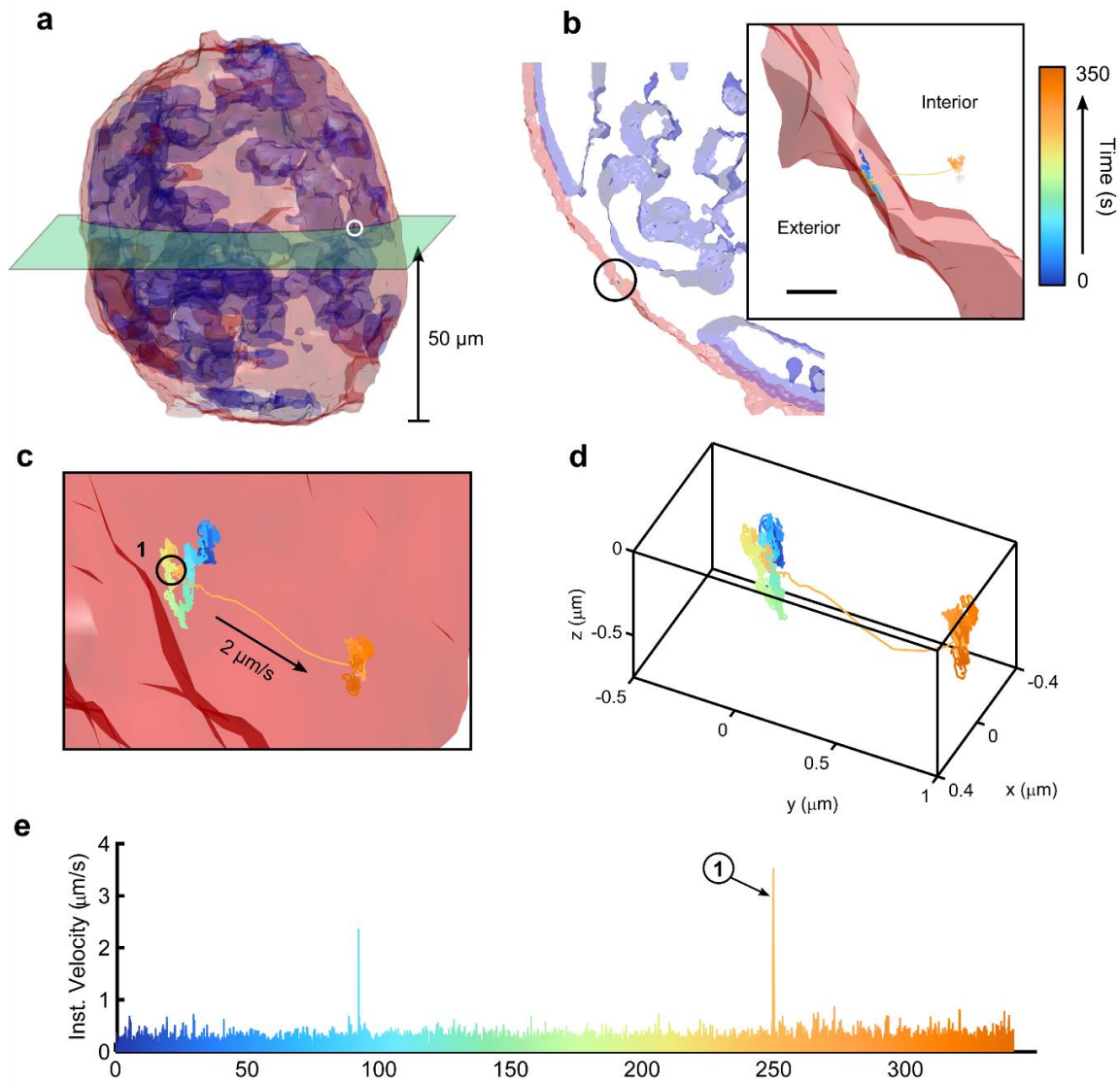


Figure 3.4 | Deep single particle tracking of EGFR in spheroid model.

a. 3D isocontour of a $\varnothing 100 \mu\text{m}$ spheroid taken with 2P LSM staining for plasma membrane (red) and nuclei (blue). The highlighted slice denotes the z-plane (at $50 \mu\text{m}$ depth) where the trajectory was measured, with the white circle marking the location of the trajectory on the spheroid. **b.** Isocontour model of the $\pm 5 \mu\text{m}$ slice taken $50 \mu\text{m}$ deep within the spheroid. Plasma membrane and nuclei are overlaid with the trajectory (black circle), (inset: zoomed view). **c.** Zoomed view of the trajectory, which begins inside the cell with slow displacement (mean velocity $\sim 0.17 \mu\text{m s}^{-1}$) for 250 seconds. Point 1 is where velocity increases to $2 \mu\text{m s}^{-1}$ and is sustained for 0.5 seconds. **d.** Trajectory plotted without cell overlay. **e.** Instantaneous velocity plot over the duration of the trajectory. Scale bar is 600 nm .

Clearly this technique is capable of measuring biologically relevant activity in the high background environment of monolayer and spheroid models with instantaneous transport speeds up to $7 \mu\text{m s}^{-1}$. We emphasize that TSUNAMI is capable of measuring EGFR translocation pathways at depths $10\times$ what was previously possible through highly scattering, cell dense samples. In addition the multi-color, multi-resolution two photon fluorescence imaging functionality is inherently integrated to allow for co-registration of deep trajectories to local cellular/tissue environment in three dimensions.

3.3.3 Additional Deep EGF Trajectories in Spheroids

An example EGFR entry pathway measured with 2P SPT $70\mu\text{m}$ deep in a spheroid model can be seen in **Figure 3.5** First a 3D Iso-contour of a $\varnothing 100 \mu\text{m}$ spheroid was taken with 2P LSM staining for plasma membrane (red) and nuclei (blue) (**Figure 3.5a**). The highlighted slice denotes the z-plane where the trajectory was measured. **Figure 3.5b** shows a close up 3D isocontour plot of a slice $70 \mu\text{m}$ deep into the spheroid taken with 2P LSM. (Inset: Close up view of the trajectory showing its location relative to the plasma membrane). The trajectory is 10 minutes long, color coded by time, with blue denoting the beginning. Points marked 1 and 2 are regions with an onset of high velocity. Point 2 denotes the point where the particle was most likely internalized due to large displacement ($\sim 1\mu\text{m}$) transverse to the membrane. **Figure 3.5c** shows a 3D Trajectory plot with no cell overlay. **Figure 3.5d** is a top view of the trajectory, while **figure 3.5e** is a side view of the trajectory. **Figure 3.5f** is a velocity plot color coded by time showing a stepwise increase in instantaneous velocity over the course of 10 minutes. (Insets: Histograms of regions of the instantaneous velocity plot. The particle starts at $0.33 \mu\text{m s}^{-1}$ mean velocity from time 0-100s, and accelerates to $2.11 \mu\text{m s}^{-1}$ from time 400s-500s.)

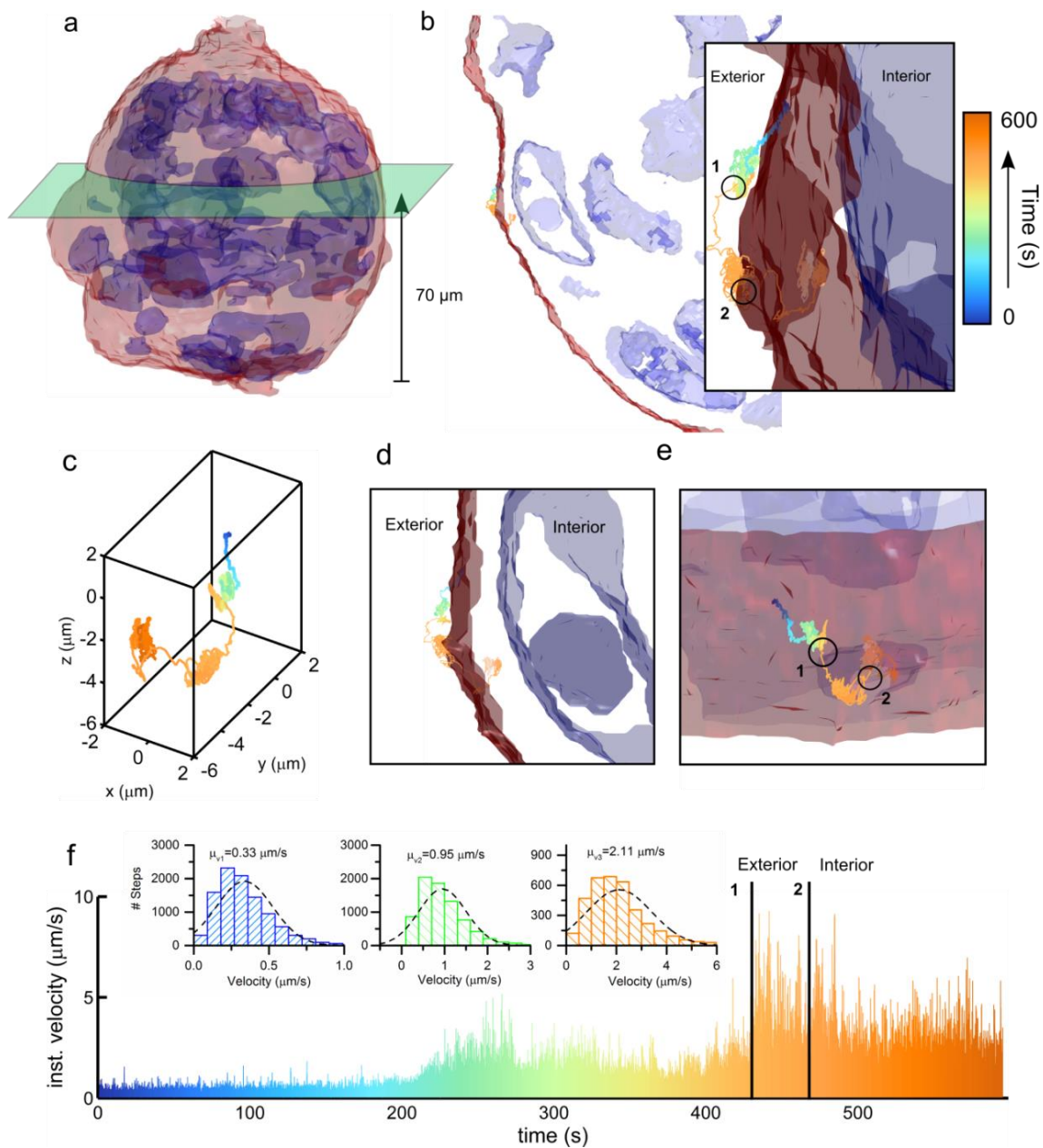


Figure 3.5 | Additional deep single particle tracking in spheroid model.

a. Isocontour of Spheroid **b.** Zoomed in plane where particle trajectory was measured **c.** Trajectory without overlay **d.** Top view **e.** Side view **f.** velocity versus time

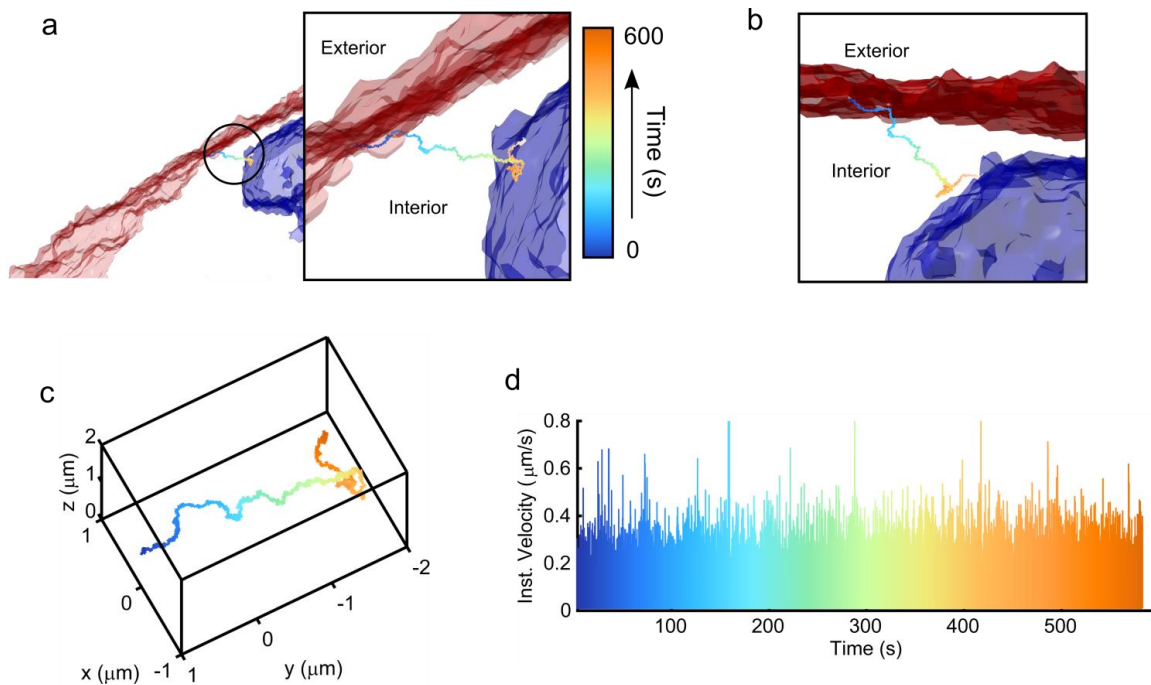


Figure 3.6 | Intra-cellular transport in spheroid model.

An additional EGF trajectory taken in a spheroid model. This example trajectory shows slow diffusive transport in cytosol and interaction with the nucleus. **a.** Isocontour of the zoomed in image stack taken 90 μm deep in a spheroid with cell membrane (red) and nucleus (blue) are overlaid with the trajectory (black circle), (inset: zoomed view of the trajectory). The trajectory begins inside the cell close to the plasma membrane and ends at the nuclear membrane. **b.** Additional close view of the trajectory from top down perspective. **c.** Plot of the trajectory. **d.** Instantaneous velocity plot over the 10 minute duration of the trajectory.

3.4 EGF CONTROL EXPERIMENTS

A series of control experiments were performed to assess the viability of EGF-antibody complexes for internalization, to better determine the frequency and timing of internalization for tracking experiments. A second set of controls were performed to demonstrate that EGF internalization is a biologically relevant activity, and can be inhibited either chemically, or thermally.

3.4.1 EGF Induces internalization of EGFR

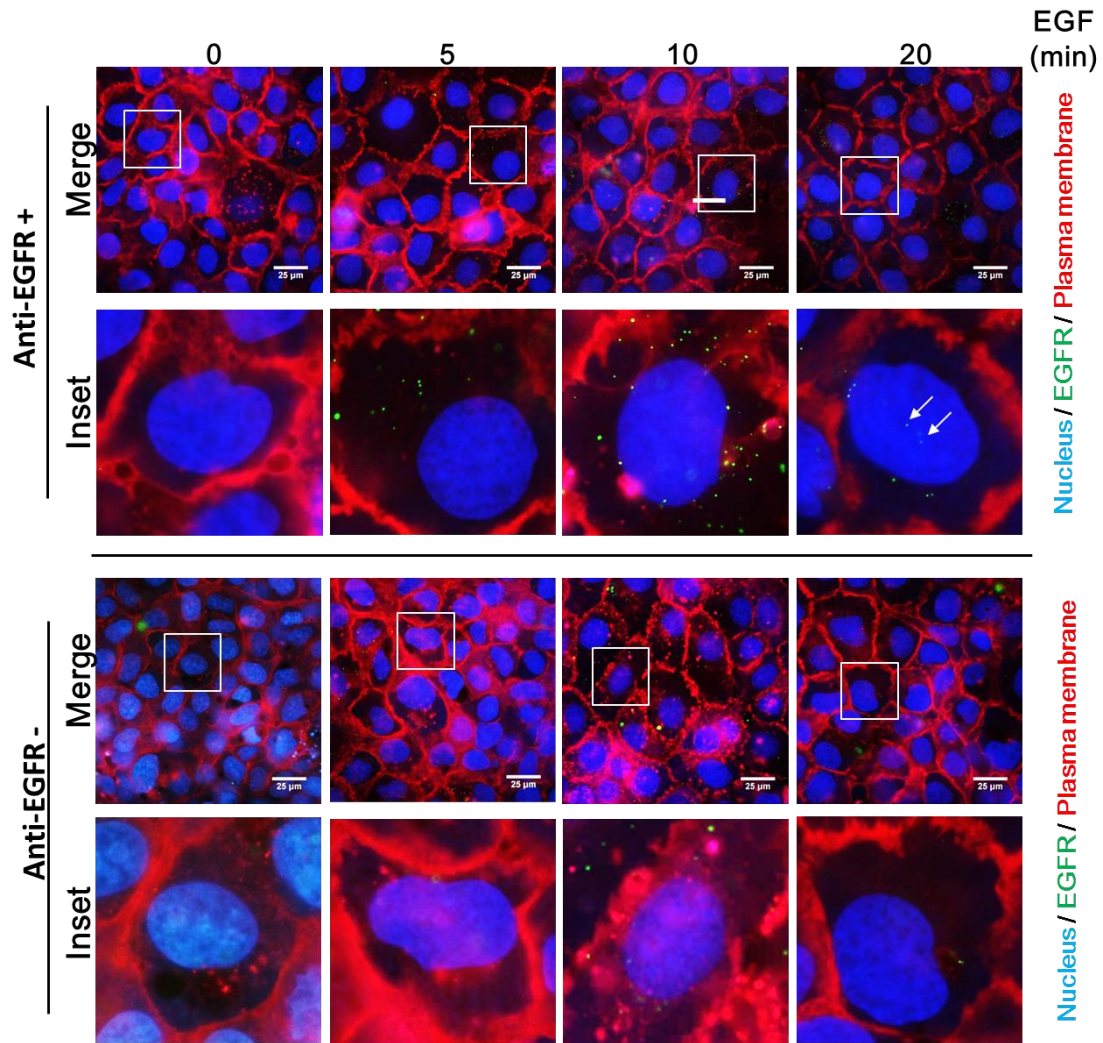


Figure 3.7 | EGF induces internalization of EGFR.

Monolayer A431 cells were exposed to serum-free media overnight, and then their EGFRs were recognized with biotin-conjugated anti-EGFR antibodies, and NeutrAvidin[®] conjugated red fluospheres (F8770, Life Technologies) bound to biotins to label EGFRs. In control group, we didn't label EGFR with anti-EGFR antibodies. After labeling, cells were treated with EGF (20 ng ml^{-1}) for indicated time. The white arrows indicate nuclear translocation of EGFR. The boxed areas are shown in detail in the insets. Scale bar is $25 \mu\text{m}$.

3.4.2 Inhibited Spheroid Trajectories

To evaluate whether the trajectories are representative of biological events or system artifacts we measured trajectories under a control environment with an endocytosis inhibitor, sodium azide, and low temperature ($<20^{\circ}\text{C}$) (**Figure 3.8**). Of the 30 inhibited trajectories we observed no high speed transport modes and only external membrane bound slow diffusion with an average velocity of $\sim 0.2 \mu\text{m s}^{-1}$. The average tracking duration was 500 seconds.

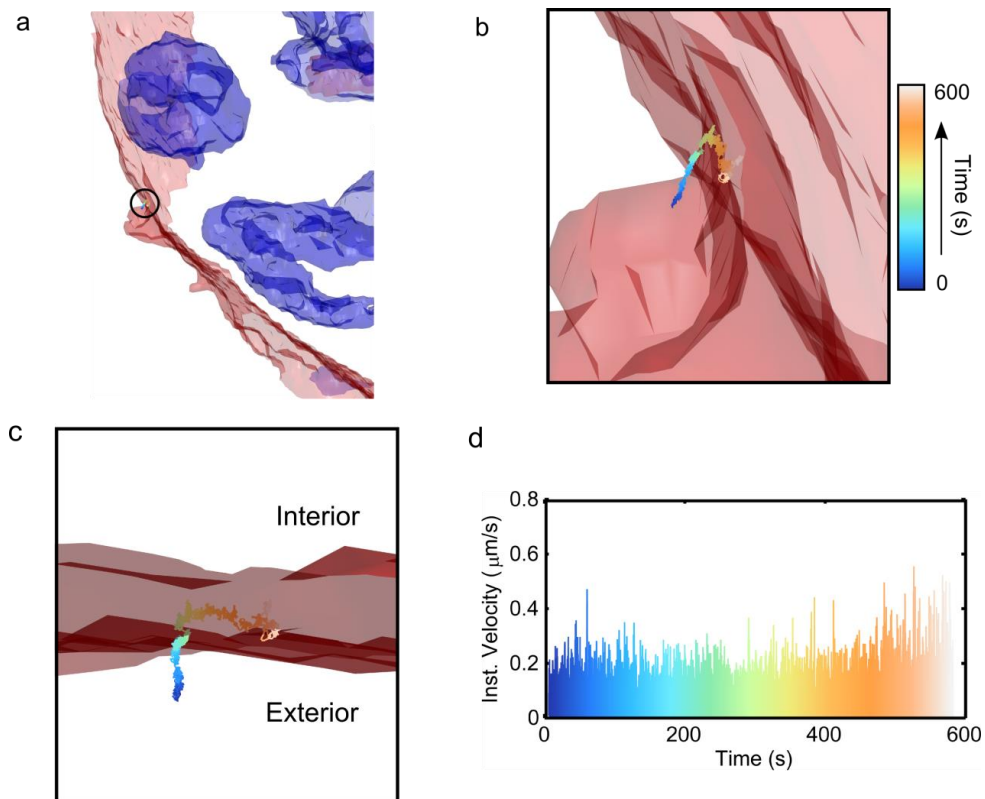


Figure 3.8 | Inhibited spheroid trajectory.

An example EGF trajectory with sodium azide inhibitor in a spheroid model. **a.** Isocontour image with cell membrane (red) and nucleus (blue) are overlaid with the trajectory (black circle) **b,c.** Zoomed images of the trajectory. Over the entire 600 second trajectory the displacement was $\sim 600\text{nm}$ and no entry through the membrane occurred. **d.** instantaneous velocity plot with mean velocity $0.2 \mu\text{m s}^{-1}$.

3.5 TRAJECTORY DATA PROCESSING AND VISUALIZATION

All data processing was performed in Matlab (Mathworks, Natick). Raw data files of the trajectory are saved in binary format and contain positional information and count data for each time point. The data on every photon event can also be saved and resampled for higher time resolution, as explained in **Chapter 2**. Each data point in the raw trajectory is a voltage output from the actuators (xy galvos and z stage) that must be converted to a physical distance. Conversion is performed by multiplying a gain factor for each axis. Trajectories are plotted by simply connecting lines between the points, no further post processing occurs.

2P LSM raw images are read into Matlab from binary files and denoised with a median filter before a 1D interpolation along the Z dimension. To segment the cellular compartments we use a simple intensity threshold technique that converts the image to a binary. Thresholds are selected at each z plane to account for variation in noise and brightness through the z-stack. The binary images are used as a mask to plot the cell isocontour. Because trajectories are measured with the same analog output device as the 2P LSM images they can be directly overlaid with the cell compartment isocontours with no conversion or scaling required.

3.6 TRAJECTORY SEGMENTATION ANALYSIS

We have developed a procedure to perform trajectory segmentation and classification (**Figure 3.9**). This work has been tested on previously measured trajectories in spheroids and is ongoing as a method to classify healthy versus diseased tissues, primarily for the early detection of cancer.

Firstly, a temporal rolling window of length w centered at time s on the trajectory is adopted for calculating the segmented MSD at s ($\text{MSD}_{w,s}$, **Figure 3.9A**). As the motional mode of the tracked particle can vary significantly from one segment to another, a wide

distribution of the segmented MSD curves is expected. We then perform a two-step test (**Figure 3.9B**) to classify the motion of each segment into four modes: (i) directed diffusion, (ii) Brownian diffusion, (iii) confined diffusion and (iv) immobilization. Within each segment, only one of these motional modes is assigned.

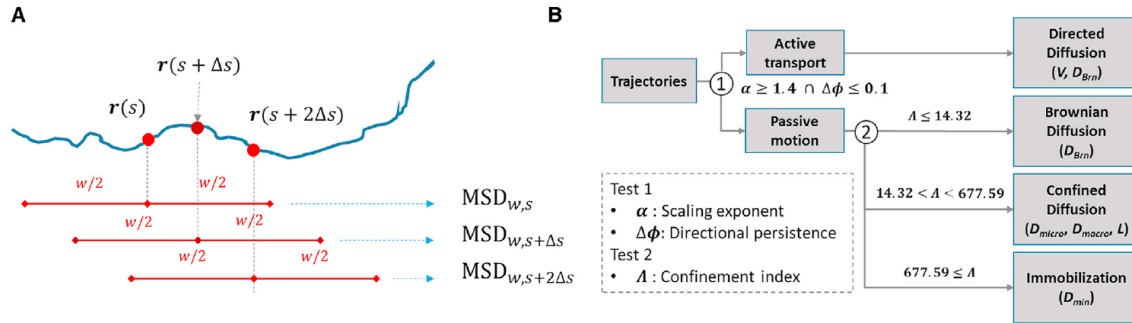


Figure 3.9 | Procedure for segmentation and classification of trajectories

(A) The rolling window analysis is conducted at a given time point s with the length of rolling window of 1.6 s ($w \approx 1.6$ s) and the sliding time step (Δs) of 0.1 s. (B) The transient behaviors of a trajectory are identified using the three classification parameters: scaling exponent of MSD curve (α), directional persistence (D_f), and confinement index (L). The MSD curve of each segment is fitted with the proper model to extract the dynamic parameters including V , D_{Brn} , D_{micro} , D_{macro} , L , and D_{min} .

The first step of test is to differentiate directed motion (active transport) from Brownian diffusion, confined diffusion, and transient immobilization (passive motion) by evaluating two parameters from the segmented trajectories and their derived MSD curves— scaling exponent (α)⁷ and directional persistence ($\Delta\phi$)⁸. By fitting each segmented MSD curve with the following power-law equation⁹, a single α value is obtained and is assigned to each time point s along the trajectory.

$$MSD(t) \sim t^\alpha \quad (1)$$

Directional persistence function ($\Delta\phi$) in a temporal rolling window of length w centered at time s is defined as⁷:

$$\Delta\phi(t) = \langle (\phi(t' + t) - \phi(t'))^2 \rangle^{\frac{1}{2}}, t' \in [s - \frac{w}{2}, s + \frac{w}{2}] \quad (2)$$

where ϕ is the directional vector at each data point. While, each rolling window centered at s generates a directional persistence function $\Delta\phi(t)$, we use the single value, $\Delta\phi(w/4)$, to represent the direction persistence $\Delta\phi$ at s . The time lag of $w/4$ is chosen in consideration of the microtubule bending during a motor-driven event⁷. The $\Delta\phi$ is equal to zero when the motion is unidirectional.

The segment at time s is classified as active transport when $\alpha \geq 1.4$ and $\Delta\phi \leq 0.1$ (Test 1 in **Figure 3.9B**). Otherwise, the segment is classified as passive motion. In the complex intracellular environment, the active transport along microtubules has α values ranging from 1.4 to 2¹⁰. While some biological studies also used the α value of 1.4 as a criterion for classification¹¹, we notice α value of 1.7 was used in a microfluidic experiment⁸. In the same report, the criterion of $\Delta\phi \leq 0.1$ was found suitable to achieve sufficient discrimination between active and passive motion. The threshold values of α and $\Delta\phi$ have also been validated in our simulated movement experiments (SME).

The second step of test is to classify passive motion into Brownian diffusion, confined diffusion and immobilization by evaluating confinement index (Λ) from the segmented trajectories (Test 2 in **Figure 3.9B**). Confinement index (Λ) is defined as:

$$\Lambda = \frac{D_{max}w}{var(r)} \quad (3)$$

where D_{max} is the unconstrained diffusivity of particles and $var(r)$ stands for the variance of particle displacements (r) within a temporal rolling window of length w . In the early reports, confinement index is defined as the ratio of $D_{max}w$ and r_{max}^2 , where r_{max} is the largest displacement from the starting point within the rolling window¹². r_{max}^2 scales

linearly with $D_{max}w$ under Brownian diffusion. But when the particle is confined in a domain of linear size L , r_{max}^2 is limited by L^2 . Thus the value of A becomes significantly larger than that in Brownian diffusion. In **Equation 3**, r_{max}^2 is replaced with $var(r)$ in the A calculation. As a result, A becomes the ratio of the variance of Brownian diffusion ($D_{max}w$) and the variance of trajectory segmented under study ($var(r)$). This modified definition of A has advantage in detecting confinement in a wider class of trapping potential shapes. Two threshold values were selected: $A_{Brn} = 14.32$ and $A_{Im} = 677.59$. Based on these thresholds, trajectories were classified into Brownian diffusion ($A \leq A_{Brn}$), confined diffusion ($A_{Brn} < A < A_{Im}$) and immobilization ($A \geq A_{Im}$).

For trajectory segmentation and classification, the length of temporal rolling window (w) should be sufficiently long to ensure good estimation of α , $\Delta\phi$ and A . On the other hand, the w should be kept short in order to maintain decent temporal resolution. We found that the reasonably short rolling window of 1.6 s (w) can effectively differentiate active transport from passive motion and distinguish confined diffusion from Brownian diffusion. The sliding time step (Δs) for the rolling window analysis is set as 0.1 s, while the time step for position acquisition (Δt) is either 2.5 ms for simulated trajectories or 20 ms for experimental trajectories. In our simulations, we also found that the confinement index of Brownian motion is independent of the rolling window length (w), but the scaling exponent (α) of directed diffusion, the directional persistence ($\Delta\phi$) of directed diffusion, and the confined index (A) of confined diffusion are all functions of the rolling window length.

Figure 3.10 demonstrates an example of how trajectories measured in live cells can be classified according to three distinct motion modes.

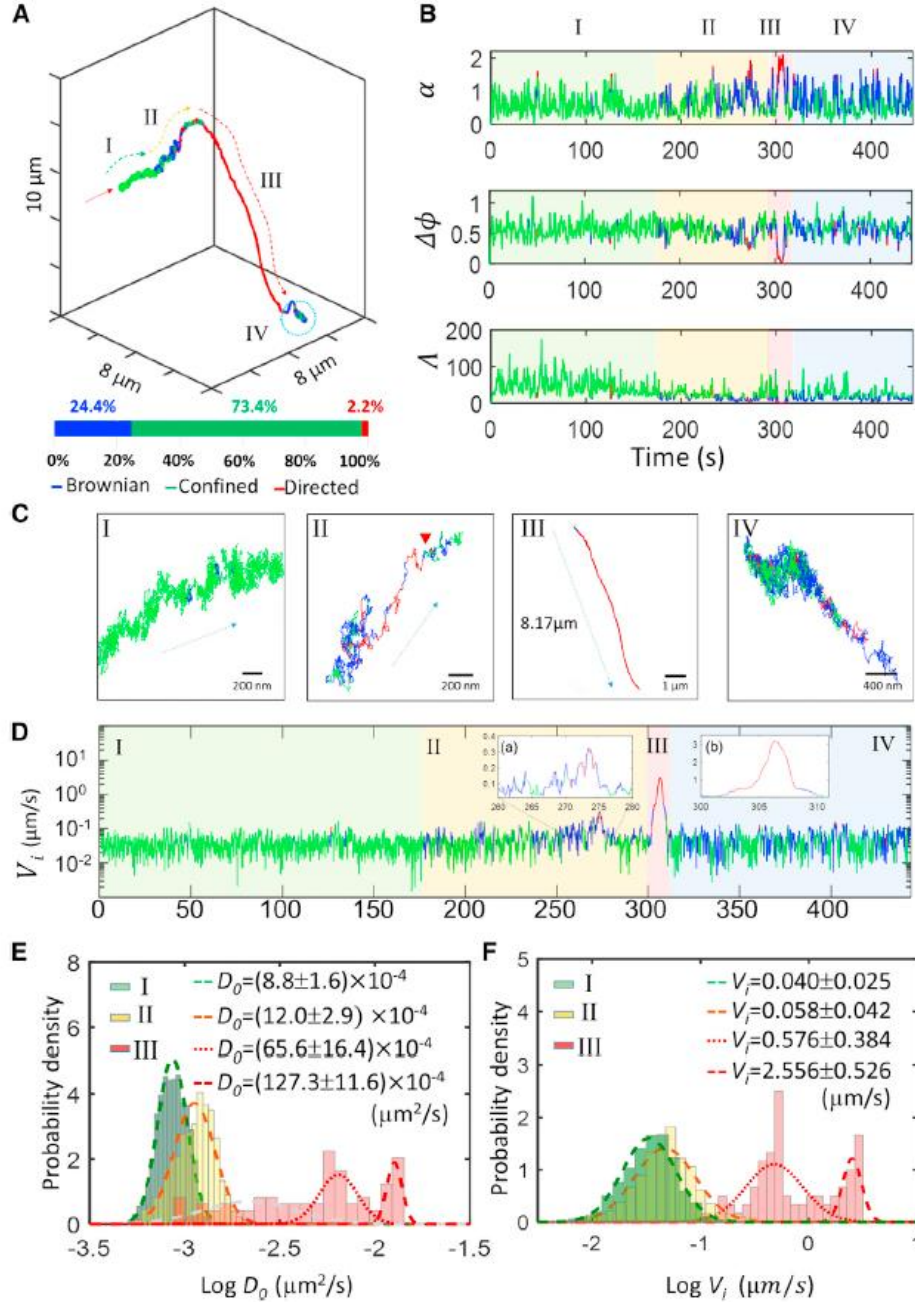


Figure 3.10 | Trafficking from membrane to cytoplasm.

(A) Representative trajectory of EGFR trafficking from cell membrane to cytoplasm. (B) Time traces of the three motion classification parameters (α , $\Delta\phi$, Λ). Corresponding periods of the four phases are color coded in these time traces. (C) Zoom-in views of the four phases. In this case, EGFR complex travelled $8.17\ \mu\text{m}$ into cytoplasm at phase III. (D) Time trace of instantaneous velocity (V_i). (E) Histograms of $\log D_0$ in phases I-III. (F) Histograms of $\log V_i$ in phases I-III. The values shown in (E) and (F) represent the means and standard deviations from Gaussian mixture model fitting.

Based on the demonstrated proof of concept using previously recorded data³, we plan to further this work by applying this classification algorithm to the study of dysregulation in cancerous cell and tissues to establish early detection markers.

3.7 DISCUSSION

Whereas a few reports demonstrated 3D-SPT in monolayer cell cultures using two-photon excitation,^{13,14} to the best of our knowledge high-resolution subsurface particle tracking in three dimensions has never been demonstrated in highly scattering multicellular environments. One recent report demonstrates deep 3D-SPT light sheet microscopy using astigmatism,¹⁵ however the capability is limited by the use of an EMCCD (16 ms temporal resolution), and would prove difficult to implement multicolor tracking or simultaneous lifetime measurement schemes. Furthermore, we expect an astigmatic PSF would have significantly decreased localization precision when tracking at depth ($>10\ \mu\text{m}$).¹⁶

Other than penetration depth, 2P excitation allows us to excite multiple fluorophores simultaneously, which greatly facilitates multi-color detection (**Figure 3.2**).¹⁷ The two factors that determine the fundamental limit of our temporal resolution are the detector and the tracer. The timing resolution (FWHM of the instrument response function) of our detector (H7422P-40, Hamamatsu) is about 230 ps. Whereas this response time is typical in photon-counting detectors, it is still orders of magnitude faster than CCD. It is well known that localization accuracy of a fluorescent particle relies heavily on the brightness and photostability of this fluorescent molecule.¹⁸ Assuming that a bright fluorophore has an emission rate of $10^8\ \text{s}^{-1}$ and 10% of emitted photons are collected, the detected photons could exceed 10^7 per second. As approximately 100 photons are needed for particle position determination with moderate precision, this could mean that the ultimate temporal resolution for SPT is approximately 10 μs . Recently another group reported achieving 10

nm 3D localization precision and 10 μ s temporal resolution in confocal 3D tracking of a giant QD cluster (~40 QDs).¹⁹ As our 3D tracking approach has better collection efficiency (non-descanned detection and the emission light is not split among multiple detectors) we see no potential problem for our system to reach similar temporal resolution and localization precision using a tracer system with ultrahigh emission rate but with a short lifetime.

Despite a shorter time gate of 3.3 ns, demultiplexing of longer lifetime emitters can be performed by applying a fluorescence correction factor in our tracking algorithm (further discussed in **Figure 2.13**). The correction factor allows tracking of lifetimes up to 4.5 ns by subtracting the estimated crosstalk from the previous time gate. The correction factor must be adjusted for fluorophores of different lifetimes. With a correspondingly smaller correction factor we demonstrate tracking a short lifetime emitter, Cy5-tagged beads (1.18 ns), and show that lifetime can be accurately measured (± 0.08 ns) during tracking (**Figure 2.13**). However, for extremely long lifetime emitters, such as quantum dots, or emitters whose lifetime changes dynamically a lower repetition rate source or a pulse picker would be needed, in conjunction with longer physical delay lines.

Moving the beam through the sample instead of moving the sample itself¹⁹⁻²¹ has the additional advantage that beam steering is generally faster than the movement of a potentially heavy stage. Also steering the beam is particularly suitable for applications in neuroscience, such as patching clamping, which requires stationary samples. While the stage response frequencies (10 kHz for the galvo mirrors and 300 Hz for the objective z-piezo stage) do not determine the temporal resolution of our tracking system, they impose an upper limit on the observable particle speeds.²² The way to bypass this limitation in mechanical scanning and completely rule out the possibility that the observed dynamics

are influenced by the objective motion (*via* mechanical coupling through the immersion medium) is to use fast adaptive optical elements in both lateral scan^{21,23} and axial focusing.²⁴

An important characteristic of our tracking microscope lies in the fact that it is readily compatible with a number of fluorescence spectroscopy or microscopy techniques for probing molecular interactions, potentially at the true single-molecule level,²⁵ including FRET²⁶ (*via* lifetime measurements), multi-color single-molecule imaging/spatiotemporal colocalization analysis,²⁷ step counting,^{28,29} and MSD analysis.²³ Since only one detector is used for 3D tracking, additional detectors can be easily added and used for simultaneous, multi-color detection, which can provide a structural overview of the particle's surrounding environment or indicate molecular interactions. On the other hand, it is not straightforward to detect the 2nd color simultaneously on the traditional confocal tracking setups that employ 3-5 detectors for spatial filtering,^{19,20,30} as twice as many detectors and serious alignment effort may be required for multi-color detection. The unique nature of the tetrahedral point spread function allows easily configurable beam spacing which may be optimized for measurements such as 3D pair correlation analysis.³¹

Here we demonstrate a new 2P-3D-SPT microscope (TSUNAMI) that addresses fundamental limitation of deep and high-resolution single-particle tracking in the 3D space¹. Extended from our current tracking results in multicellular models, we are working towards direct *in vivo* 3D-SPT at high spatiotemporal resolution. Our system will allow researchers to explore new questions in receptor transport and dynamic processes directly in 3D tissues.

3.8 REFERENCES

1. Perillo, E. P. *et al.* Deep and high-resolution three-dimensional tracking of single particles using nonlinear and multiplexed illumination. *Nat. Commun.* **6**, 7874 (2015).
2. de Bruin, K. *et al.* Cellular dynamics of EGF receptor-targeted synthetic viruses. *Mol. Ther.* **15**, 1297–305 (2007).
3. Liu, Y. *et al.* Segmentation of 3D Trajectories Acquired by TSUNAMI Microscope : An Application to EGFR Trafficking. *Biophysj* **111**, 2214–2227 (2016).
4. Durr, N. J. *et al.* Two-photon luminescence imaging of cancer cells using molecularly targeted gold nanorods. *Nano Lett.* **7**, 941–5 (2007).
5. Sigismund, S. *et al.* Clathrin-mediated internalization is essential for sustained EGFR signaling but dispensable for degradation. *Dev. Cell* **15**, 209–19 (2008).
6. Friedrich, J., Seidel, C., Ebner, R. & Kunz-Schughart, L. A. Spheroid-based drug screen: considerations and practical approach. *Nat. Protoc.* **4**, 309–24 (2009).
7. Karatekin, E. *et al.* Analysis of Transient Behavior in Complex Trajectories : Application to Secretory Vesicle Dynamics. **91**, 3542–3559 (2006).
8. Sackmann, E., Ra, J. O. & Heinrich, D. Temporal Analysis of Active and Passive Transport in Living Cells. **248103**, 1–4 (2008).
9. Meroz, Y. & Sokolov, I. M. A toolbox for determining subdiffusive mechanisms. *Phys. Rep.* **573**, 1–29 (2015).
10. Fakhri, N. *et al.* High-resolution mapping of intracellular fluctuations using carbon nanotubes. *Science* **344**, 1031–5 (2014).
11. Ahmed, W. W. & Saif, T. A. modulated by mechanical tension. 1–7 (2014). doi:10.1038/srep04481
12. Simson, R., Erin, D. & Jacobson, K. Detection of Temporary Lateral Confinement of Membrane Proteins Using Single-Particle Tracking Analysis. *Biophys. J.* **69**, 989–993 (1995).
13. Levi, V., Ruan, Q. & Gratton, E. 3-D particle tracking in a two-photon microscope: application to the study of molecular dynamics in cells. *Biophys. J.* **88**, 2919–28 (2005).
14. van den Broek, B., Ashcroft, B., Oosterkamp, T. H. & van Noort, J. Parallel nanometric 3D tracking of intracellular gold nanorods using multifocal two-photon microscopy. *Nano Lett.* **13**, 980–6 (2013).
15. Spille, J.-H., Kaminski, T., Königshoven, H.-P. & Kubitscheck, U. Dynamic three-dimensional tracking of single fluorescent nanoparticles deep inside living tissue. *Opt. Express* **20**, 19697–707 (2012).
16. Thompson, M. a, Lew, M. D., Badieirostami, M. & Moerner, W. E. Localizing and tracking single nanoscale emitters in three dimensions with high spatiotemporal resolution using a double-helix point spread function. *Nano Lett.* **10**, 211–8 (2010).
17. Heinze, K. G., Koltermann, a & Schwille, P. Simultaneous two-photon excitation of distinct labels for dual-color fluorescence crosscorrelation analysis. *Proc. Natl. Acad. Sci. U. S. A.* **97**, 10377–82 (2000).

18. Thompson, R. E., Larson, D. R. & Webb, W. W. Precise nanometer localization analysis for individual fluorescent probes. *Biophys. J.* **82**, 2775–83 (2002).
19. Welsher, K. & Yang, H. Multi-resolution 3D visualization of the early stages of cellular uptake of peptide-coated nanoparticles. *Nat. Nanotechnol.* **9**, 198–203 (2014).
20. Wells, N. P. *et al.* Time-resolved three-dimensional molecular tracking in live cells. *Nano Lett.* **10**, 4732–7 (2010).
21. McHale, K., Berglund, A. J. & Mabuchi, H. Quantum dot photon statistics measured by three-dimensional particle tracking. *Nano Lett.* **7**, 3535–9 (2007).
22. Juette, M. F. & Bewersdorf, J. Three-Dimensional Tracking of Single Fluorescent Particles with Submillisecond Temporal Resolution. *Nano Lett.* 4657–4663 (2010).
23. Wang, Q. & Moerner, W. E. Single-molecule motions enable direct visualization of biomolecular interactions in solution. *Nat. Methods* **11**, 555–8 (2014).
24. Juette, M. F., Rivera-Molina, F. E., Toomre, D. K. & Bewersdorf, J. Adaptive optics enables three-dimensional single particle tracking at the sub-millisecond scale. *Appl. Phys. Lett.* **102**, 173702 (2013).
25. Ha, T. *et al.* Single-molecule fluorescence spectroscopy of enzyme conformational dynamics and cleavage mechanism. *Proc. Natl. Acad. Sci. U. S. A.* **96**, 893–8 (1999).
26. Myong, S., Rasnik, I., Joo, C., Lohman, T. M. & Ha, T. Repetitive shuttling of a motor protein on DNA. *Nature* **437**, 1321–5 (2005).
27. Gebhardt, J. C. M. *et al.* Single-molecule imaging of transcription factor binding to DNA in live mammalian cells. *Nat. Methods* **10**, 421–6 (2013).
28. Ulbrich, M. H. & Isacoff, E. Y. Subunit counting in membrane-bound proteins. *Nat. Methods* **4**, 319–21 (2007).
29. Cocucci, E., Aguet, F., Boulant, S. & Kirchhausen, T. The first five seconds in the life of a clathrin-coated pit. *Cell* **150**, 495–507 (2012).
30. Sahl, S. J., Leutenegger, M., Hilbert, M., Hell, S. W. & Eggeling, C. Fast molecular tracking maps nanoscale dynamics of plasma membrane lipids. *Proc. Natl. Acad. Sci.* **107**, 6829–6834 (2010).
31. Hinde, E., Cardarelli, F., Digman, M. A. & Gratton, E. In vivo pair correlation analysis of EGFP intranuclear diffusion reveals DNA-dependent molecular flow. *Proc. Natl. Acad. Sci. U. S. A.* **107**, 16560–16565 (2010).

Chapter 4: Improvements to TSUNAMI and Dual Particle Tracking³

Although Tracking Single-particle Using Nonlinear And Multiplexed Illumination (TSUNAMI) is a robust approach to biological Single Particle Tracking (SPT), as outlined in **Chapters 2 & 3**, there are certain design refinements and improvements that have been made to the system. First, we detail the optical design improvements for the beam multiplexer, which allows for fully independent control of all four beams (**Section 4.1**). An algorithmic technique for improved localization accuracy is detailed in **Section 4.2**. Development towards simultaneous SPT and superresolution microscopy is discussed in **Section 4.3**. Finally, a modification, which allows for two-color dual particle tracking is discussed in **Section 4.4**.

4.1 IMPROVED BEAM MULTIPLEXER DESIGN

The previous beam multiplexer design (**Figure 2.2, Chapter 2**)¹, allowed formation of the tetrahedral point spread function (PSF) through the use of beamsplitters and created temporal offsets using only 2 delay lines. The original design was inspired by passive pulse splitters for 2P microscopy². The benefits of the chosen design were a small number of components, and small space. However, the original design suffered from several drawbacks, including (1) difficult alignment due to non-independent beam paths (2) no ability to independently control collimation of each beam leading to focus offsets (3) large pulse dispersion due to thick cube beamsplitters, and (4) limited wavelength operating range (780-820 nm) due to poor performance of cube beamsplitters.

An improved design (**Figure 4.1**) was built to address all of the mentioned issues. The major difference between the two designs is the use of four completely independent

³ Portions of this chapter (sections 4.2.2 and 4.2.3) were adapted from: C. Liu, Y.-L. Liu, E.P. Perillo, N. Jiang, A.K. Dunn, H.-C. Yeh, "Improving z-tracking accuracy in the two-photon single-particle tracking microscope," *Applied Physics Letters*, 107 (2015). E.P.P conceived the project, designed and built the microscope. C.L. implemented the algorithm and wrote the manuscript.

beam paths that are then recombined onto a single axis. Independent access to each beam allows for complete control (x-tip, y-tilt, and z-collimation) of each beam in the focal plane of the microscope. The independent design also allows for balancing the power of each beam with variable neutral density filters, something that could not be done with the previous iteration.

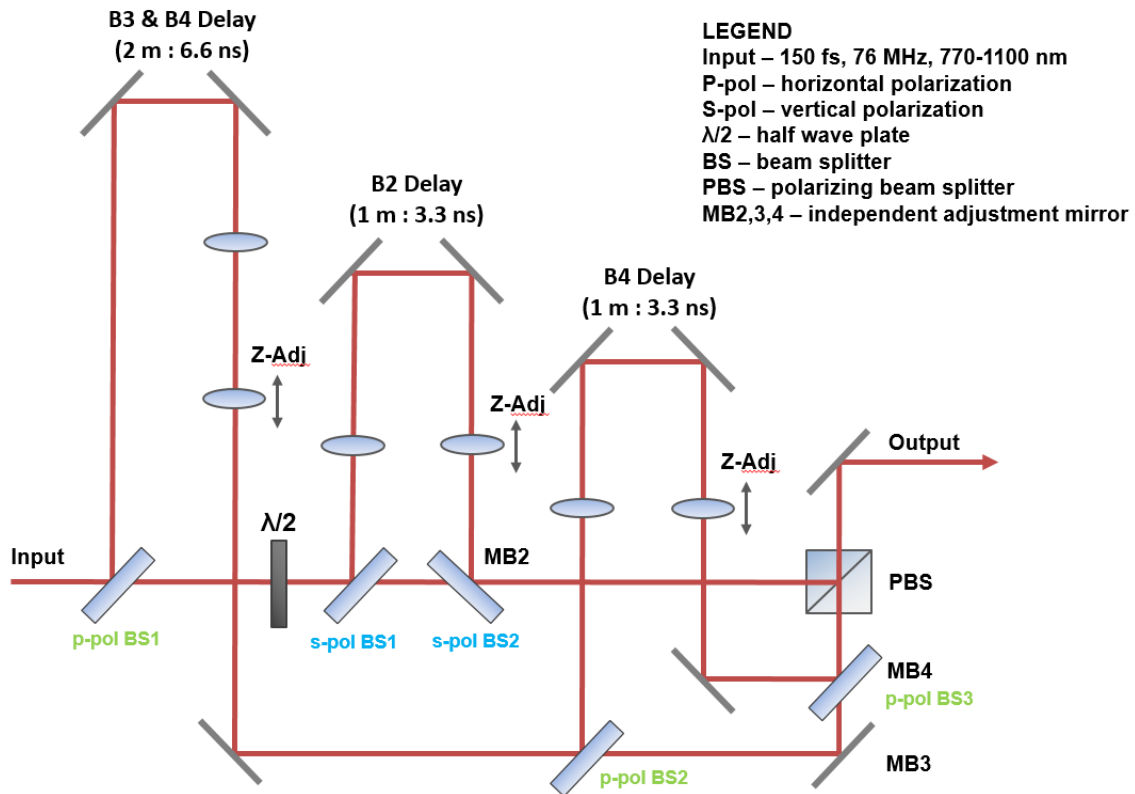


Figure 4.1 | Independent Control Beam Multiplexer Schematic

A major limitation with wavelength operating range in the previous design was that the beam splitter optics employed did not offer perfect 50:50 split ratio over the entire range. The inability to independently adjust each beam power level added to problem. The result was that power could not be balanced when working with a wavelength outside of the 780-

820 nm range, with differences in beam powers sometimes exceeding 20%. TSUNAMI generally requires average power of each beam to be within 10% to operate robustly, although the proportional controller can account for some misalignment and difference in beam power. The ability to independently adjust each beam makes daily alignment easier, as only one adjustment mirror is tied to one beam, so there is no crosstalk between beams when aligning. The addition of another optical delay line, for a total of three, means that collimation of each beam can independently adjusted through telescope assemblies (Z-adj, in **Figure 4.1**), as opposed to convoluted adjustments with only two-delay lines in the previous design.

Another improvement to the multiplexer design is the use of low group velocity dispersion (GVD) beam splitters (BS1,2,3 in **Figure 4.1**) as opposed to bulk glass cube beam splitters in the old design. The low-GVD beam splitters (FS01-BSTiS-5050P-25.4, Semrock) excel in two areas. First, they minimize the impact of the pulse width broadening at the sample. Second, the beam splitters have a significantly larger operating range (700-1100 nm) and a near perfect 50:50 split ratio over their entire range. This, in theory, expands the usable wavelength for TSUNAMI from 780-820 nm to 700-1100 nm.

4.2 ENHANCED LOCALIZATION WITH MAXIMUM LIKELIHOOD ALGORITHM

The following section details an improved algorithm for localization of single emitters with the TSUNAMI microscope. The algorithm notably improves axial (z dimension) localization by a factor of 3 fold. First, axial localization with the arithmetic method is discussed, followed by an introduction to the improved maximum likelihood method (MLE), and finally a detailed comparison is outlined.

4.2.1 Axial localization with arithmetic method

The first iteration of TSUNAMI performed localization using an arithmetic method. The arithmetic methods calculates normalized count rate differences between a pair of beams (xy) or all four beams (z) to obtain an optical error signal,

$$E_x = \frac{G_2 - G_1}{G_2 + G_1} \quad (1)$$

$$E_y = \frac{G_4 - G_3}{G_4 + G_3} \quad (2)$$

$$E_z = \frac{(G_4 + G_3) - (G_2 + G_1)}{(G_1 + G_2 + G_3 + G_4)} \quad (3)$$

Where G_1 , G_2 , G_3 , and G_4 are the summed beam counts within the four windows of the detector (**Figure 2.2b**).

For a particle moving perfectly along any single axis the error profiles will appear to be like **Figure 4.2**. These error profiles in xyz, allows for accurate (<30 nm) localization over a wide range of ~500 nm in xy, and 1 μm in z. Although, they are idealized. In reality, a particle does not move perfectly along a single axis while staying centered on the orthogonal axes. A particle in free diffusion, will move randomly along all three axes in space according to Brownian diffusion. This results in inaccuracies with the localization algorithm. Specifically, if the particle is not centered in the xy plane, the axial (z) localization can suffer dramatically, from 30 nm to >100 nm.

The reason for the loss in z localization is because the error signal is not uniform within a given xy plane (**Figure 4.3**), and can even switch sign, resulting in a positive feedback loop and rapid loss of tracking.

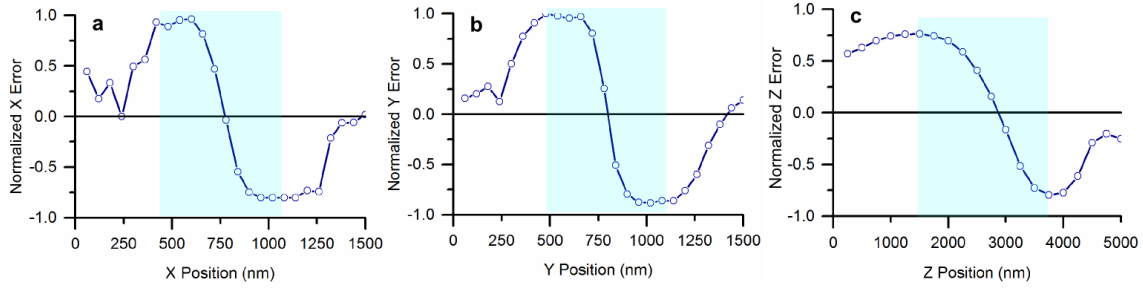


Figure 4.2 | TSUNAMI Error Profiles

(a) X error signal, (b) y error signal, (c) z error signal. All profiles are perfectly positioned along the PSF centroid.

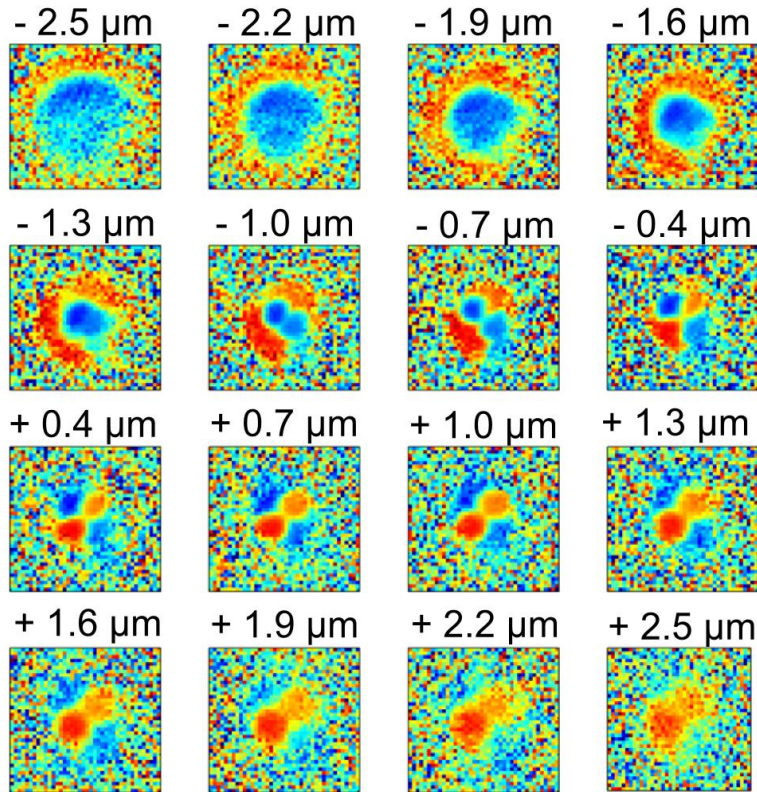


Figure 4.3 | Axial Error Signal as a Function of XY Position

Axial error signal calculated at 16 plane spanning 5 μm in z. The XY image size is 4 μm . Data is obtained from fluorescent scanning of a single 40 nm bead. The calculation from Equation (3) is applied to every voxel in the 3D stack. The beam spacing is approximately 500 nm in XY and 1 μm in Z.

The axial localization signal can be seen to switch sign depending on which beam pair the particle is over (**Figure 4.3**). This effect can be attributed to the spatially offset beam pairs that are used for z-localization. If the particle is moving rapidly and moves out of the small region where all four beams overlap in the XY plane, then an inaccurate error signal will be calculated. For example, if the particle is perfectly centered in xy in the PSF, and moves along the z direction, the error profile will take the form of **Figure 4.2c**. However, if the particle moves towards a beam in the lower pair (B1, **Figure 4.4**), or a beam in the upper pair (B3, **Figure 4.4**), the error signal profile will be significantly different. In most cases, the error signal is either drastically over reported, or drastically under reported, depending on which beam it is closest to.

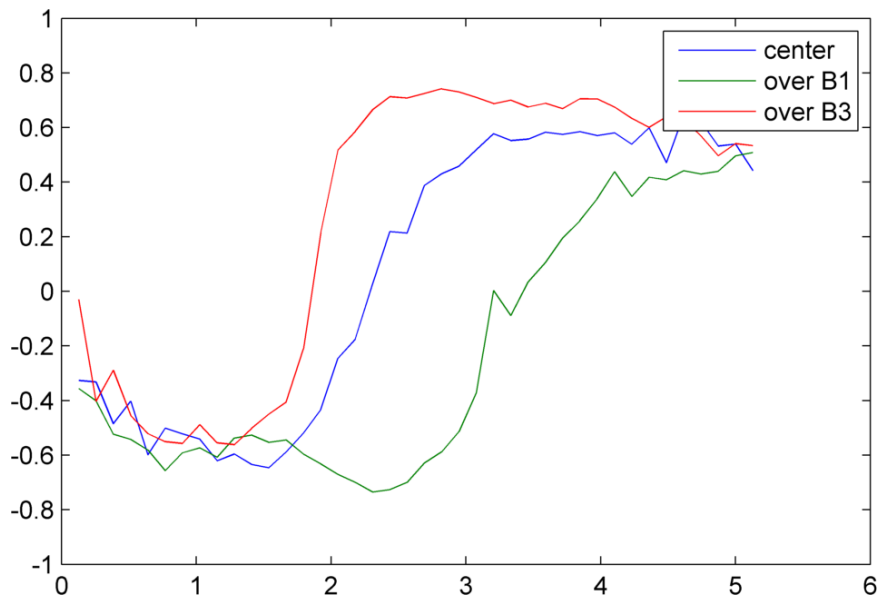


Figure 4.4 | Axial Error Profile Inconsistency

The loss in axial localization can be mitigated by moving the xy offset of the tetrahedral PSF closer together, resulting in a more consistent axial localization signal as a

function of xy space. However, moving the PSF to a smaller xy beam offset comes at the expense of worse xy localization and a smaller localization range.

Ideally, to fully overcome this limitation and obtain a flat z error across the entire XY PSF, one would need 6 independent beams, two beams for each dimension. Unfortunately, 6 beams would dramatically increase the complexity and cost of the beam multiplexer, and limit the number of usable fluorophores by requiring even narrower temporal windows (2.1 ns vs. 3.3 ns for a 13 ns period laser).

Another approach to improve the axial localization while still retaining good localization in the xy direction is to adopt a different algorithm. Rather than using a simple normalized difference (Arithmetic method), one can employ a more sophisticated algorithm which uses a maximum likelihood approach and a look up table to account for the co-dependent localization signal in all three-dimensions. The following section will discuss the implementation and performance of such an algorithm.

4.2.2 Implementation of MLE

An algorithm that can significantly increase the z-tracking accuracy is maximum likelihood estimation (MLE)³. Using MLE for particle position estimation, Sahl and coworkers have previously achieved 2D single-particle tracking with xy localization error as small as 10–20 nm.⁴ MLE finds the most likely position of the emitter by comparing the recorded photon counts in the four time gates $\vec{I} = [I_1, I_2, I_3, I_4]$, with a 3D reference map $\vec{R}(x, y, z) = [R_1(x, y, z), R_2(x, y, z), R_3(x, y, z), R_4(x, y, z),]$, where $R_i(x, y, z)$, denotes the photon counts in the i-th time gate when the reference emitter is located at position (x, y, z). Such a 3D reference map can either be established by optical modeling, or established experimentally by raster scanning the excitation tetrahedron with an immobilized fluorescent nanoparticle (i.e., the reference emitter) while recording the four signal

intensities as a function of the particle's position. $\vec{R}(x, y, z)$ is further normalized such that $\sum_{i=1}^4 R_i(x, y, z) = 1$. For a given emitter position (x, y, z) , the probability of detecting I_i photons in the i -th time gate follows Poisson distribution (where R_i is the expected value and the variance).

$$p_1(I_i; R_i | x, y, z) = \frac{R_i(x, y, z)^{I_i}}{I_i!} \exp(-R_i(x, y, z)) \quad (4)$$

The likelihood of detecting \vec{I} photons at a position (x, y, z) with $\vec{R}(x, y, z)$ expected photons on average is given by the product of the above probabilities.

$$L(\vec{I}; \vec{R} | x, y, z) = \prod_{i=1}^4 p_i(I_i; R_i | x, y, z) \quad (5)$$

The most likely position of the emitter is thus the location where this likelihood L is maximized, or equivalently where the log-likelihood is maximized⁴.

$$(\hat{x}, \hat{y}, \hat{z}) = \max_{(x, y, z)} [\sum_{i=1}^4 I_i \ln(R_i(x, y, z))] \quad (6)$$

In each time step, we search for a position (x, y, z) that maximizes the log-likelihood and uses that to represent the emitter's position. By virtue of MLE, the z-tracking accuracy is enhanced by 1.7 fold (**Table 3.1**). While the z-tracking error is still larger than the xy-tracking error, their relative difference is reduced from $129 \pm 23\%$ to $33 \pm 4\%$. Additionally, the relative error for the calculated diffusion coefficient is decreased from $14 \pm 1\%$ to less than 2%. The improvement of the z-tracking accuracy can be clearly seen in the z-tracking error histograms (**Figure 4.5b and 4.5d**). Both histograms could be well described by a Gaussian distribution, with mean approximately equal to zero. Comparing the two tracking schemes, MLE clearly gives a narrower z-tracking error distribution ($\sigma = 50.2$ nm vs. 93.9 nm) and a better diffusion coefficient estimate ($\hat{D} = 0.50$ $\mu\text{m}^2/\text{s}$ vs. 0.47 $\mu\text{m}^2/\text{s}$).

	Method	XY (nm)	Z (nm)	\hat{D} ($\mu\text{m}^2/\text{s}$)
$D = 0.5 \mu\text{m}^2/\text{s}$	ESA	42.9	87.6	0.42 ± 0.06
	MLE	38.7	50.7	0.51 ± 0.06
$D = 1.0 \mu\text{m}^2/\text{s}$	ESA	53.4	123.8	1.14 ± 0.13
	MLE	55.6	72.8	1.00 ± 0.11
$D = 1.5 \mu\text{m}^2/\text{s}$	ESA	65.7	164.7	1.76 ± 0.20
	MLE	69.0	95.5	1.53 ± 0.18

Table 3.1 | Comparison of tracking errors from different estimation algorithms
 \hat{D} is the estimation of true diffusion coefficient D . ESA: error signal analysis, and MLE: maximum likelihood estimator.

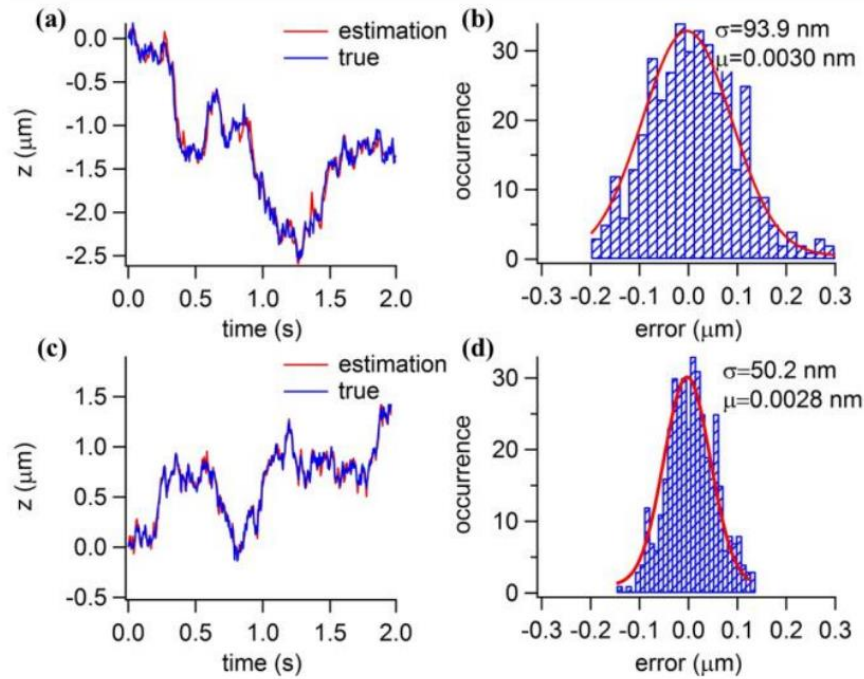


Figure 4.5 | Representative z trajectories and tracking error distribution.

(a) and (b): ESA tracking. (c) and (d): MLE tracking. The red curves represent the estimated z trajectories while the blue curves represent the true z trajectories of the diffusive particle. In this simulation, the diffusive particle ($D = 0.5 \mu\text{m}^2/\text{s}$) is tracked for 2 seconds, and 250 of 2-second-long trajectories are used to build the histograms. The standard deviations of the fitted Gaussian curves are 93.9 nm (ESA) and 50.2 nm (MLE), respectively. The diffusion coefficients calculated from the mean-squared displacement analysis are $0.47 \mu\text{m}^2/\text{s}$ and $0.50 \mu\text{m}^2/\text{s}$, respectively.

4.2.3 Comparison between localization methods

Both enhanced z-tracking accuracy and less temporally correlated z-tracking errors can contribute to the improved molecular kinetics estimation shown in **Figure 4.6**. To understand their relative importance, we have tested two scenarios in our simulations : (a) the z-tracking errors are kept small, but they are temporally correlated; (b) the z-tracking errors are large, but they are temporally uncorrelated. By comparing the relative errors given by the MLE based tracking and the scenario (a), we have found that more precise kinetics estimation in MLE-based tracking cannot be solely explained by better z-tracking accuracy. On the other hand, by comparing the relative errors given by the ESA-based tracking and the scenario (b), we have found that the quality of kinetics characterization can be dramatically improved solely by making the tracking error less correlated over time, even when the tracking error amplitude remains the same. Therefore, decorrelation of z-tracking error plays a critical role in reliable recovery of molecular kinetics. In conclusion, we have developed a maximum likelihood estimator (MLE) that can improve the z-tracking accuracy of TSUNAMI microscope by 1.7 fold, without sacrificing the xy-tracking accuracy. MLE outperformed the traditional ESA tracking scheme mainly because ESA has a fundamental flaw in its z-position estimate—the cross-talk between the lateral and axial direction is not accounted for. MLE, on the other hand, uses all the information available for position estimate (including any possible cross-talk), therefore resulting in a much smaller z-tracking error. We believe that the less temporally correlated z-tracking error found in MLE tracking is also a result of its better position estimate in each time step. With less temporally correlated tracking error, precise hybridization-melting kinetics of a DNA model system have been recovered from thousands of short trajectories in silico.

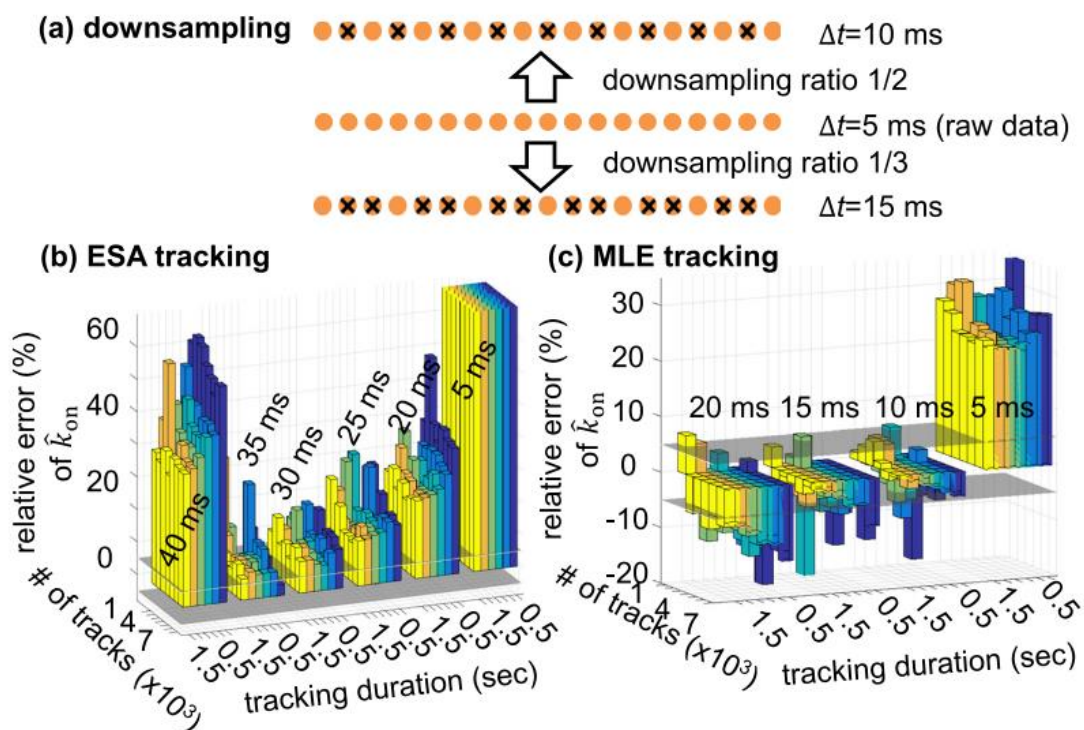


Figure 4.6 | Comparison between ESA and MLE Algorithms

(a) Downsampling of the raw trajectory data. Raw trajectory data have a temporal step size $\Delta t = 5$ ms. Downsampling ratios of 1/2 and 1/3 result in $\Delta t = 10$ ms and $\Delta t = 15$ ms, respectively. Downsampled trajectories are then analyzed by the 3D variational Bayes method (vbSPT) in order to discern the binding-unbinding kinetics (k^{on} and k^{off}) of the tracked particle. (b) Relative error of k^{on} derived from ESA-based trajectories. (c) Relative error of k^{on} derived from MLE-based trajectories. In this simulation, the number of tracks and track duration are varied to assess the convergence of vbSPT. Each bar represents one vbSPT analysis of 1,000-7,000 trajectories, with bar height showing the relative error of k^{on} and bar color encoding tracking duration (0.5 s—purple, 0.7 s—dark blue, 0.9 s—light blue, 1.1 s—green, 1.3—orange, and 1.5 s—yellow). The horizontal grey planes are where the relative error equals 6.5%. The 6 bar groups in (b) correspond to k^{on} obtained from 6 different downsampling ratios, whose Δt are integer multiples of 5 ms. Similarly, the 4 bar groups in (c) correspond to k^{on} obtained from 4 different downsampling ratios. Figure from Cong Liu.

Our preliminary implementation of the MLE algorithm on a quad-core Windows PC suggests that MLE can be run in quasi real time (< 1 ms), and potentially can be further accelerated by dedicated field programmable gate array (FPGA). Our approach can be

readily applied to other feedback-driven SPT techniques which suffer from the large z-tracking error and the temporally correlated-tracking-error issues.⁵ This work demonstrates that temporally uncorrelated tracking error is as important as small tracking error, and binding-unbinding kinetics cannot be correctly characterized without first examining the temporal properties of tracking/localization errors.

4.3 SIMULTANEOUS TRACKING AND IMAGING WITH STED MICROSCOPY

TSUNAMI is inherently compatible with traditional two-photon (2P) laser scanning microscopy, because it is built upon a basic 2P microscope. In the first demonstration of TSUNAMI, 2P scanning is performed just before SPT to map out the surrounding cellular environment and provide biological context for the measured trajectory¹. Other such combined tracking and imaging approaches have been utilized in the past to provide biological context. For example, Welsher combined a 2P scanning microscope and confocal 3D SPT microscope together to map interactions with particles and membrane structure⁶. The Werner group has employed the use of EMCCD detection overlaid with 3D confocal SPT microscope for simultaneous detection of the surrounding environment⁷. The hybrid tracking and imaging approach is a powerful tool for understanding how trajectories fit into the biological context. However, all of the previous methods, rely on diffraction limited images for which the place the trajectory. Often times a 3D SPT trajectory can have resolution of better than 30 nm in all dimensions, whereas diffraction limited 2P images are typically ~300 nm resolution. This order of magnitude resolution discrepancy can pose a problem when co-registering trajectories to densely packed sub-diffraction structures, such as the actin or tubulin within a live cell⁸.

Here we propose to combine superresolution microscopy with high resolution 3D single particle tracking as a method to study fast transport events within the live cell. The

most compatible superresolution technique to combine with TSUNAMI is Stimulated Emission Depletion (STED) Microscopy.⁹ As STED can be made compatible with two-photon excitation¹⁰. Recently, it was shown that 2P STED microscopy can be performed with a single laser source¹¹. We demonstrate that this approach can be easily incorporated into the existing TSUNAMI microscope design and utilized for STED superresolution mapping of the cellular environment followed by TSUNAMI particle tracking in a serial acquisition scheme.

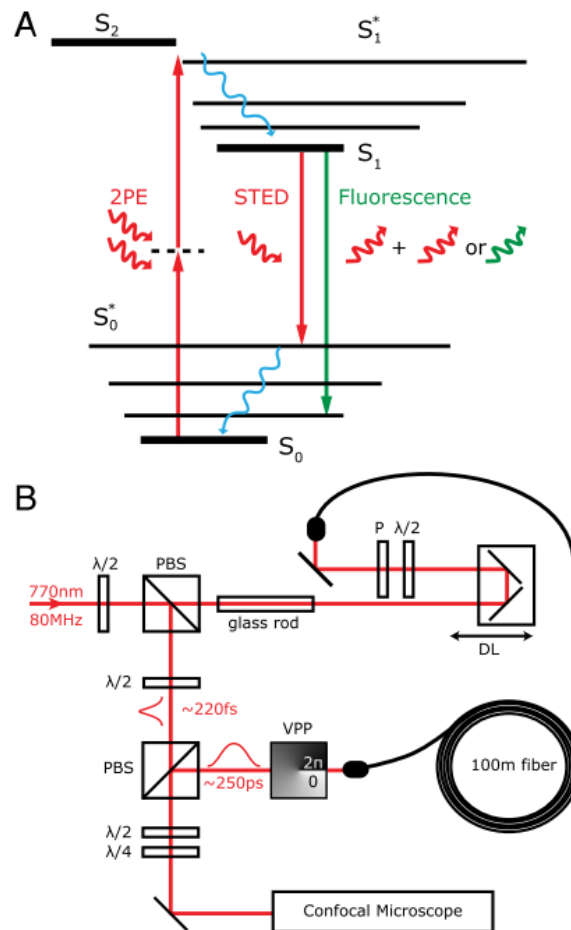


Figure 4.7 | Single Wavelength 2P STED Schematic

(Figure adapted from Bianchini et. al. PNAS)¹¹ (A) Simplified Jablonski diagram showing the states involved in 2PE-STED single wavelength. (B) Scheme of the setup. P, polarizer; DL, delay line; VPP, vortex phase plate.

The single wavelength STED setup (**Figure 4.7**) consists of a fairly simple design, including a stretcher path with glass rod and 100 m of fiber and a vortex phase plate to generate a donut beam. The excitation path is the same as any traditional 2P microscope. Using a single laser allows for easy integration into the existing TSUNAMI microscope since the same laser (Mira 900, Coherent) can be shared among all excitation paths, even further reducing cost. The system is inherently synchronized, for any future applications requiring multiplexed TSUNAMI and STED excitation for parallel image acquisition.

Preliminary results show that the 2P STED system can achieve superresolution in a sample of fixed dark red fluorescent beads (**Figure 4.8**) and that the donut beam generation is possible with a good central null.

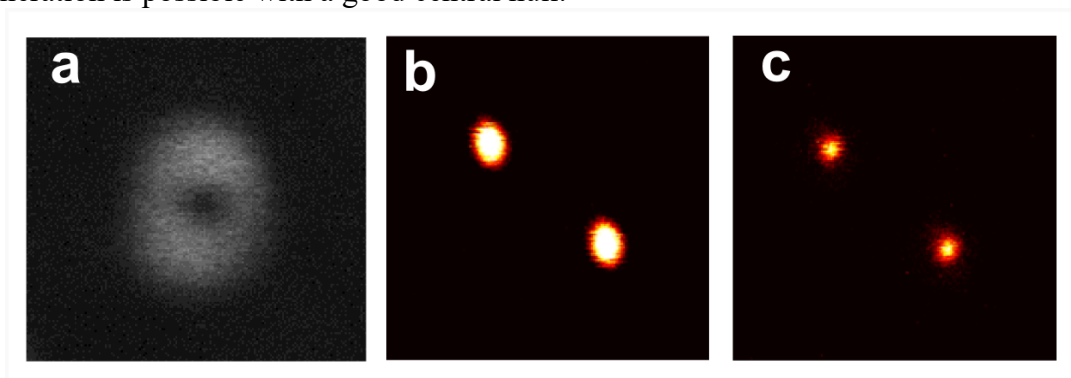


Figure 4.8 | 2P STED Preliminary Results

(a) Image of the donut shaped depletion PSF used for STED, generated by scanning of a 200 nm fluorescent bead. (Image size 3 μm) (b) 2P Image of 200 nm fixed fluorescent beads. (c) 2P STED images of the same 200 nm fluorescent beads. (Image size is 5 μm)

The resolution enhancement from 2P scanning to STED with fluorescent beads was found to be ~ 300 nm to ~ 150 nm. Due to the size of the fluorescent beads, the lowest limit of resolution was not able to be determined. However, the previous demonstrations have shown that 80 nm resolution is possible with 2P STED.^{10,11}

When moving to a biological sample with a standard dye used for STED (atto633) we find that our implementation of STED suffers from significant background noise

introduced from the depletion beam (**Figure 4.9**). We have stained the actin structure with atto633 and performed 2P scanning with just the excitation beam (2P, in **Figure 4.9**), just the depletion beam (Depletion in **Figure 4.9**), and both beams synchronized (STED in **Figure 4.9**). We find that the STED image offers slightly better resolution than the 2P image, however at the expense of a lower signal to background ratio. The result is a less than optimal image. By observing the contribution from the depletion beam alone, we can see that the system suffers from very high background introduced by the depletion beam.

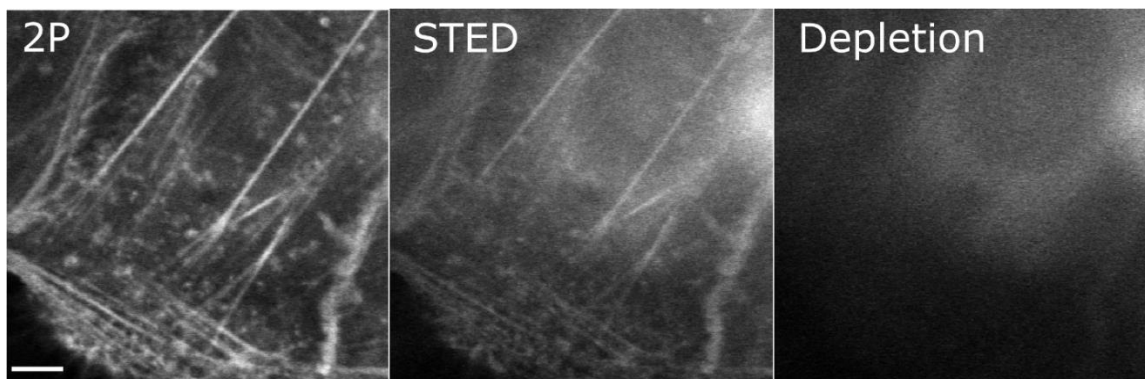


Figure 4.9 | 2P STED in a Fixed Cell

Despite the depletion beam being stretched to 200 ps, there is still significant excitation. It was determined that the excitation is one-photon fluorescence, not two-photon. This type of one-photon excitation is known as anti-stokes excitation, and can occur depending on the quantum selection rules of the dye in question, if the excitation spectrum extends beyond the peak of the emission spectrum. A discussion regarding this phenomenon has been mentioned in literature¹². The issue with our embodiment of 2P STED is the non-descanned detection scheme which relays all of the light from the objective back aperture onto the detector. Whereas, other STED microscopes, even 2P STED, use a confocal pinhole detector which removes out of focus light. The excitation

from the donut depletion beam is effectively removed through the use of a confocal pinhole. Future steps will be towards utilizing a confocal detection scheme with 2P STED and improving labelling strategies to perform live cell STED with combined TSUNAMI.

4.4 TWO-COLOR DUAL PARTICLE TRACKING MICROSCOPY

The final modification to the TSUNAMI microscope that will be discussed is an expansion to the number of available detector channels which allows for localizing multiple particles. The TSUNAMI system is capable of adding an arbitrary number of additional detectors limited only by the spectral overlap of common fluorophores (typically maximum of 4). Unlike confocal 3D SPT, the addition of extra detectors for TUSNAMI is a nearly trivial alignment matter and offers robust perfectly co-localized detection. Because TSUNAMI is built upon a two-photon microscope it shares the common architecture of non-descanned detection. In non-descanned detection, the light exiting the objective back aperture is collected and condensed onto a large area detector, image formation occurs through sequentially scanning the laser over the sample. Whereas, for confocal detection SPT the addition of a second image channel requires 4 or 5 extra detectors, all which must be perfectly co-aligned to the original detector channels. The alignment challenge present with confocal based SPT microscopes has, to date, precluded the use of multiple color detection and co-localization. However, 2D camera tracking techniques have utilized two-color detection, by merely doubling the number of cameras and using proper spectral filtering¹³. Although, for multicolor detection with cameras, the approach is expensive, and limited in temporal resolution to ~500 ms. Here, we detail the method for multiple particle localization using TSUNAMI and highlight one application for detecting DNA in free diffusion.

4.4.1 Multiple Particle Localization

Multiple particle localization is performed through two modifications to the standard TSUNAMI microscope (1) Hardware (2) Algorithm. First, the hardware required is an additional PMT (PMT1 and PMT2, **Figure 2.2**), and a TCSPC routing module. The PMT collects the light emitted from the second fluorophore in the separate spectral channel. The routing module is required (HRT-41, Becker & Hickl) for routing the second detectors channel to the same TCSPC board (SPC-150, Becker & Hickl). Since all detectors feed into the same SPC module, as the number of detector channels increases, the saturation count rate decreases accordingly. For two channels, the saturation count rate in each is approximately 2 MHz which is still twice as high as the highest typical count rate for live cell tracking of fluorescent beads.

The second, modification needed to perform multiple particle localization is an algorithm to register the raw photon count data from the second channel within the same 3D space as the primary particle being tracked. Two-color TSUNAMI works by co-registering the secondary particle relative to the primary target being tracked. If the secondary particle moves out of the PSF which is centered on the primary target then the particle will be lost.

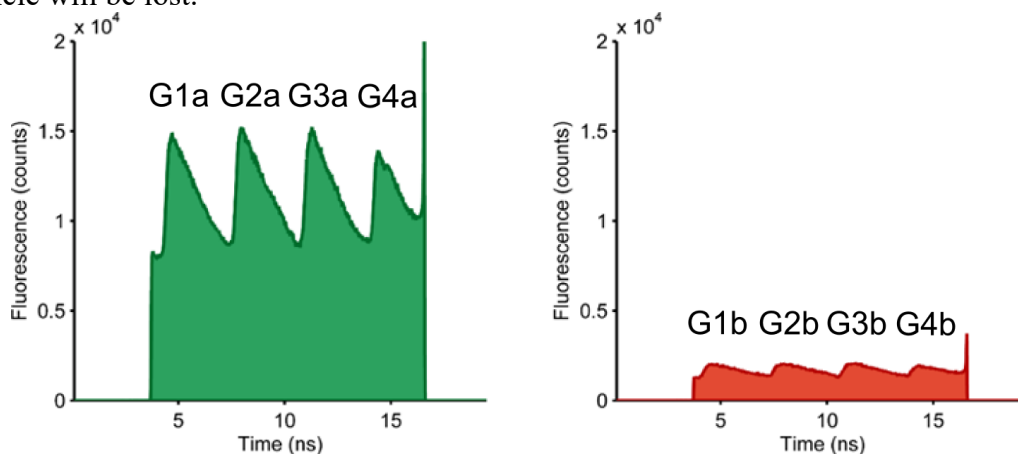


Figure 4.10 | Raw Photon Count Data for Two-color TSUNAMI

The raw signal can be seen (**Figure 4.10**) summed up in each channel (green and red) for a 2 second trajectory. The localization for the secondary (red) channel can be performed using the same arithmetic method as outlined in Section 4.2. The key difference being, that this localization takes place in post processing and does not affect the position of the xy galvo mirror actuators. The post-processed error signals are calculated from equations (1-3), which are then proportionally modified to account for stage scaling factors. The resulting localization is a position relative to where the PSF was at the current time of localization (i.e. the current position of the primary target. To move the relative localizations into the global frame of reference, all that is required is to shift the position by the amount of the current position of the primary target. Using this technique two particles can be tracked simultaneously with no loss in temporal resolution.

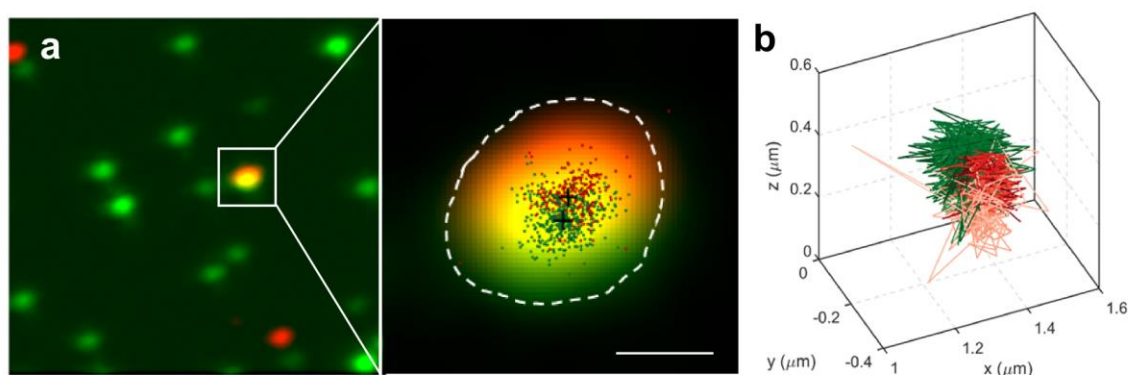


Figure 4.11 | Two-Color Localization

(a) 2P Fluorescence image of red and green 40 nm fluorescent beads fixed to a coverslip. Zoom: a magnified view of a single red and green bead pair separated by a distance of ~40 nm, scale bar is 200 nm. (b) A reconstructed 3D trajectory of both beads measured for 2 seconds.

Simultaneous two-color tracking is demonstrated with 40 nm red and green beads fixed to a coverslip. It can be seen that the secondary target co-localization (**Figure 4.11b**) agrees well with the 2P scanning images (**Figure 4.11a**). The Gaussian fit centroid (+ in

Figure 4.11a) of each image channel is overlaid with the trajectory points projected onto 2D (green and red dots in **Figure 4.11a**).

The signal-to-noise in each 2P image is very high due to long exposure and lots of averaging (5 frames), so we use this as a reference standard for which to compare our two-color trajectories. The typical standard deviation for the centroid fit in the 2P images was less than 1 nm, so it can be used as a highly accurate reference compared to the SPT trajectories which have an error in the 20-50 nm range.

By repeatedly imaging and tracking many bead pairs in the sample of 40 nm green and red beads, along with other mixtures (40-40 nm with 150 nt DNA, 200 and 200 nm) we can build a plot that shows the RMS accuracy of the two-color co-localization technique relative to the Gaussian based image analysis.

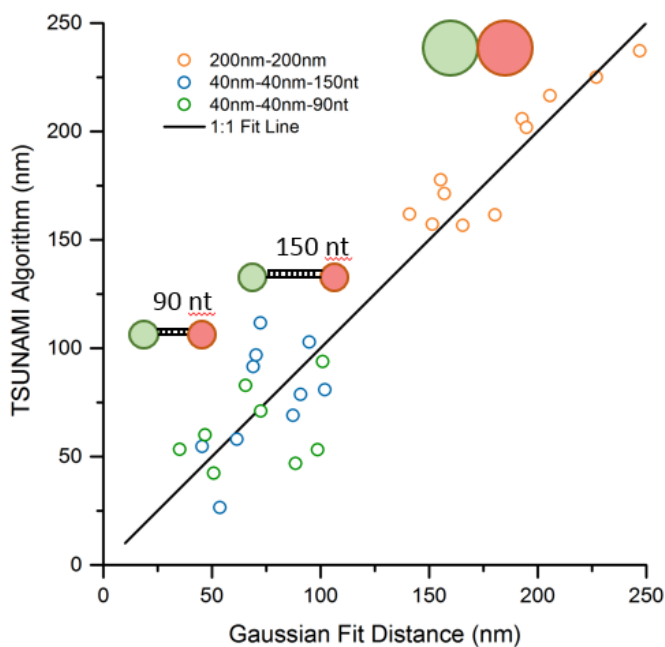


Figure 4.12 | Co-localization of different separation distance bead pairs

The results of our experimental determination of the technique's accuracy can be seen in **Figure 4.12**. The accuracy was found to be 40 nm, with a precision on the order of

20 nm. In this experiment we use a DNA separating strand to ensure that there is 1:1 dimerization of the beads, along with controlled separation distance. The technique follows the guidelines of previous DNA linker formation protocol¹⁴.

4.4.2 Dual particle tracking of DNA in solution

The dual particle tracking technique offers a wealth of information about the particle constructs. In the case of a target labelled with two separate indicators, such as a DNA strand (**Figure 4.13**), several key parameters can be obtained through processing of the trajectory: XYZ Position, $\theta\phi$ Rotation Angle, D Binding distance, and B1, B2 Photon Count Rate are all available metrics which can be obtained by processing the raw data from both channels.

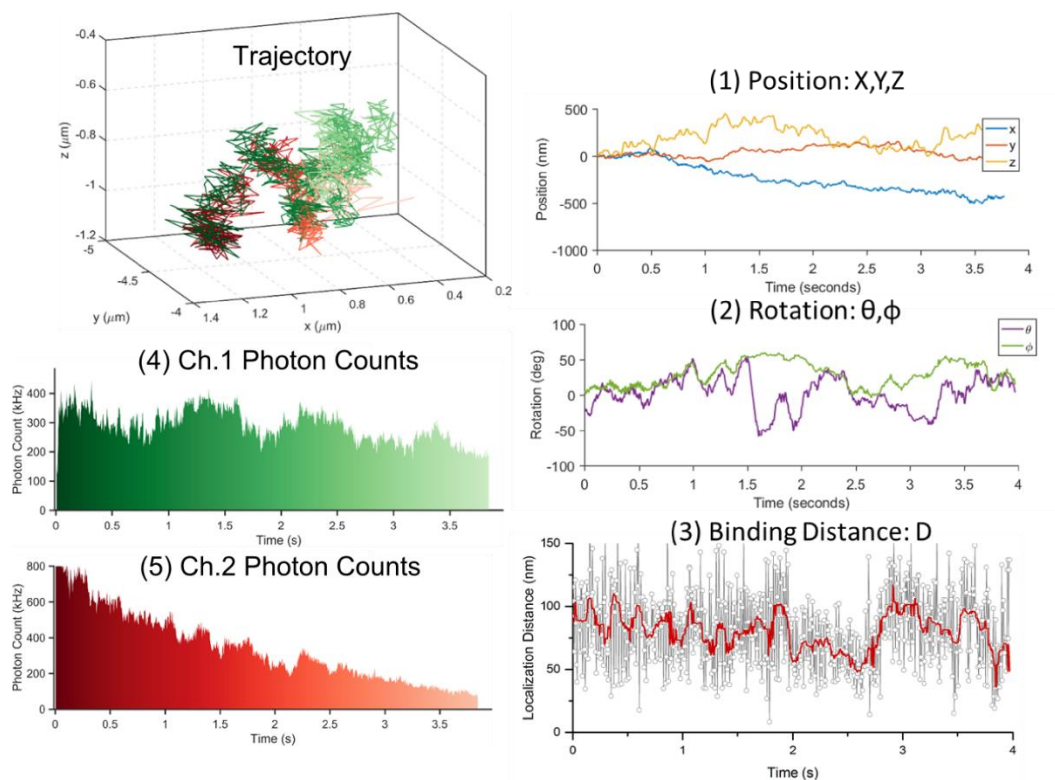


Figure 4.13 | Dual Particle Tracking of DNA Constructs in Free Diffusion

We concentrate our analysis on the binding distance parameter, D (**Figure 4.13**) in a novel application to study the dynamics of DNA strands in free diffusion. By calculating the geometric distance between the primary (green channel) and secondary (red channel) target we can estimate the approximate distance between the two labelled ends of the DNA strand.

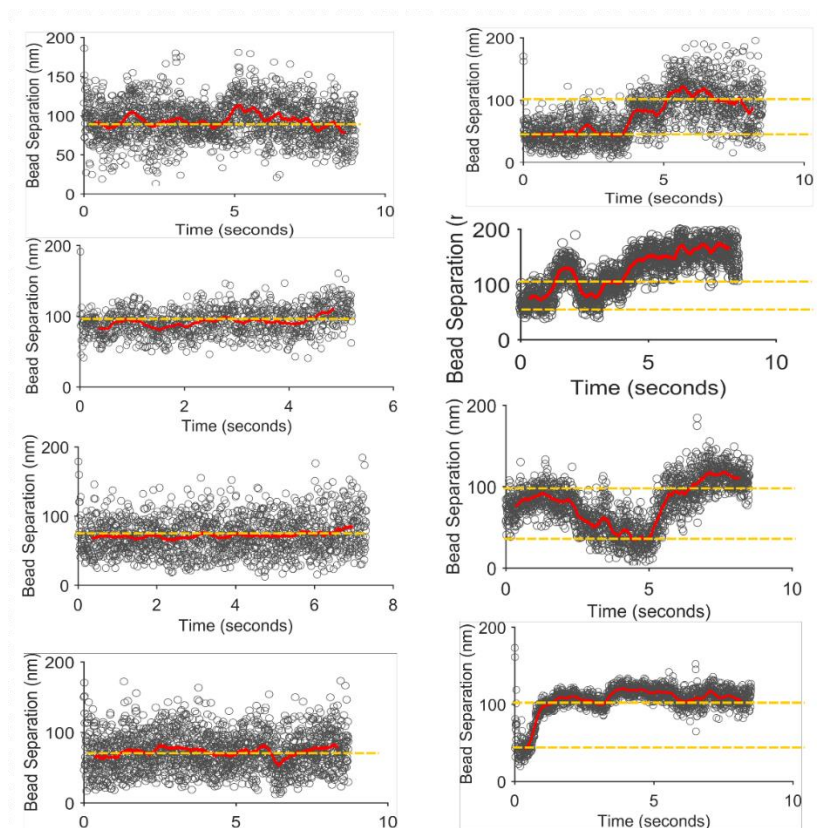


Figure 4.14 | DNA Distance Fluctuations in Free Diffusion

First Column: Fixed DNA bead constructs (150 nt, 40nm green, 40nm red), Second Column: Free diffusion DNA bead constructs in 60% dextran solution.

Figure 4.14 Shows four representative trajectories plotting binding distance versus time for two experimental conditions with a bead construct and 150 nucleotide linker DNA strand. In the fixed case we see a relatively static binding distance at approximately the expected magnitude ~ 100 nm. Whereas, for the free diffusion case, we observe a switching behavior between two states, 100 nm *the fully extended length) and 40 nm (the minimum

distance between the beads). This potentially indicates that the DNA is flexing or bending during free diffusion which allows for the beads to occupy a range of separation distances during the trajectory. Future work will be towards determining the exact mechanism of this behavior, and measuring a sufficient number of trajectories to statistically support the hypothesis.

The two-color dual-particle localization technique outlined here is a simple modification to TSUNAMI which provides a number of important metrics (rotation, separation distance) that are unable to be obtained through standard SPT alone. Existing multicolor techniques based on plasmonic resonance only provide localization within a small <70 nm range, and are limited to slow camera detection¹⁴. We expand the toolset for multiple particle tracking techniques by outlining a simple addition to the TSUNAMI microscope which allows for co-localization with distances up to 300 nm and accuracy as good as 40 nm, with a precision of 20 nm. The dual-particle localization technique will be a powerful analysis tool for measuring biological interactions in the cell.

4.5 DISCUSSION

Here we demonstrate that TSUNAMI is a flexible technique with a wide array of capabilities and areas for specialization. First, we discussed two modifications, one hardware modification to the novel beam multiplexer design which enables easier alignment through independent beam control. The second modification is an improvement to the localization algorithm which improves axial (z) localization by a factor of two times. Both modifications do not necessarily have drawbacks when compared with the previous embodiment, and should be regarded as purely upgrades or refinements to the instrumentation.

The second half of this section covers hardware and software modifications that aim to solve more specialized problems in biology. The combined superresolution STED microscopy with TSUNAMI approach enhances the ability to localize single particles to their surrounding environment. However it comes at the expense of slower image acquisition, and higher photobleaching rates, as is typical for STED microscopy¹². Nevertheless, the approach holds promise for applications requiring co-registration of trajectories to sub-diffraction structures such as the actin cytoskeleton of a cell⁸. The final modification to the TSUNAMI method is two-color (dual-particle) tracking. We show that this method of co-localizing secondary targets relative to the primary target allows for potentially interesting applications for measuring rotational orientation of constructs in the cell¹⁵. The method could also be used to measure distance between two labelled targets¹⁴ for detection of binding events, or to measure binding dynamics in real-time (<5 ms).

Clearly, the TSUNAMI technique is adaptable to numerous applications in single particle analysis and live cell biology, from measuring trajectories across an entire 10 μm span of a cell through 100 μm of scattering material, all the way down to detection of the binding distance between two targets only ~ 40 nm apart, this technique spans many orders of magnitude in length scale. We believe these outlined methods will provide a unique toolset for future applications in cell biology research.

4.6 REFERENCES

1. Perillo, E. P. *et al.* Deep and high-resolution three-dimensional tracking of single particles using nonlinear and multiplexed illumination. *Nat. Commun.* **6**, 7874 (2015).
2. Ji, N., Magee, J. & Betzig, E. High-speed, low-photodamage nonlinear imaging using passive pulse splitters. *Nat. Methods* 1–6 (2008).
3. Liu, C. *et al.* Improving z-tracking accuracy in the two-photon single-particle tracking microscope. *Appl. Phys. Lett.* **107**, 153701 (2015).
4. Sahl, S. J., Leutenegger, M., Hilbert, M., Hell, S. W. & Eggeling, C. Fast molecular tracking maps nanoscale dynamics of plasma membrane lipids. *Proc. Natl. Acad. Sci.* **107**, 6829–6834 (2010).

5. Lessard, G. a., Goodwin, P. M. & Werner, J. H. Three-dimensional tracking of individual quantum dots. *Appl. Phys. Lett.* **91**, 224106 (2007).
6. Welsher, K. & Yang, H. Multi-resolution 3D visualization of the early stages of cellular uptake of peptide-coated nanoparticles. *Nat. Nanotechnol.* **9**, 198–203 (2014).
7. Wells, N. P. *et al.* Time-resolved three-dimensional molecular tracking in live cells. *Nano Lett.* **10**, 4732–7 (2010).
8. Lagerholm, C., Andreade, D., Clausen, M. & Eggeling, C. Convergence of lateral dynamic measurements in the plasma membrane of live cells from single particle tracking and STED-FCS. *J. Phys. D Appl. Phys.* **50**, (2017).
9. Moneron, G. & Hell, S. W. Two-photon excitation STED microscopy. *Opt. Express* **17**, 14567–73 (2009).
10. Takasaki, K. T., Ding, J. B. & Sabatini, B. L. Live-cell superresolution imaging by pulsed STED two-photon excitation microscopy. *Biophys. J.* **104**, 770–7 (2013).
11. Bianchini, P., Harke, B., Galiani, S., Vicidomini, G. & Diaspro, A. Single-wavelength two-photon excitation-stimulated emission depletion (SW2PE-STED) superresolution imaging. *Proc. Natl. Acad. Sci. U. S. A.* **109**, 6390–3 (2012).
12. Hernández, I. C. *et al.* Two-Photon Excitation STED Microscopy with Time-Gated Detection. *Sci. Rep.* 1–9 (2016). doi:10.1038/srep19419
13. Albrecht, D., Winterflood, C. & Ewers, H. Dual color single particle tracking via nanobodies. *Methods Appl. Fluoresc.* (2015). doi:10.1088/2050-6120/3/2/024001
14. Lee, K., Cui, Y., Lee, L. P. & Irudayaraj, J. Quantitative imaging of single mRNA splice variants in living cells. *Nat. Nanotechnol.* **9**, 474–480 (2014).
15. Anthony, S. M. & Yu, Y. Tracking single particle rotation : probing dynamics in four dimensions. *Anal. Methods* 7020–7028 (2015). doi:10.1039/C5AY00522A

Chapter 5: Fiber Lasers for Two-photon Microscopy⁴

5.1 INTRODUCTION

First developed in early 1990's, two-photon microscopy is a powerful optical sectioning technique ideal for deep imaging of biological samples with submicron resolution¹. The field of neuroscience saw a number of discoveries enabled by this technique^{2,3}. The critical enabling tool for two-photon microscopy has been the ultrafast laser, typically <200 fs in pulse duration and emitting in the near infrared region >750 nm. For the past two decades, titanium-doped sapphire (Ti:S) lasers have been the industry standard for deep two-photon microscopy due to relatively robust optical design, high stability, high output power, and wide wavelength tuning (700-1000 nm) over a range accessible to most standard dyes. However, the system cost and complexity of these lasers typically limits their use to specialized labs, or as shared resources. Furthermore, at the upper limit of the tuning range (1000 nm) the output power typically degrades four-fold. It is well known that a longer excitation wavelength allows significantly deeper penetration into tissues^{4,5} and offers a broad the range of usable fluorescence proteins, many of which have a peak two-photon cross-section between 900-1100 nm^{6,7}. To better investigate intact neurons and vasculature in a living mouse, it will be necessary to utilize light sources that offer deeper imaging than Ti:S lasers and with emission wavelengths that better overlap with the new generation of fluorescent proteins.

Alternatives to the Ti:S laser for biological microscopy have been explored in the past decade. A gain switched laser emitting at 980 nm was demonstrated for two-photon imaging an *ex vivo* mouse tissue⁸. Another study used a semiconductor based laser and

⁴ Portions of this chapter were adapted from: E.P. Perillo, J.E. McCracken, D.C. Fernée, J.R. Goldak, F.A. Medina, D.R. Miller, H.-C. Yeh, and A.K. Dunn, "Deep in vivo two-photon microscopy with a low cost custom built mode-locked 1060 nm fiber laser," *Biomedical Optics Express*, 7, 324-334 (2016). E.P.P. conceived the project, designed and built the laser, carried out the experiments, analyzed the data, and wrote the manuscript.

amplifier system with a 5 ps pulse to image neurons labelled with eYFP *in vivo*⁹. Of the alternatives to Ti:S laser systems, the fiber laser is potentially the most promising. Fiber lasers offer excellent pump absorption efficiency, high pulse energy, entirely passive mode-locking, and no need for active cooling^{10,11}. Several groups have demonstrated two-photon imaging with fiber laser systems. One group utilized a homebuilt system with grating compressor to obtain pulse widths down to 384 fs with 80 mW average power¹². Commercial fiber lasers with photonic crystal fiber have been employed for widely tunable systems¹³, and for fiber delivery of femtosecond pulses to the sample¹⁴. Previous demonstrations of homebuilt and commercial fiber lasers have shown a great potential to be used as a low cost alternative to the Ti:S laser for *in vivo* imaging, however their pulse energy and average power is not sufficient to be used for deep *in vivo* brain imaging.

Recently, fiber lasers making use of the All Normal Dispersion (ANDi) design have allowed for power scaling up to 20 nJ pulse energy¹⁵, but the use of a single mode pump laser limits the usable output to an average power of only 200 mW. A further improvement to the ANDi design enabled 10 times scaling of average power by switching to a multimode pumped laser and double clad gain fiber^{16,17}. Despite the relatively simple optical design of the ANDi laser, it has seen limited use in two-photon microscopy systems. In this report we describe the performance of a double clad – multimode pumped ANDi ytterbium fiber laser, built in our lab, for deep-tissue *in vivo* brain imaging. We demonstrate that a robust and stable system can be built from entirely off the shelf commercial components for only \$13,000, or approximately 1/10th the cost of a commercial Ti:S laser system. We characterize the laser to have a central wavelength of 1060 nm, with a 40 nm bandwidth. The laser emits 8 ps pulses that can be extracavity compressed to 81 fs. Two-photon imaging is demonstrated at depths up to 900 μm in an intact living mouse brain with YFP labelled layer-V neurons and Texas Red perfused vasculature.

5.2 YTTERBIUM FIBER OSCILLATOR

5.2.1 Instrumentation

The self-starting mode-locked operation of the laser is based upon the non-linear polarization rotation effect^{18,19}. Typical fiber laser designs utilize a single mode core with single mode pump which limits the usable output power to approximately 200 mW¹⁵. Here we adopt a multimode pump – double clad fiber design¹⁷. The gain medium lies within a 10 μm core large-mode area double clad fiber (YDF) (YB1200-10/125DC, nLIGHT Photonics), in this region the pump light from a multimode diode ($\lambda = 976 \text{ nm}$) travels within the cladding of the YDF and is absorbed through chance encounters with the ytterbium-doped core of the fiber. This design allows scaling of the output power to 30 nJ pulses with uncompressed average powers of 1.2 W at a repetition rate of 40 MHz.

The laser is a ring cavity as seen in **Figure 5.1** with a total fiber cavity length of approximately 4.8 m and a small free space portion. The gain medium consists of 2.5 m of ytterbium-doped double clad fiber (YDF) followed by a pigtailed collimator (F220FC-1064, Thorlabs) with 0.8 m of HI1060 fiber. High power patch cable with a mechanically cleaved air gap (SMJ-A3HPC-X-1060-6/125-1-3, Oz Optics) is used to prevent damage during mode-locked operation. A free space portion of the laser accomplishes several tasks: (1) polarization control with waveplates, (2) ejection of pulses via a polarizing beam splitter, (3) unidirectional cavity with an isolator, and (4) spectral tuning through a birefringent filter plate. A second collimator with 0.5 m of HI1060 fiber is spliced onto 0.5 m of un-doped double clad fiber (UDCF) on the signal line of a multimode pump combiner (MMC02112CC0A, 3SP Group). A 10 W multimode fiber coupled diode pump laser (L4-9897603-100B, JDSU) provides the energy for lasing. Another 0.5 m of UDCF follows the pump combiner and is spliced onto the YDF closing the ring cavity. To reduce loss in the

cavity from the mismatched core sizes at the splice joints between HI1060 and DC fiber we splice ~2 cm of an 8 μm core fiber (SMF28e, Corning).

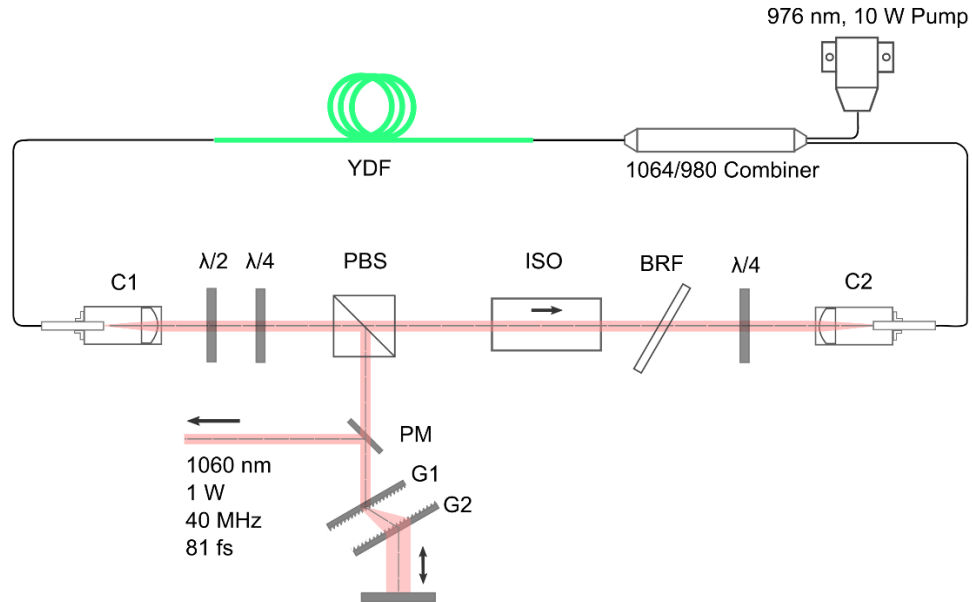


Figure 5.1 | Schematic of the mode-locked ytterbium fiber laser.

The majority of the cavity lies within 4.8 meters of optical fiber. A free space portion is used to eject the pulses with a polarizing beam splitter (PBS). Half-wave and quarter-wave plates control the polarization rotation effect which initiates and sustains mode-locking. The birefringent filter plate (BRF) allows control of the spectral bandwidth in the cavity. G1 and G2 are transmission pulse compression gratings, PM is pick-off mirror, C1 and C2 are fiber collimators.

The spatial output of the fiber laser can be directly characterized by the light exiting from a single mode fiber collimator, C1 in **Figure 5.1**. These collimators (F220FC-1064, Thorlabs) have an average beam quality factor, $M^2 = 1.1$, as characterized by the manufacturer. The divergence angle was calculated from ray optics to be 0.5 mrad, while the beam size is 2.4 mm in diameter.

External to the cavity is a double pass, grating pair compressor to compensate for the large dispersion introduced by the cavity²⁰. The light is diffracted by two transmission

diffraction gratings with grating pitch of 1000 lines/mm (LSFSG-1000-3212-94, LightSmyth). The path is folded onto itself and picked off by a mirror to be reflected into the microscope setup.

5.2.2 Characterization

The laser achieves full output mode-locked operation at 4.5 W pump power and is able to maintain stability over an entire animal experiment duration, typically 4 hours. The longest consecutive time the laser was operated was for 10 hours, over which it remained stably mode-locked. The average power output directly from the cavity is 1.2W, after a four pass transmission grating compressor the usable power is 1 W.

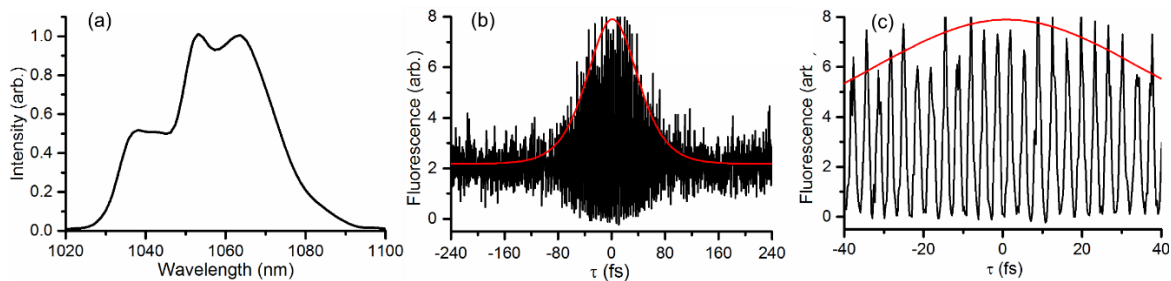


Figure 5.2 | Fiber Oscillator Characterization

(a) Emission spectrum of the mode-locked ytterbium laser. (b) Autocorrelation trace of the compressed pulse at the sample measured by *in situ* autocorrelation. The measured pulse width was found to be 127 fs full-width half max. Assuming a sech^2 pulse shape, the estimated pulse width is 81 fs. (c) Zoomed view of autocorrelation trace.

The spectral output was measured with a commercial spectrometer (AvaSpec-256-NIR1.7, Avantes) and found to be 40 nm bandwidth centered at 1060 nm [Figure 5.2(a)]. The pulse width nm at the sample was characterized by an *in situ* second-order autocorrelation technique²¹ [Figure 5.2(b)]. The pulse is long upon exiting the cavity (8

ps). With the external grating pair the pulse can be compressed down to 81 fs. It was found that a grating spacing of 20 mm provided the optimal pulse compression at the sample. The pulse is not transform limited because of large higher-order dispersion introduced by several meters of fiber cavity length¹⁷.

5.2.3 Build Protocol

Refer to **Table 5.1** for a list of the components used in this build. Fusion splicing of the fiber components is the first completion milestone, with laser alignment and mode-locking being the second and third milestones, respectively. Many of the fiber components are of differing core size and, for this reason, should be spliced using a core-alignment fusion splicer as opposed to V-groove. The splicer used for this build was a FFS200PM from Vytran. First, the HI1060 patchcord attached to the collimators, C1 and C2 in Fig 1, are spliced to a small section of SMF fiber (<2 cm). This intermediate splice allows a taper in core size from 5.2 μm up to 8.2 μm to reduce splice loss (<0.2 dB typical). The C1 fiber assembly (containing 0.8 m of HI1060 patch cable and 2 cm of SMF fiber) is spliced to the 2.5 m section of ytterbium doped gain fiber, typical splice loss for the entire assembly should reach 0.5 dB. Next, both assemblies, C1 and C2 are spliced to the multimode combiner output and input signal lines, respectively. The length of the input and output signal lines are both 0.5 m. The final splice is the 105 μm core multimode fiber coupled pump laser; no specific target fiber length is needed. The fiber output from the pump laser is spliced to either one of the multimode input fibers of the combiner unit, the other input line can be left unused. A (1+1)x1 combiner may also be used.

Description	Supplier	Manufacturer's Part #	Price	Qty.
10 W, 976 nm Laser Diode Pump	JDS Uniphase	L4-9897603-100B	\$325	1
20 A Laser Diode Driver	Arroyo Instruments	4320	\$1995	1
28W TEC Driver	Arroyo Instruments	585-04-08	\$695	1
TEC Laser Mount	Arroyo Instruments	207	\$595	1
(2+1)x1 Multimode Combiner	3SP Group	MMC02112CC0A	\$460	1
Ytterbium-Doped LMA Double Clad Fiber	Thorlabs	YB1200-10/125DC	\$168	3
High-power HI1060 Patchcord	Oz Optics	SMJ-A3HPC,X-1060-6/125-1-3	\$189	2
1064 nm, FC/PC Fiber Collimation Pkg.	Thorlabs	F220FC-1064	\$134	2
Polarizing Beamsplitter Cube, 900-1300 nm	Thorlabs	CM05-PBS203	\$255	1
Achromatic Quarter Waveplate, 690-1200 nm	Thorlabs	AQWP05M-980	\$783	2
Achromatic Half Waveplate, 690-1200 nm	Thorlabs	AHWP05M-980	\$783	1
1 mm thk. Quartz Birefringent Plate	OFR	BF-16-1.00	\$275	1
60 W Max, 1064 nm Isolator	Thorlabs	IO-5-1064-HP	\$2435	1
High-Precision Rotation Mount for Ø1" Optics	Thorlabs	PRM1	\$260	4
1000 line/mm Transmission Grating	LightSmyth	LSFSG-1000-3212-94	\$395	2
Breadboard, 2' x 1.5' x 2.2", 1/4"-20 Taps	Newport	PBG12118	\$654	1

^aOpto-mechanical components have been omitted and can be selected based on user preference.

Table 5.1 | Summary of select components used in laser build

Once all of the fiber splices have been completed, the alignment process can begin. The first step in laser alignment is to close the circular cavity and obtain lasing, this is accomplished by aligning the output collimator, C1, to the input collimator, C2, through the isolator, ISO. An isolator should always be used during alignment for stability and to avoid damaging the components. The waveplates and birefringent plate are not necessary to achieve lasing. The pump power should be set to a value near the lasing threshold, for this laser cavity the lasing threshold is at approximately 1.5W of pump power. Upon lasing, the waveplates and BRF can be inserted into their respective locations as described by **Figure 5.1**. The alignment should be adjusted again to maximize output power. The BRF should be placed near the Brewster angle. Mode-locking can be achieved by systematically rotating the waveplates and BRF at a high enough pump power for non-linear polarization evolution to occur. The mode-locking threshold for this laser is approximately 3.5 W of pump power. The specific angles for waveplates and the BRF that achieve mode-locking will vary between different builds. During rotation of the waveplates to achieve mode-locking we never noticed damage to the high power patch cable collimators, even with higher pump powers of 5-6 W. With standard epoxy polished terminated fiber, damage occurred during rotation of waveplates to both the input and output end-faces of the fiber collimators.

5.3 DEEP IN VIVO IMAGING WITH FIBERLASER

5.3.1 Animal Procedure

All animal procedures were reviewed and approved by the University of Texas at Austin Institutional Animal Care and Use Committee (protocol number AUP-2015-00011) and were conducted in strict accordance with the Guide for the Care and Use of Laboratory

Animals (published by NIH), the Public Health Service Policy on Humane Care and Use of Laboratory Animals, and the Animal Welfare Act and Animal Welfare Regulations.

5.3.2 Chronic preparation

A genetically modified C57BL/6 mouse (female, 20-g) expressing yellow fluorescent protein in layer V pyramidal neurons was anesthetized using 5 percent isoflurane (VetOne). Eye ointment was applied and the temperature was monitored and kept constant at 37.5°C with a feedback heating plate (World Precision Instruments Inc., Sarasota, FL). Next, Carprofen (5mg/kg, subcutaneous) and dexamethasone sodium phosphate (2mg/kg, intramuscular) were administered to control inflammation. The mouse was transferred into a stereotaxic frame. The mouse head was cleaned with ethanol, lidocaine was applied under the head skin and the skin from the top of the head was removed using scissors. The scalp was exposed and a ~4 mm circular diameter portion of the skull was removed (center located at 3 mm lateral and 3 mm caudal from bregma). A 5 mm sterile glass #1.5 cover slip (502040, World Precision Instruments) was placed over the craniotomy and glued to the skull using cyanoacrylate and dental cement. After sealing the craniotomy, the animal was removed from anesthesia and allowed to recover for two weeks. Carprofen injections were given daily for the next 2 days after surgical procedure. The procedure was performed using autoclaved tools and materials.

5.3.3 Imaging session

For the imaging sessions the YFP mouse was placed into the stereotaxic frame, kept under isoflurane anesthesia, body temperature was maintained at 37.5°C and 0.1 mL subcutaneous injections of 5% (w/v) glucose in physiological saline were applied every hour. After verifying that the mice was under anesthesia by a lack of the paw pinch reflex,

blood plasma was labeled via an intraorbital injection of 5% (w/v) Texas Red-dextran (D1864, Invitrogen) dissolved in physiological saline.

5.3.4 Two-Photon Microscope

Two-photon laser scanning microscopy was performed on a custom built upright microscope for animal imaging²² [**Figure 5.3(a)**]. The laser is expanded with a two lens telescope assembly before being projected onto an xy-galvo mirror pair (6125H, Cambridge Tech.). A scan (25 mm) and tube lens (125 mm) are used to reimage the scanned laser onto the back aperture of the microscope objective (XLUMPLFLN 20× 0.95 NA, Olympus). Fluorescence light is epi-collected and reflected towards the detectors by a dichroic mirror, DM1 (FF775-Di01-25x36, Semrock). The detectors are 5 mm area, short working distance, uncooled PMTs (H10770PB-40, Hamamatsu Photonics). A dichroic filter, DM2 separates emitted light into two channels. Emission filters are placed directly in front of the PMTs, corresponding to green (FF01-534/42-25, Semrock) for YFP, and red (FF01-534/42-25, Semrock) for Texas Red. The analog waveform from each PMT is sent to a current preamplifier before being digitized by a PCI-based DAQ (PCI-6353, National Instruments).

Laser speckle contrast imaging (LSCI) was used to locate the optimal location to record two-photon image stacks²³. At the start of an experiment, a laser speckle contrast image was taken [Fig. 3(b)] using a laser diode ($\lambda = 785$ nm) and a CCD camera through the same objective as used for imaging. Following the laser speckle imaging, two-photon microscopy was performed.

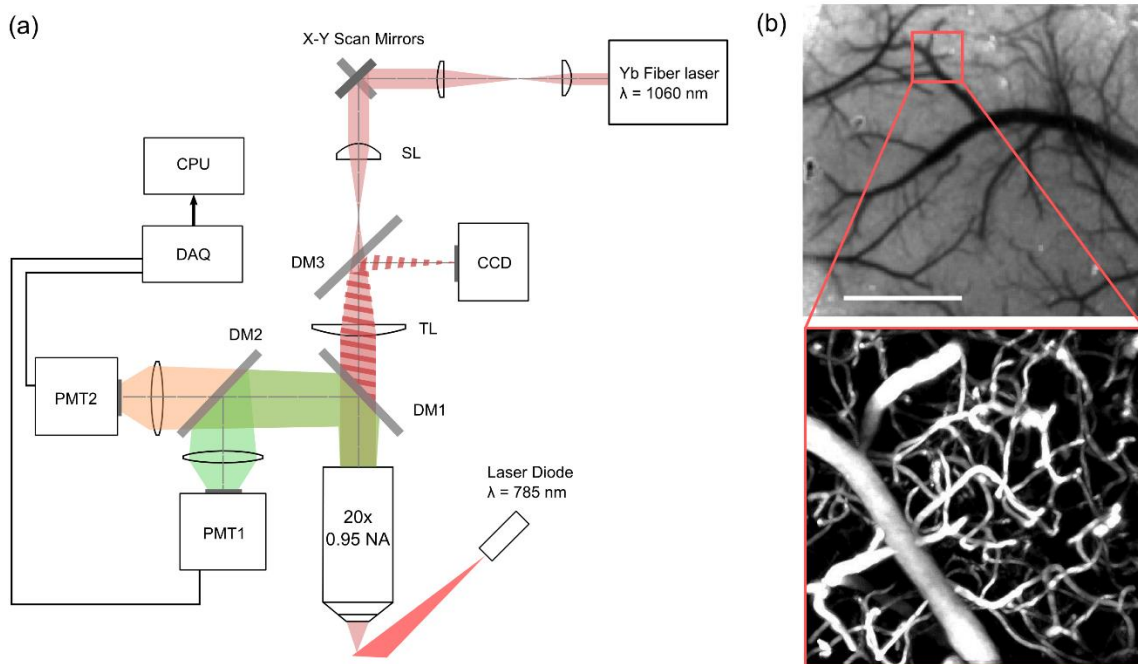


Figure 5.3 | Two-Photon Microscope

(a) Custom two-photon instrument schematic. SL: scan lens, TL: tube lens, DM1, DM2, DM3: dichroic mirrors with transmission lines: $T > 775$ nm, $T > 570$ nm, and $T > 795$ nm, respectively (b) Laser speckle contrast image of the mouse craniotomy. The scale bar is $800 \mu\text{m}$. (zoomed view: a representative two-photon maximum intensity z-projection of a $400 \times 400 \times 200 \mu\text{m}^3$ stack. The vessels are perfused with Texas Red.

For a typical experiment, we used a $400 \mu\text{m}$ field of view and image resolution of 512×512 pixels, corresponding to a pixel size of 781 nm. The pixel integration time was $2.66 \mu\text{s}$ and images were acquired at 1 Hz. At the surface and up to $700 \mu\text{m}$ 5 frame averaging was used, while at depths greater than $700 \mu\text{m}$ 10 frame averaging was used.

5.3.5 Vasculature Imaging

Deep brain imaging using the custom 1060 nm fiber laser was performed in an anesthetized YFP mouse with a previously implanted cranial window. Images of the brain were obtained using LSCI for reference followed by two-photon microscopy. 3D images

stacks were taken with 5 μm separation between image planes. A power of 20 mW at the objective back aperture was used for surface level imaging, while 200 mW was needed for depths of $>700 \mu\text{m}$. A variable neutral density filter allowed for manual control of laser power at varying depths. A comparatively higher power was required for surface level imaging due to low objective transmission ($\sim 65\%$ at 1060 nm) and off peak excitation of Texas Red and YFP ($<60\%$ relative to peak)^{24,25}. It is possible that using a fluorophore with a better matched 2P cross-section at 1060 nm would allow for a lower excitation power for surface level imaging.

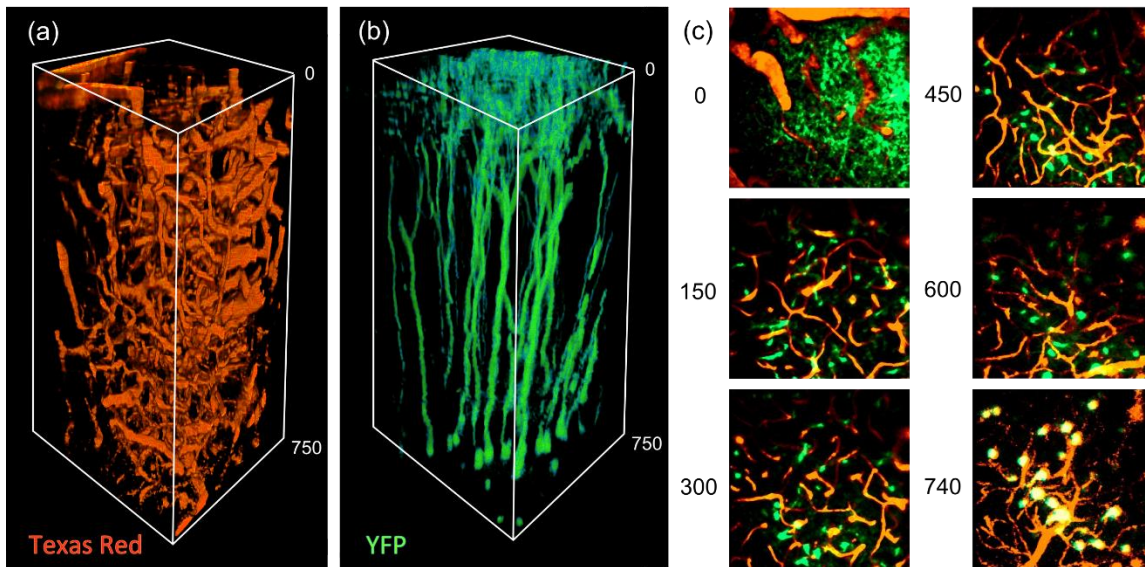


Figure 5.4 | Deep in vivo Neuron and Vasculature Stack with Fiber Oscillator

(a and b) Image stack of dimensions $400 \times 400 \times 750 \mu\text{m}^3$ taken with two-photon laser scanning microscopy labeling for (a) microvasculature with Texas Red, and (b) Neurons expressing YFP. (c) 2D z-projections at various depths through the stack, the image at each plane is a maximum intensity projection of the nearest $10 \mu\text{m}$.

Images of vasculature perfused with Texas Red and neurons expressing YFP, as shown in **Figure 5.4**, were measured to depths up to $750 \mu\text{m}$. Rendering of the 3D stack

data is performed with a 3D visualization software (Aviso standard, VSG). **Figure 5.4(c)** shows a merged plane projection images at various depths through the stack. Each plane is a maximum intensity z-projection image of the nearest 10 μm . From [**Figure 5.4(b)**], we can observe the progression of neural structure from the top ~ 100 μm of branching dendrites down to the neuron bodies at depths of 700-800 μm .

We further investigate the neuron structural imaging capability of the laser and compare performance to that of a commercial Ti:S laser tuned to 920 nm. Two stacks were recorded down to 900 μm in two different mice using a commercial Ti:S laser (Mira 900, Coherent) and the custom fiber laser. For the fiber laser, the same previously mentioned back aperture excitation powers were used at the surface (20 mW) and at depth (200 mW), while the Ti:S laser used a proportionally scaled excitation pulse energy to account for the decreased 2P cross-section of YFP at 920 nm. The Ti:S excitation power ranged from 30 mW at the surface to 380 mW at 900 μm depth. The same frame averaging conditions were performed with each laser. In both cases we observe neuron bodies at depths around 700 μm [**Figure 5.5(a)**]. Although, with the commercial Ti:S laser, past ~ 650 μm the background signal increased dramatically. With the Ti:S at 900 μm the signal-to-noise ratio (SNR) was so low that no structure could be resolved, whereas with the fiber laser SNR remained acceptable throughout the 900 μm image. Although experimental conditions can vary, in this specific case we see that the 1060 nm fiber laser offers superior deep imaging capability to that of a Ti:S laser tuned near the end of its standard operating range, 920 nm. The difference in excitation wavelengths between the two lasers has a notable impact on the imaging performance, however additional differences such as shorter pulse width (81 fs vs. 150 fs), and lower auto-fluorescence from the fiber laser are likely significant factors in the improved imaging depth.

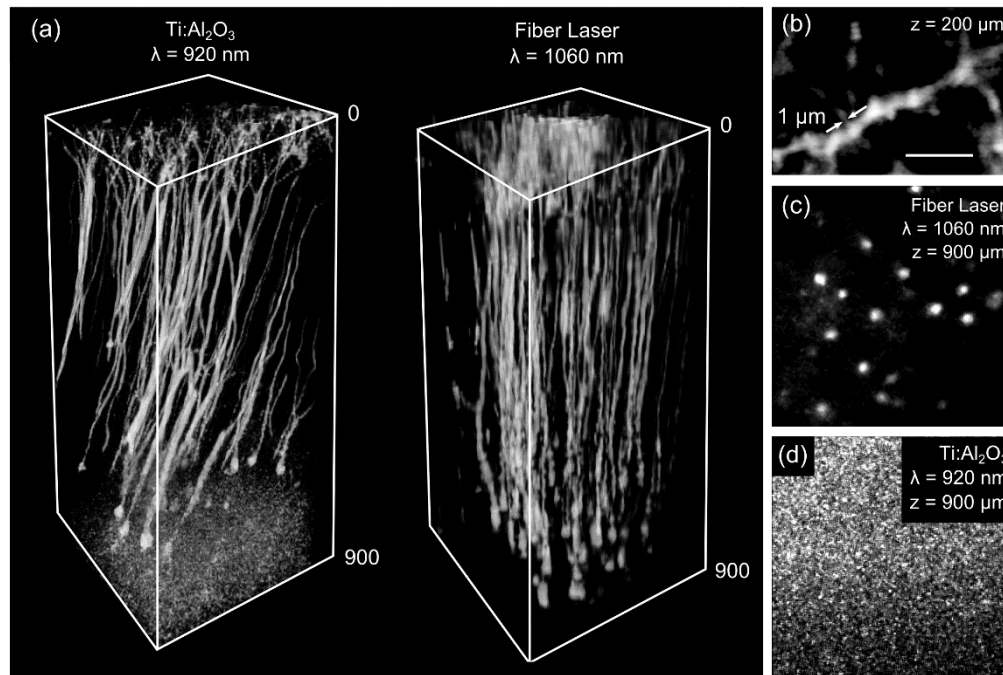


Figure 5.5 | Deep *in vivo* neuron imaging comparison between Ti:S and fiber laser

(a) Deep imaging comparison between a commercial Ti:S laser tuned to 920 nm and the custom built 1060 nm fiber laser. Image dimensions $400 \times 400 \times 900 \mu\text{m}^3$. Fluorescence stacks are pyramidal neurons expressing YFP taken in two separate mice. (b) A zoomed in view of a dendrite at 200 μm depth taken with the fiber laser. Single dendritic spines can be visualized with sub 1 μm features. Scale bar is 8 μm . (c) An image of pyramidal neuron bodies at 900 μm depth taken with the fiber laser. (d) An image at 900 μm depth taken with a commercial Ti:S laser, neuron structures cannot be resolved.

Upon zooming in to a single apical dendrite at 200 μm depth with the fiber laser, it is possible to resolve single dendritic spines [Figure 5.5(b)]. In this case our image resolution was no longer limited by the pixel size (64 nm), but instead, by optical diffraction (~ 350 nm). We observe that the thin features of dendritic spines are still easily resolvable using 1060 nm light, even to depths of 200 μm . Going to depths further than 900 μm yielded no signal even with increasing laser power. Although YFP had acceptable SNR with 10 frame averaging at 900 μm [Figure 5.5(c)], the signal level decayed past that point, indicating that a practical depth limit had been reached. It is likely that the poor SNR

past 900 μm was due to loss of signal rather than an overwhelming noise from out of focus fluorescence. With a higher peak power, a brighter fluorophore, or better collection optics, it should be possible to obtain even deeper imaging with the 1060 nm wavelength. For example, using a fluorescent protein such as tdTomato would allow for even deeper imaging due to its significantly greater two-photon cross-section around 1060 nm⁶.

5.4 DISCUSSION

This work demonstrates that with our microscopy setup and custom laser we can achieve a practical imaging depth of 900 μm in an intact live mouse brain, which is superior to most standard Ti:S laser oscillators operating at 800 nm⁵, and comparable to studies performed with Ti:S regenerative amplifiers^{26,27}. Comparing the specifications of the demonstrated 1060 nm laser and modern Ti:S lasers that are tunable out to 1060 nm, it is clear that the fiber laser offers higher performance at the 1060 nm wavelength. With 8 \times higher pulse energy and a shorter pulse width (81 fs vs. 140 fs), the fiber laser has a peak power well over an order of magnitude above Ti:S systems. Given the difference in peak power the fiber laser should be capable of achieving significantly deeper imaging than a modern Ti:S tuned to the same wavelength. In terms of pulse repetition rate, duty cycle, and photodamage the fiber laser should offer comparable performance to that of a Ti:S laser. Tissue heating from water absorption can be a concern when using longer excitation wavelengths. Despite almost 3 orders of magnitude higher water absorption at 1060 nm versus 800 nm, it is unlikely that tissue damage due to heating is increased. There has been shown to be insignificant heat accumulation in tissue samples (<0.2 K at 800 nm) with femtosecond pulsed lasers,²⁸ due to comparatively low pulse energy. Femtosecond pulses do not generate sufficient absorption over the image area to increase temperature by 1K within the sample even with wavelengths out to 1300 nm where absorption is much

higher.²⁹ Furthermore, even though the absorption of water is significantly higher at 1060 nm versus 800 nm, the overall tissue absorption coefficient is within a factor of two due to the increased absorption of oxygenated and deoxygenated hemoglobin at 800 versus 1060 nm.³⁰

Although groups have demonstrated imaging as deep as 1 mm with a regenerative amplifier, it should be noted that regenerative amplifiers have as much as 100 times the pulse energy, and at 50 times lower duty cycle – the combination of which can lead to poor image quality, slow acquisition, and tissue damage. Certain studies use regenerative amplifiers specifically to damage healthy brain tissue through optical breakdown effects with high pulse intensities³¹. With our setup, there was no damage to the surface of the brain through extravasation, or hemorrhaging even with the highest tested power of 500 mW at the back aperture.

Other groups have utilized lasers with even longer excitation wavelengths, in the range of 1200-1700 nm, that are capable of imaging to up to 1.6 mm in a living mouse brain. These systems are built upon either commercial OPOs³², or are a mix of custom and commercial products³³. We emphasize that our system is entirely custom built, and for an order of magnitude lower cost. Yet, our fiber laser can achieve imaging depth close to that of the more complicated systems such as OPOs, or Ti:S regenerative amplifiers.

This specific laser embodiment provides sufficient pulse energy, 30 nJ, and average uncompressed power, 1.2 W, to image deep in highly scattering tissues. Although, in practice, it is possible to further scale the average power up to 2.4 W by increasing the repetition rate to 80 MHz¹⁶. Power scaling beyond 30 nJ pulse energy has been demonstrated by using large-mode-area photonic crystal fibers to manage instability from higher-order modes.^{34,35} However, these systems typically suffer from increased alignment complexity due to free space coupled pump light.

In this work we detail the construction and application of an all normal dispersion mode-locked ytterbium fiber laser for two-photon microscopy³⁶. The laser achieves stable and self-starting mode-locking at 1060 nm center wavelength with 81 fs compressed pulses and a rate of 40 MHz. We use this custom built laser to demonstrate *in vivo* two-photon imaging of the intact brain of a living mouse down to a depth of 900 μm . Based on the simplicity and low cost of this laser design we believe it will be a highly valuable tool for labs that cannot afford traditional Ti:S laser systems. The cost alone would be a large draw for any neuroscience groups wishing to study intact neuron structure and function *in vivo*, where a Ti:S laser system would be otherwise impractical or not feasible. Furthermore, the longer wavelength allows deeper penetration into tissue, and access to a wider range of fluorescent proteins than possible with Ti:S lasers emitting between 700-900 nm. It is clear that the fiber laser approach has numerous benefits over traditional femtosecond mode-locked lasers and we expect to see more labs adopt fiber lasers for their multiphoton microscopy research in the near future.

5.5 REFERENCES

1. Denk, W., Strickler, J. H. & Webb, W. W. Two-photon laser scanning fluorescence microscopy. *Science* **248**, 73–76 (1990).
2. Grutzendler, J., Kasthuri, N. & Gan, W.-B. Long-term dendritic spine stability in the adult cortex. *Nature* **420**, 812–816 (2002).
3. Matsuzaki, M., Honkura, N., Ellis-Davies, G. C. R. & Kasai, H. Structural basis of long-term potentiation in single dendritic spines. *Nature* **429**, 761–766 (2004).
4. Dunn, A. K., Wallace, V. P., Coleno, M., Berns, M. W. & Tromberg, B. J. Influence of optical properties on two-photon fluorescence imaging in turbid samples. *Appl. Opt.* **39**, 1194–1201 (2000).
5. Oheim, M., Beaurepaire, E., Chaigneau, E., Mertz, J. & Charpak, S. Two-photon microscopy in brain tissue: parameters influencing the imaging depth. *J. Neurosci. Methods* **111**, 29–37 (2001).
6. Drobizhev, M., Tillo, S., Makarov, N., Hughes, T. E. & Rebane, A. Absolute Two-photon Absorption Spectra Of Orange And Red Fluorescent Proteins. *J. Phys. Chem. B* **113**, 855–859 (2009).
7. Drobizhev, M., Makarov, N. S., Tillo, S. E., Hughes, T. E. & Rebane, A. Two-

- photon absorption properties of fluorescent proteins. *Nat. Methods* **8**, 393–399 (2011).
8. Taira, K., Hashimoto, T. & Yokoyama, H. Two-photon fluorescence imaging with a pulse source based on a 980-nm gain-switched laser diode. *Opt. Express* **15**, 2454–2458 (2007).
 9. Kawakami, R. *et al.* Visualizing hippocampal neurons with in vivo two-photon microscopy using a 1030 nm picosecond pulse laser. *Sci. Rep.* **3**, 1014 (2013).
 10. Xu, C. & Wise, F. W. Recent advances in fibre lasers for nonlinear microscopy. *Nat. Photonics* **7**, 875–882 (2013).
 11. Fermann, M. E. & Hartl, I. Ultrafast fibre lasers. *Nat. Photonics* **7**, 868–874 (2013).
 12. Kim, D. U. *et al.* Two-photon microscopy using an Yb(3+)-doped fiber laser with variable pulse widths. *Opt. Express* **20**, 12341–9 (2012).
 13. Unruh, J. R. *et al.* Two-photon microscopy with wavelength switchable fiber laser excitation. *Opt. Express* **14**, 9825–9831 (2006).
 14. Tang, S., Liu, J., Krasieva, T. B., Chen, Z. & Tromberg, B. J. Developing compact multiphoton systems using femtosecond fiber lasers. *J. Biomed. Opt.* **14**, 30508 (2009).
 15. Chong, A., Renninger, W. H. & Wise, F. W. All-normal-dispersion femtosecond fiber laser with pulse energy above 20 nJ. *Opt. Lett.* **32**, 2408–10 (2007).
 16. An, J., Kim, D., Dawson, J. W., Messerly, M. J. & Barty, C. P. J. Grating-less, fiber-based oscillator that generates 25 nJ pulses at 80 MHz, compressible to 150 fs. *Opt. Lett.* **32**, 2010–2 (2007).
 17. Kieu, K., Renninger, W. H., Chong, a & Wise, F. W. Sub-100 fs pulses at watt-level powers from a dissipative-soliton fiber laser. *Opt. Lett.* **34**, 593–5 (2009).
 18. Hofer, M., Fermann, M. E., Haberl, F., Ober, M. H. & Schmidt, a J. Mode locking with cross-phase and self-phase modulation. *Opt. Lett.* **16**, 502–504 (1991).
 19. Chong, A., Renninger, W. H. & Wise, F. W. Properties of normal-dispersion femtosecond fiber lasers. *J. Opt. Soc. Am. B* **25**, 140 (2008).
 20. Shank, C. V., Fork, R. L., Yen, R., Stolen, R. H. & Tomlinson, W. J. Compression of femtosecond optical pulses. *Appl. Phys. Lett.* **40**, 761–763 (1982).
 21. Xu, C., Guild, J., Webb, W. & Denk, W. Determination of absolute two-photon excitation cross sections by in situ second-order autocorrelation. *Opt. Lett.* **20**, 2372 (1995).
 22. Kazmi, S. M. S. *et al.* Three-dimensional mapping of oxygen tension in cortical arterioles before and after occlusion. *Biomed. Opt. Express* **4**, 1061–73 (2013).
 23. Schrandt, C. J., Kazmi, S. M. S., Jones, T. a & Dunn, A. K. Chronic monitoring of vascular progression after ischemic stroke using multiexposure speckle imaging and two-photon fluorescence microscopy. *J. Cereb. Blood Flow Metab.* **35**, 933–942 (2015).
 24. Bestvater, F. *et al.* Two-photon fluorescence absorption and emission spectra of dyes relevant for cell imaging. *J. Microsc.* **208**, 108–15 (2002).
 25. Spiess, E., Bestvater, F., Heckel-Pompey, A. & K. -photon excitation and emission

- spectra of the green fluorescent protein variants eCFP,. *J. Microsc.* **217**, 200–204 (2005).
26. Beaulieu, E., Oheim, M. & Mertz, J. Ultra-deep two-photon fluorescence excitation in turbid media. *Opt. Commun.* **188**, 25–29 (2001).
 27. Theer, P., Hasan, M. T. & Denk, W. Two-photon imaging to a depth of 1000 microm in living brains by use of a Ti:Al₂O₃ regenerative amplifier. *Opt. Lett.* **28**, 1022–4 (2003).
 28. Schönle, A. & Hell, S. W. Heating by absorption in the focus of an objective lens. *Opt. Lett.* **23**, 325 (1998).
 29. Kobat, D. *et al.* Deep tissue multiphoton microscopy using longer wavelength excitation. *Opt. Express* **17**, 13354–64 (2009).
 30. Bevilacqua, F. *et al.* In vivo local determination of tissue optical properties: applications to human brain. *Appl. Opt.* **38**, 4939–4950 (1999).
 31. Nishimura, N. *et al.* Targeted insult to subsurface cortical blood vessels using ultrashort laser pulses: three models of stroke. *Nat. Methods* **3**, 99–108 (2006).
 32. Kobat, D., Horton, N. G. & Xu, C. In vivo two-photon microscopy to 1.6-mm depth in mouse cortex. *J. Biomed. Opt.* **16**, 106014 (2011).
 33. Horton, N. G. *et al.* In vivo three-photon microscopy of subcortical structures within an intact mouse brain. **7**, 205–209 (2013).
 34. Lefrançois, S., Kieu, K., Deng, Y., Kafka, J. D. & Wise, F. W. Scaling of dissipative soliton fiber lasers to megawatt peak powers by use of large-area photonic crystal fiber. *Opt. Lett.* **35**, 1569–71 (2010).
 35. Baumgartl, M. *et al.* High average and peak power femtosecond large-pitch photonic-crystal-fiber laser. *Opt. Lett.* **36**, 244–6 (2011).
 36. Perillo, E. P. *et al.* Deep in vivo two-photon microscopy with a low cost custom built mode-locked 1060 nm fiber laser. *Biomed. Opt. Express* **7**, 324 (2016).

Chapter 6: Two-color two-photon Excitation with a Diamond Raman Laser

6.1 INTRODUCTION

Two-photon excitation (2PE) fluorescence microscopy is a widely used tool in neuroscience and biology for three-dimensional (3D) imaging of intact live specimen at the millimeter spatial scale with sub-micron resolution^{1,2}. Implementing 2PE with commonly used fluorescent dyes and proteins is readily accomplished with femtosecond titanium-doped sapphire (Ti:S) lasers emitting in the range of 700-1000 nm. Unfortunately, the restricted wavelength tuning range of Ti:S lasers often leads to compromises in excitation efficiency with multicolor imaging experiments. Optimal excitation of fluorescent labels is even more critical when coupling 2PE with functional techniques such as Ca²⁺ imaging³⁻⁵, pO₂ mapping⁶⁻⁸, and optogenetics⁹, where the probe selection is restricted. Additionally, many of the recently developed fluorescent proteins (e.g. mKate2, tdKatushka2, mNeptune, mCardinal) that offer exceptional brightness, long emission wavelength and photostability¹⁰⁻¹² have their 2PE peaks at longer wavelengths (1050-1200 nm), which enables deeper imaging in tissues^{13,14}. It has recently been shown that a 50-100% improvement in imaging depth can be obtained by using 1050-1700 nm excitation, as compared with 800 nm excitation^{15,16}.

Excitation of multiple far-red fluorophores and functional probes (Ca²⁺, pO₂, and optogenetic probes) which cover a broad spectral range presents a significant instrumentation challenge that cannot be achieved by a single Ti:S laser. Attempts to expand the palette of useable fluorophores have primarily relied on multiplexing excitation wavelengths through either discrete lasers,¹⁷ or with supercontinuum sources^{18,19}. However, in the case of discrete lasers, the approach often involves an optical parametric oscillator (OPO) pumped by a Ti:S laser (1050-1300 nm), which is not only limited by

output power (~200 mW) but also costly to implement, making this approach not available to many labs. While supercontinuum sources (600-1200 nm) are cheaper and provide flexible excitation wavelengths, they typically offer even lower power in a given spectral band (<10 mW), making these sources not suitable for deep tissue imaging.

Recently, an integrated and synchronized Ti:S laser and OPO system was used to perform both two-photon (2PE) and two-color two-photon (2C2P) excitation,²⁰ enabling simultaneous excitation of three distinct fluorophores spread over a 250 nm-wide spectral region (850, 960, and 1100 nm). However, this Ti:S-OPO system only demonstrated shallow tissue imaging (~300 μm) in *ex vivo* samples,^{20,21} likely due to insufficient output powers from the synchronized lasers at the sample. Furthermore, the high cost of the entire system may prevent its widespread use in the community. We believe the 2C2P excitation approach holds great promise for future deep, multicolor tissue imaging, as long as we can build a cost-effective multicolor excitation system with a longer excitation wavelength coverage (1050-1240 nm).

6.1.1 Existing Commercial Products

To date, current commercial products are available that output simultaneous two color synchronized pulses usable for biological fluorescence microscopy. However, their cost is often prohibitively expensive for biology and neuroscience labs (**Figure 6.1**). The platforms are typically based upon fiber amplifier pumped OPOs, which are challenging and costly to implement at the high power levels required for biological microscopy (>500 mW).

<p>Topitca</p> <ul style="list-style-type: none"> ◦ 780 nm, >500 mW ◦ 1050 nm, >1000mW ◦ 150 fs ◦ 80MHz 		<p>FemtoFiber dichro bioMP Er-Yb co-doped fiber amplifier, frequency doubled Er</p>
<p>Spectra Physics</p> <ul style="list-style-type: none"> • 1041 nm, 1.5 W, 200 fs • 680-1300nm, ~800mW, 120 fs • 80 MHz • Price: ~400,000 		<p>InSightDS+ Yb Amplified Fiber pumped OPO</p>
<p>Coherent</p> <ul style="list-style-type: none"> • 1041 nm, 1.5 W, 140 fs • 680-1300nm, ~800mW, 100 fs • 80 MHz • Price: ~400,000 		<p>Chameleon Discovery Yb Amplified Fiber pumped OPO</p>

Figure 6.1 | Commercial dual output laser systems

6.2 DUAL OUTPUT LASER SYSTEM FOR TWO COLOR EXCITATION

Here we demonstrate that such a low-cost multicolor excitation system can be built from a home-built high-powered ytterbium fiber amplifier, and a home-built diamond Raman laser. Diamond Raman lasers offer a promising alternative to the Ti:S pumped OPO for two-color excitation microscopy; as they are inherently dual output through synchronous pumping, relatively low cost, have a simple cavity design, and require no active cooling or phase matching within their crystal^{22,23}. Yet, to date, diamond Raman lasers have seen little use in microscopy. A Ti:S pumped diamond Raman laser has been used for asynchronous multi-color imaging in thin cell samples²⁴, and a Nd:YVO₄-pumped, picosecond diamond Raman laser emitting at 1240 nm has been demonstrated,²⁵ but not used for imaging. In our system, the two synchronized output wavelengths for 2PE are centered at 1055 nm (λ_1) and 1240 nm (λ_2), provided by the ytterbium fiber amplifier and

diamond Raman laser, respectively. Excitation at an effective wavelength of 1140 nm ($\lambda_3=2/(1/\lambda_1+1/\lambda_2)$) is achieved by spatiotemporal overlap of the two synchronized lasers (i.e. 2C2P).

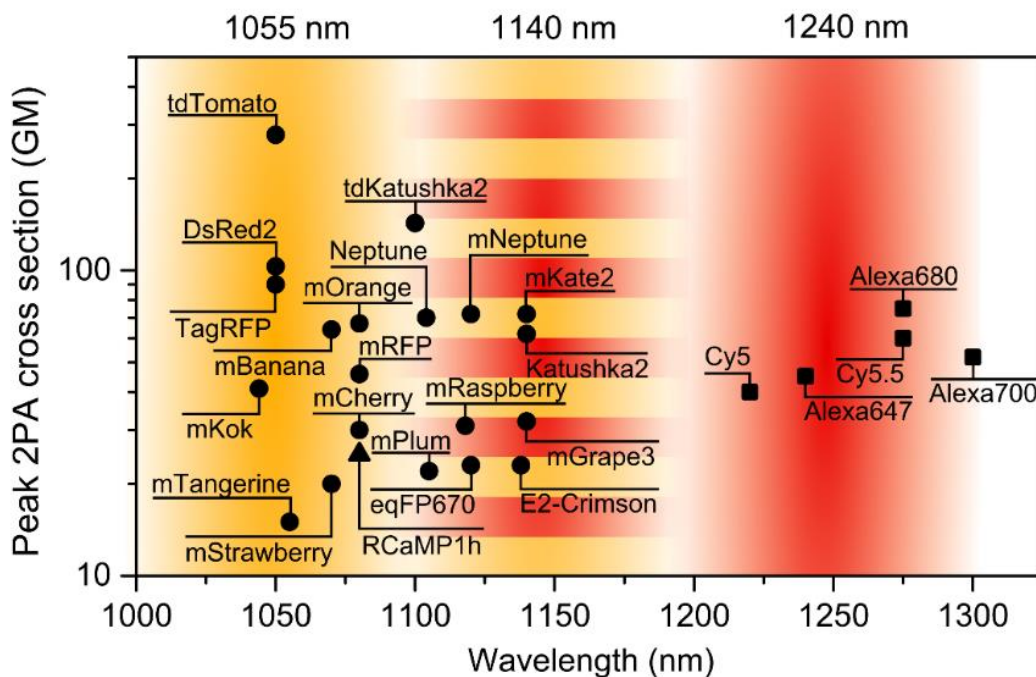


Figure 6.2 | Efficient excitation of far-red fluorophores with fiber-pumped diamond Raman laser.

A compilation of peak two-photon absorption cross sections from published literature^{5,11,26}. The triangle is from Ref. 5, circles are from Ref. 11, and squares are from Ref. 26. The three wavelength bands of the dual output laser system shown overlaid on the graph, 1240 nm diamond Raman laser (red), 1055 nm ytterbium fiber amplifier (orange), and 1140 nm 2C2P excitation (striped). The laser system offers simultaneous and complete excitation coverage for fluorophores within the range of 1000-1300 nm.

We have significantly extended the capabilities of two-color excitation for deep *in vivo* imaging; as our integrated fiber-diamond laser system offers not only higher output power (>500 mW) but also more suitable excitation coverage for far-red fluorescent proteins and dyes (90% increase in signal; **Figure 6.2**). Here we demonstrate deep *in vivo* imaging to nearly 1 mm in a mouse brain with 2C2P excitation (1140 nm) of Texas Red

perfused vasculature, which is a 20% depth increase when compared with 1055 nm excitation. The system cost is only about one-tenth that of a Ti:S-OPO system or commercial dual-output laser. Interestingly, when performing simultaneous multicolor imaging of Hoechst 33342 and tdKatushka2 within an engineered 3D tumor spheroid model, we found that Hoechst 33342 was excited by an unexpected two-color three-photon (2C3P) process, while tdKatushka2 was excited by the expected 2C2P process.

6.3 YTTERBIUM FIBER AMPLIFIER

The ytterbium fiber amplifier acts as both a source for imaging and a pump for the diamond Raman laser, therefore it is required to have sufficient output power, approximately 3W, while still maintaining femtosecond pulse-widths. We adopt an amplifier design that utilizes a single pass through large-mode-area fiber with input seed pulse parameters selected such that parabolic pulse evolution occurs^{27,28}. In the parabolic amplification regime, nonlinear spectral broadening is balanced by normal dispersion. As a result, the pulse acquires only a linear chirp, even through several meters of fiber, which is easily compensated by standard grating or prism compressors. Parabolic pulse amplifiers have been built with output powers as high as 10 W and sub-100 fs pulses²⁹⁻³¹. Here, a fiber core size was selected to achieve the target requirement of 3 W output power. The amplifier is seeded with 50 mW from a commercial oscillator (Origami-10, OneFive GmbH), amplified up to 3 W, and the output pulses are compressed with an external grating pair to 120 fs. The emission wavelength is 1055 nm with a repetition rate of 80 MHz.

6.3.1 Instrumentation

The amplifier consists of a 7 m long segment of double-clad ytterbium-doped large-mode-area optical fiber with a core size of 20 μm and cladding size of 400 μm (LMA-YDF-20/400-9M, Nufern). To avoid damage from high pulse energy, the fiber was custom

endcapped with a 1.2 mm long coreless fiber and angle polished in FC:APC connectors (Coastal Connections, Ventura, CA). By coiling the fiber to a radius of less than 10 cm, the higher order modes of the fiber are attenuated and single-mode output is enforced. The fiber is pumped with 7.5 W by a wavelength-stabilized laser diode emitting at 976 ± 0.1 nm (maximum available pump power of 12 W). The amplifier is seeded by a commercial oscillator emitting 80 fs pulses at 1050 nm (Origami-10, OneFive GmbH). The oscillator repetition rate (80 MHz) drives the repetition rate of the amplifier and diamond laser, in addition to defining the cavity length of the diamond laser. An optical isolator (IO-5-1050-HP, Thorlabs) placed between the amplifier and the seed laser blocks amplified spontaneous emission feedback into the seed source. After exiting the amplification fiber, the pulses are compressed with a two-grating two-pass geometry (G1, G2, in **Figure 6.3**) and the output is split using a Glan-type calcite polarizer, with the majority (2.5 W) going to pump the diamond laser, and the remainder (500 mW) going to the microscope to be used for imaging.

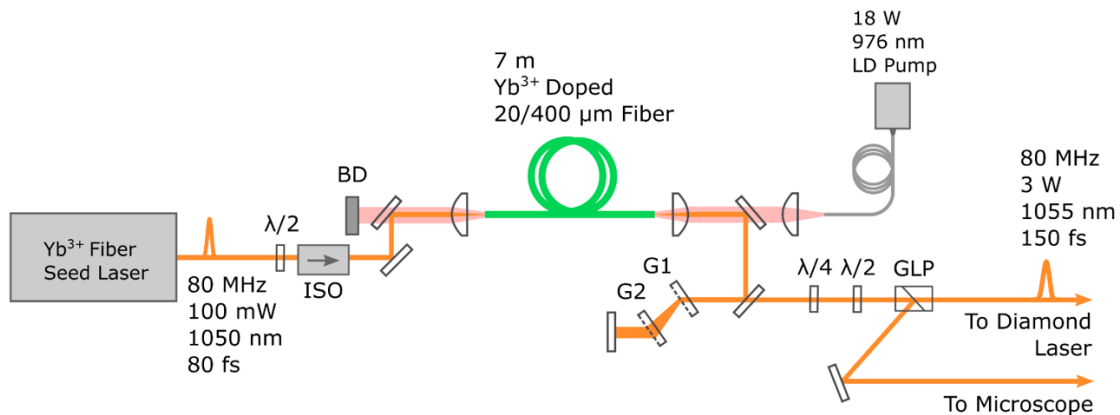


Figure 6.3 | Ytterbium Fiber Amplifier Schematic

Custom-built ytterbium fiber amplifier seeded by a commercial fiber oscillator. The amplified output is 3 W at 1055 nm with a pulse-width of 120 fs. ISO is isolator, BD is beam dump, GLP is Glan-laser polarizer, G1,G2 are transmission gratings.

Description	Supplier	Manufacturer's Part #	Price	Qty.
18 W 967 nm Laser Diode Pump	BWT Laser	K976AA2RN-18.00W	\$486.00	1
30W TEC High Power LaserMount	Arroyo Instruments	264-BB-9W4	\$895.00	1
LaserSource, 20A/7V Driver	Arroyo Instruments	4320-20-07	\$2,395.00	1
Yb-Doped Double Clad LMA Optical Fiber	Nufern	LMA-YDF-20/400-9M	\$252.00	7
FC/APC Fiber Endcap 1.3 mm	Coastal Connections	CUSTOM	\$414.00	1
1000 nm Shortpass Dichroic	Thorlabs	DMSP1000	\$261.00	2
Fiber Launch Stage	Thorlabs	MAX355D	\$1,729.00	1
1050 nm Isolator	Thorlabs	IO-5-1050-HP	\$2,490.00	1
1000 lines/mm Trans. Gratings	LightSmyth	T-1000-1040-3212-94	\$400.00	2
Origami – 10 fs Fiber Laser	OneFive GmbH	OR/SM/80/10530/100/100/F S	\$28,080.00	1

Table 6.1 | Summary of select components used in fiber amplifier build

An outline of the select critical components used in the laser build (**Table 6.1**) demonstrates that the system is relatively simple, and low cost. For example, the total cost of the amplifier including seed laser is \$40,000, which is approximately half the cost of a commercial system operating with the same output power, wavelength, and pulse width.

6.3.2 Parabolic Amplifier Design

The fiber amplifier was designed to be parabolic evolution through previous demonstrations^{32,33}. The primary design drivers for parabolic pulse amplifiers are optimal seed pulse duration ΔT_{opt} , Optimal seed pulse energy E_{opt} , and desired gain per unit length g . All numerical investigations for pulse evolution within optical fiber can be modelled as a nonlinear Schrödinger equation (NLSE) given by,

$$i \frac{\partial A}{\partial z} = \frac{1}{2} \beta_2 \frac{\partial^2 A}{\partial T^2} - \gamma |A|^2 A + i \frac{g}{a} A \quad (1)$$

The NLSE shows that the primary pulse shaping mechanisms are, normal dispersion of the fiber β_2 , nonlinearity parameter of the fiber γ , and gain g . For a parabolic pulse to properly form, these parameters must be selected and balanced appropriately.

Given that most standard telecom, and doped glass fiber have a nonlinearity factor of $\beta_2 = 0.02 \text{ ps}^2 \text{ m}^{-1}$, and that the nonlinearity parameter of the fiber is dependent on the core size $\gamma = \frac{2\pi n_2}{\lambda A_{eff}} = 6.62 \times 10^{-4} \frac{\text{W}}{\text{m}}$, the values can be plugged into the following derivations for optimum pulse width and energy,³²

$$\Delta T_{i,opt} = 3g^{-\frac{2}{3}} \left(\frac{\gamma \beta_2}{2} \right)^{\frac{1}{3}} E_i^{\frac{1}{3}} \quad (2)$$

$$E_{i,opt} = \frac{2(\Delta T_i)^3 g^2}{27\gamma \beta_2} \quad (3)$$

By solving Equations 2 and 3 with the fiber design parameters, we find that the optimum pulse width is 315 fs, and the optimum pulse energy is 2 pJ. The real seed laser pulse width is significantly shorter ~ 80 fs, while the available energy is significantly larger ~ 2 nJ. We find that to overcome amplified spontaneous emission (ASE) noise in the fiber amplifier a much larger seed energy must be used (~ 625 pJ). Given the shorter than ideal pulse width,

a parabolic pulse evolution will still occur, however the pulse will take more time to reshape and achieve the asymptotic parabolic solution^{28,32}.

6.3.3 Optical Design

The primary optical design challenge for the fiber amplifier is the coupling of pump light into the gain fiber. The light exiting the pump fiber is within a core fiber diameter of 105 μm and must be coupled with minimal loss into the double clad gain fiber with first cladding diameter of 400 μm . If the pump light is not properly coupled into the cladding of the gain fiber, then damage can occur, especially when pumping with high powers ($\sim 1\text{W}$).

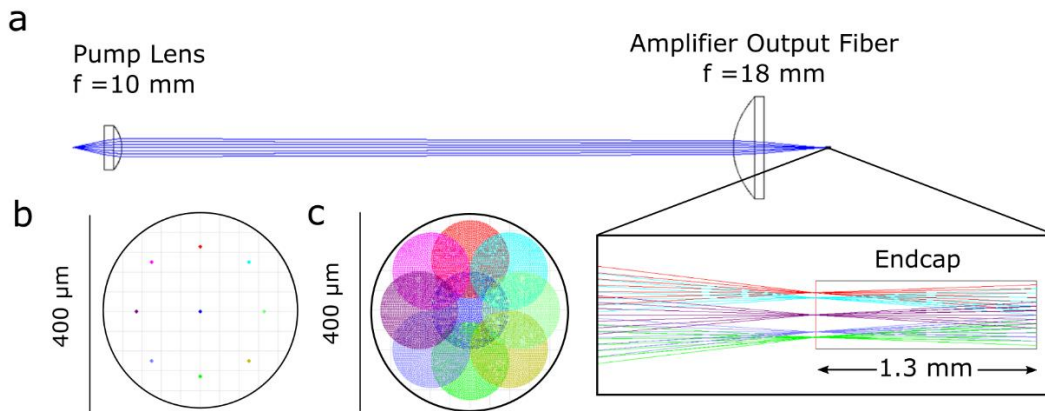


Figure 6.4 | Fiber amplifier pump coupling design

(a) Zemax 2D raytrace of the pump coupling optics (zoomed: view of pump light entering the fiber endcap (1.3 mm length)). (b) Full field spot diagram of the image from pump fiber endface projected onto the endcap face (c) Full field spot diagram of the image of the pump endface projected onto the face of the output gain fiber.

The design for the pump coupling optics was a slight magnification of the pump light onto the gain fiber through a two lens telescope assembly (Figure 6.4). First, the pump light is approximately collimated with a 10 mm focal length aspheric lens, then it is relayed onto the gain fiber over a distance of 150 mm. The second aspheric lens with focal length

18 mm is put one focal length before the pump fiber, for a total magnification of ~ 1.8 . From the zemax model, the encircled energy of the pump light from the 105 μm core is projected onto the gain fiber endface with diameter of $\sim 200 \mu\text{m}$. The geometric 200 μm spot size of the pump light on the gain fiber is expected based on the magnification of the coupling optics. With the 400 μm cladding size of the gain fiber, the coupling efficiency should be close to 100%, which is confirmed through experimental observation. When pumping at very high powers $>10\text{W}$ we notice no damage to the endface, or loss in beam quality from the gain fiber.

6.3.4 Characterization

The fiber amplifier pulse-width was measured using an *in situ* autocorrelation technique with a GaAsP photodiode³⁴. The benefit of *in situ*, over standalone, autocorrelation is that the exact pulse-width can be measured through the microscope objective used for imaging (25 \times , 1.0 NA, XLPN25XSVMP, Olympus). With this approach, the optimum pulse-width at the focal plane is achieved, despite travelling through a highly dispersive objective lens. The minimum pulse-width of the fiber amplifier at the focus of the objective was found to be 120 fs (**Figure 6.5**), although the pulse is affected by significant third order dispersion (TOD), as evidenced by the secondary peak ~ 200 fs from the central pulse. The high TOD is caused by a combination of the amplification fiber, objective lens, and pulse compression gratings. Without passing through the objective, it is possible to obtain a cleaner 120 fs pulse with no side lobes. Although the pulse distortion is not a significant limitation for this application, the use of shorter amplification fiber and prisms rather than gratings for compression would likely reduce the TOD significantly.

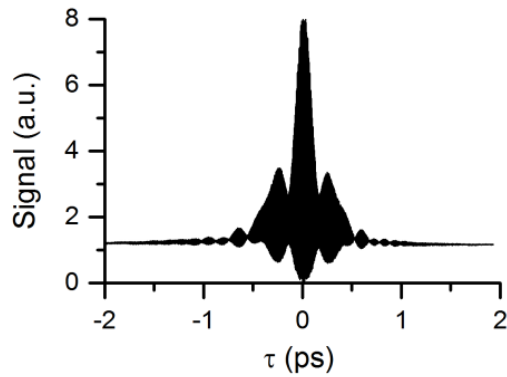


Figure 6.5 | Ytterbium fiber amplifier pulse-width

The beam quality of the fiber amplifier was characterized using a CMOS camera. The beam quality was found to be $M^2 = 1.19$ (**Figure 6.6**). Images of the focused beam were taken at different distances through the Rayleigh range of the focal spot.

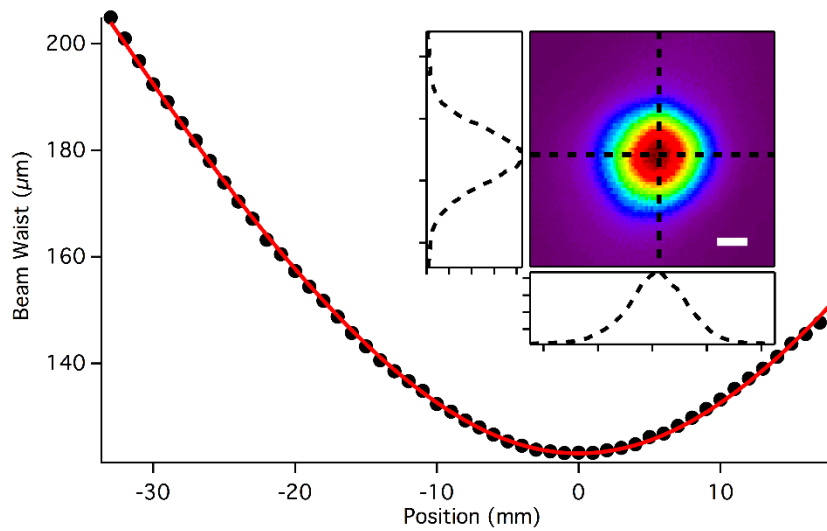


Figure 6.6 | Fiber amplifier beam quality

Fiber amplifier ($\lambda = 1055 \text{ nm}$) beam waist diameter versus focus position, using a 300 mm focal length spherical lens. The beam quality was measured to be an average of $M^2 = 1.19$, along x and y dimensions. Inset: spatial profile of the beam, the scale bar is $50 \mu\text{m}$.

The data was fitted to obtain the beam quality metric. The beam quality is significantly better than standard externally pumped Ti:S lasers (Mira 900, Coherent $M^2 = 2.7$), and comparable to single mode fiber emitters $M^2 = 1.1$.

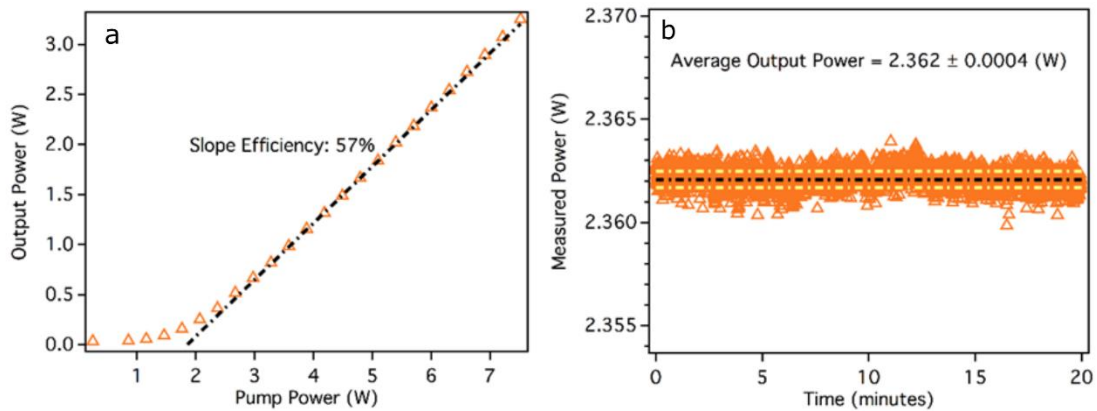


Figure 6.7 | Fiber Amplifier Pump Power Dependence and Stability

(a) Power dependence (b) Stability plot

The Fiber amplifier was characterized in terms of pump output power dependence on absorbed 976 nm pump power for a seed input power of 50 mW at 1050 nm (**Figure 6.7**). The amplification threshold is at 2 W of pump power. The average power output versus time (20 minutes) was also measured, and found to be better than 400 μ W stability ($\pm 1 \times 10^{-5}\%$).

6.4 DIAMOND RAMAN LASER

The diamond Raman laser is based on a ring cavity design according to previous embodiments^{23,25}, with two differences. First, the cavity has two additional fold mirrors to maintain a footprint of less than 1 m in length, due to space constraints. Second, the ytterbium fiber amplifier pump is unique to this embodiment, and to our knowledge, is the

first demonstration using femtosecond pumping centered at 1055 nm to achieve a first Stokes Raman output at 1240 nm.

6.4.1 Instrumentation

The pump light is expanded with a telescope lens pair ($M = 3$), and then focused ($f_l = 200$ mm) to achieve a mode-radius, $\omega_0 = 20$ μm , within the center of the diamond. The mirrors within the cavity are high reflectors ($R > 99.5\%$) at 1240 nm, except for the output coupler, which has a transmission of approximately 8% at 1240 nm. Two curved mirrors with radius of curvature 200 mm focus the light into the diamond crystal. A diamond (CVD-grown, 8 mm long, 1240 nm AR-coating) with $\langle 111 \rangle$ crystal axis aligned to the horizontal pump polarization generates the stimulated Raman gain. A cavity mirror mounted on a high precision flexure stage with integrated piezo drive (KPZNF5, Thorlabs) allows matching of the cavity round trip time to the repetition rate of the pump for optimal overlap between pump and Stokes pulses within the crystal. The Stokes pulses that exit the cavity through the output coupler have a slight chirp, 400 fs, from the dispersion introduced by the diamond in the cavity. Using a pair of prisms (P1 and P2, in **Figure 6.8**) the pulse width can be compressed down to 100 fs.

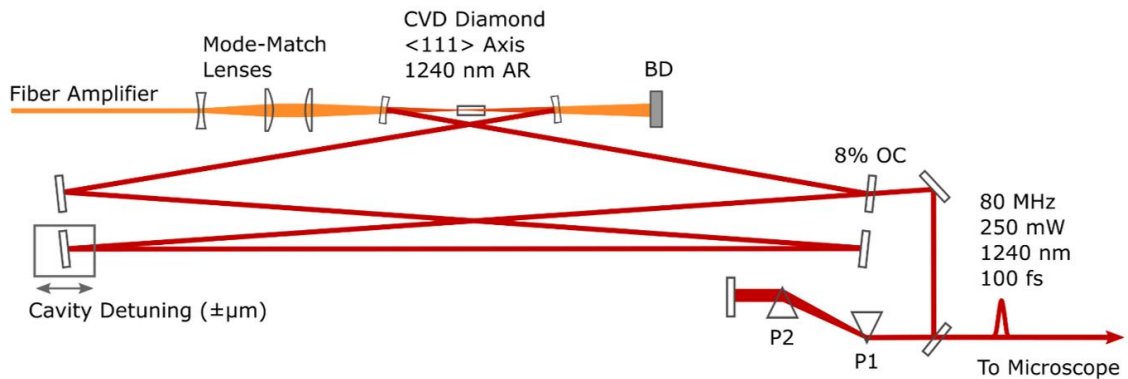


Figure 6.8 | Diamond Raman Laser Schematic

The diamond Raman laser consists of only 7 optical components: 1 CVD diamond, 3 fold mirrors, 2 curved mirrors, and 1 output coupler (**Table 6.2**). The most critical specifications for the components are reflection/Transmission or light at the pump wavelength (1040-1060nm) and the Stokes output (1230-1250 nm). The reflectivity of each component is outlined in Table 6.2.

Description	R @ 1240 nm	T @ 1050 nm	Supplier	Manufacturer's Part #	Price	Qty.
CVD Diamond 8x4x1 mm ³	<0.5%	-	Element 6	155-104-1456	\$5,000.00	1
Fold mirror	99.9%	-	Layertec	102023	\$469.00	3
Output Coupler (Rmax @1060 nm)	92%	<1%	CVI	-	\$700.00	1
Curved Mirror ROC=200 mm	99%	93%	ATF Films	-	\$800.00	2

Table 6.2 | Diamond Laser Optical Components

The total cost of the Diamond laser is extremely small, compared to OPOs with similar specs. However, one major limitation is that a high powered, and stable pump laser must be used for operation, which drives up the cost. Regardless, the total cost of both the diamond laser and fiber amplifier is ~\$50,000, which is an order of magnitude less than existing commercial OPO systems.

6.4.3 Mode Matching Design

To efficiently transfer energy from pump pulses into the diamond laser cavity, the focusing optics design must match the modes of the pump light to the cavity. Mode match analysis was performed by hand using Gaussian beam matrix approach, before moving into Zemax to refine the design. The physical optics propagation model of Gaussian beams was

used, due to the highly inaccurate results from a standard geometrical ray approach. The model used a telescope lens pair to increase the beam diameter of the pump light from 2 mm to ~6mm. A Galilean telescope was selected to avoid thermal effects from focusing the high-energy pump light, the lenses were $f = -50$ mm (ACN254-050-B, Thorlabs) and $f = 150$ mm (AC254-150-C-ML, Thorlabs), Both lenses were achromatic doublets to reduce chromatic error from the high bandwidth pump pulses (>30 nm). The spacing between the lenses was 124 mm. After the beam is expanded by the telescope pair, it is then focused using a single achromatic objective lens (AC254-200-C, Thorlabs) with focal length = 200 mm. The distance from the telescope pair to the objective is 40 mm, and the distance to the diamond from objective lens is 165 mm.

6.4.2 Characterization

Characterization of the diamond Raman laser was performed in the same way as the fiber amplifier, by measuring (1) spectrum (2) autocorrelation, and (3) efficiency and stability. The diamond Raman laser autocorrelation (**Figure 6.9c**) is both cleaner, and more compressed (100 fs) than the fiber amplifier, despite being pumped by the structured pulse from the fiber amplifier. The optimized Raman laser predominantly converts the long-wavelength components of the pump spectrum, with the central 1240 nm wavelength of the Stokes pulse corresponding to the longer-wavelength 1064 nm peak of the structured pump spectrum. This selective Raman conversion process along with self- and cross-phase modulation of the Stokes pulse itself results overall in a Stokes spectrum that is narrower than the 120 fs non-transform-limited pump pulse; however, the Stokes spectrum has less phase noise resulting in a shorter 100 fs Stokes pulse (**Figure 6.9d**), closer to its transform limit. We find that the fiber amplifier pulse-width affects the Raman conversion efficiency

and resulting output power. To achieve the shortestest 2C2P pulse, the fiber amplifier pulse-width was minimized at the objective focus, rather than at the focus of the diamond crystal.

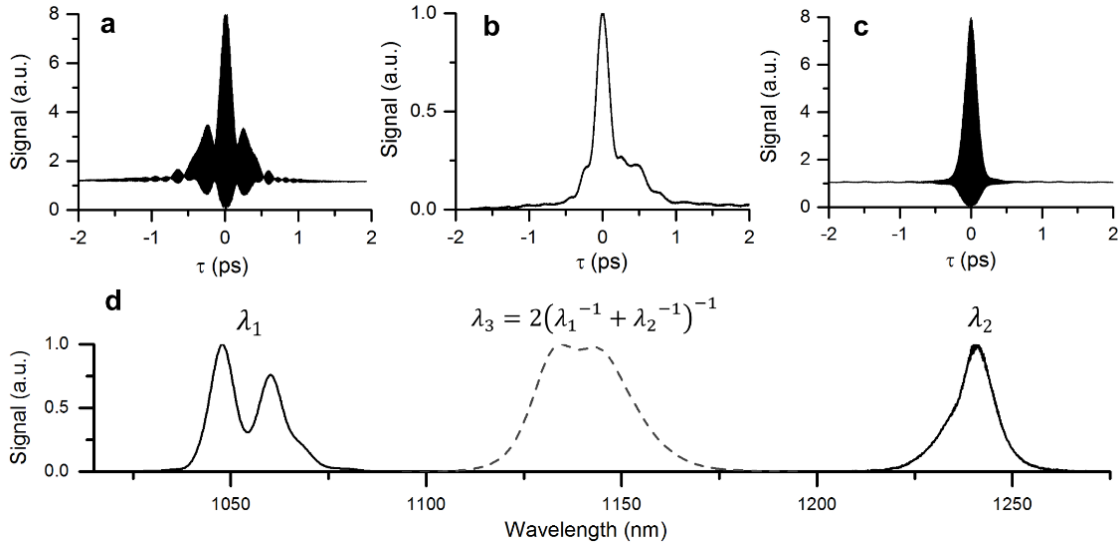


Figure 6.9 | Dual Output Laser Characterization

(a) Fiber amplifier autocorrelation (b) Cross-correlation (1055 nm and 1240 nm)
(c) Diamond laser autocorrelation (d) Fiber amplifier and diamond laser spectrum and correlation spectrum

In addition to autocorrelation of individual laser pulses, we perform cross-correlation between both lasers to evaluate the effective 2C2P pulse-width (**Figure 6.9b**). The resulting full-width-half-max (FWHM) pulse-width was measured to be 220 fs. As expected, the cross-correlation shows that the effective 2C2P pulse-width is roughly equal to the temporal overlap between both excitation pulse-widths. The asymmetrical effect of TOD on the pulse due to the contribution from the fiber amplifier can clearly be seen from the cross-correlation.

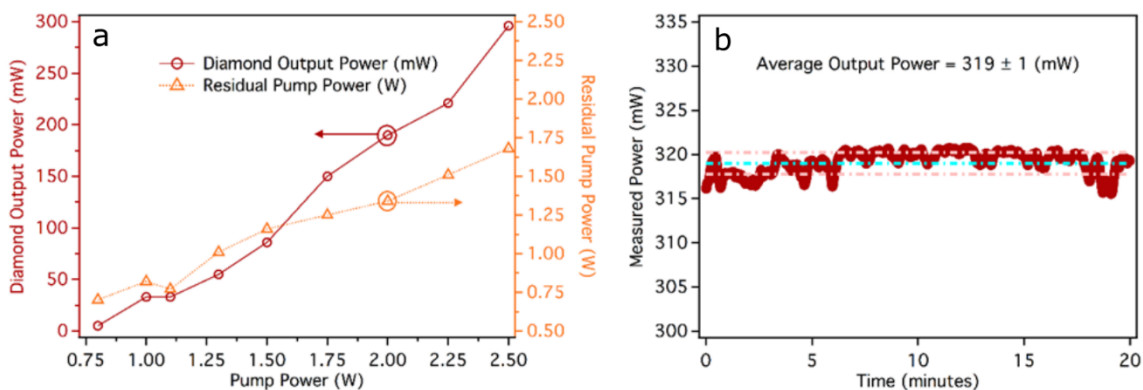


Figure 6.10 | Diamond Laser Pump Power Dependence and Stability
 (a) Output power versus absorbed pump power (b) stability over 20 minutes

The diamond laser was characterized in terms of efficiency in pump power and stability over the course of 20 minutes (**Figure 6.10**). From the output power versus pump power experiment it was found that the lasing threshold is 750 mW, which is in agreement with previous demonstrations of femtosecond diamond Raman lasers³⁵.

6.5 TWO-COLOR TWO-PHOTON EXCITATION MICROSCOPY

6.5.1 Dual output laser system

A custom-built upright microscope was used for imaging experiments to validate the dual output laser system (**Figure 6.11a**). The fiber amplifier was routed through a delay line before being combined with the diamond laser with a shortpass dichroic mirror. The delay line is mounted on a motorized stage to perform cross-correlation measurements, and allow synchronization of the pulses during imaging experiments. After the pulses are combined onto a single optical axis, they enter the custom-built microscope stage.

The brightness enhancement afforded by 2C2P is noticeable when the pulses are delayed by several hundred femtoseconds ($\tau = \pm 330$ fs) versus perfectly overlapped ($\tau = 0$ fs) in a cell expressing tdKatushka2 (**Figure 6.11b**). The modulation depth of the

brightness enhancement was quantified by recording the average signal in the image at varying pulse synchronization delays, τ (**Figure 6.11c**).

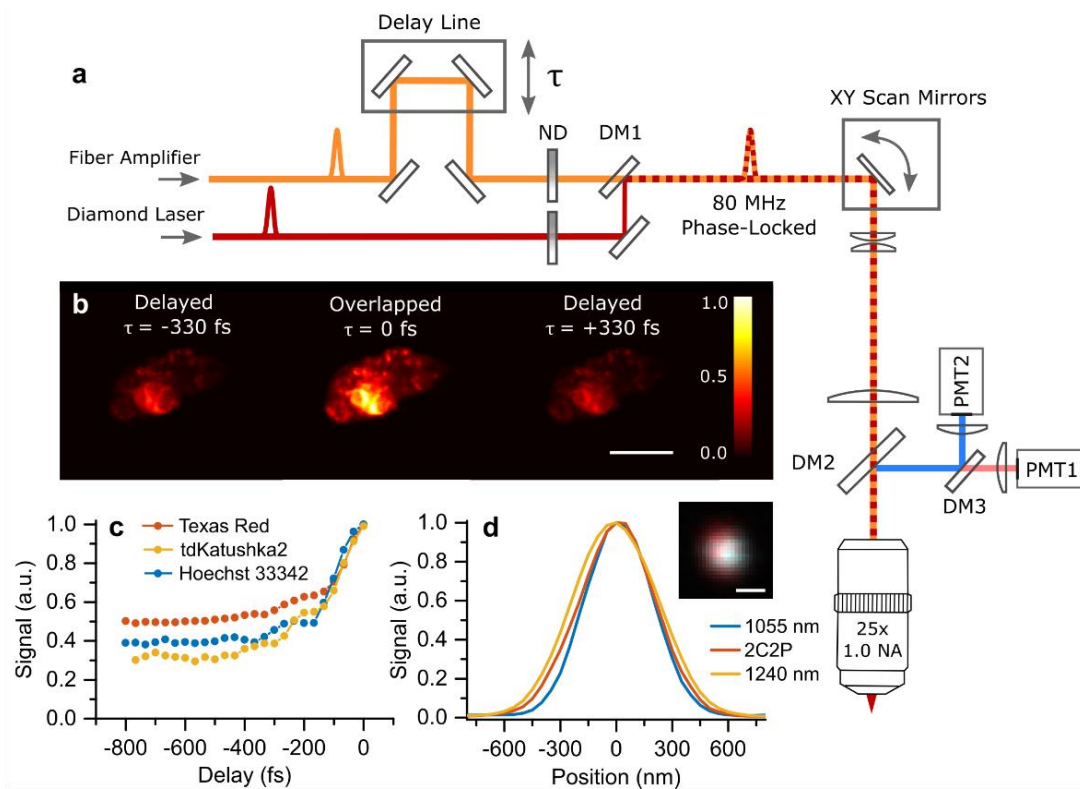


Figure 6.11 | Two-color Excitation Microscope

(a) Microscope schematic, the fiber amplifier is overlapped in time (τ) relative to the diamond Raman laser using a mirror delay line. Their ratio of excitation power is adjusted using independent neutral density filters (ND). Both pulses are sent into a custom-built two-photon upright microscope (b) 2C2P excitation demonstrated on a single cell expressing tdKatushka2-VASP-5 at various pulse synchronization delay times, scale bar is 10 μm . (c) 2C2P excitation as a function of delay time, τ , for various fluorescent labels. (d) The point spread function line profiles for 1055 nm, 1240 nm, and 2C2P excitation on 200 nm red fluorescent beads in agarose (inset: image of a single 200 nm bead with 1055 nm and 1240 nm excitation overlaid in blue and red respectively, scale bar is 500 nm). DM1 is a shortpass dichroic filter with edge at 1180 nm. DM2 and DM3 are longpass dichroic filters with edges at 775 nm, and 570 nm, respectively.

A large modulation depth can be achieved for fluorophores with a small direct excitation cross-section (one-color two-photon, 1C2P), but high 2C2P cross-section. For a fluorophore with zero excitation cross-section at either 1C2P wavelength and non-zero excitation efficiency with 2C2P, the modulation depth approaches unity.²⁰ In the case of the fluorophores used here, the modulation ranges from 0.7 for tdKatushka2, to 0.5 for Texas Red. Additionally, it is possible to tune the modulation depth by adjusting the ratio of excitation powers (**Figure 6.12**). The point spread function (PSF) of each excitation regime was measured using 200 nm fluorescent microspheres (F8810, ThermoFisher) embedded in agarose (**Figure 6.11d**). The FWHM PSF lateral size was found to be 528 nm, 602 nm, and 635 nm, for $\lambda=1055$ nm, 2C2P ($\lambda=1140$ nm), and $\lambda=1240$ nm, respectively.

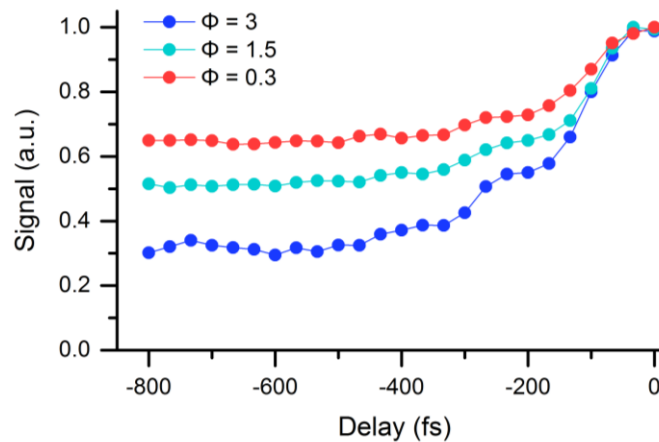


Figure 6.12 | Two-color Excitation Power Ratio

Fluorescence signal of tdKatushka2 versus pulse synchronization delay time under 2C2P excitation for differing levels of Φ . Where Φ is the ratio of average powers of 1240 nm and 1055 nm excitation. $\Phi > 1$, refers to higher 1240 nm average power. In this case of fluorophore and 2C excitation wavelength pair it is possible to adjust the signal modulation

depth from 35% to 70% for increasing values of Φ . With 1240 nm excitation, tdKatushka2 has a near zero cross section, whereas at 1055 nm the cross section is almost 50% of the peak, so there will always signal due to direct 1C2P excitation. Although the excitation efficiency is not increased with high values of Φ , the increased modulation depth could be beneficial for multicolor experiments requiring rapid signal modulation of 2C2P while still maintaining direct 1C2P excitation.

6.5.2 Two-color excitation efficiencies for common fluorophores

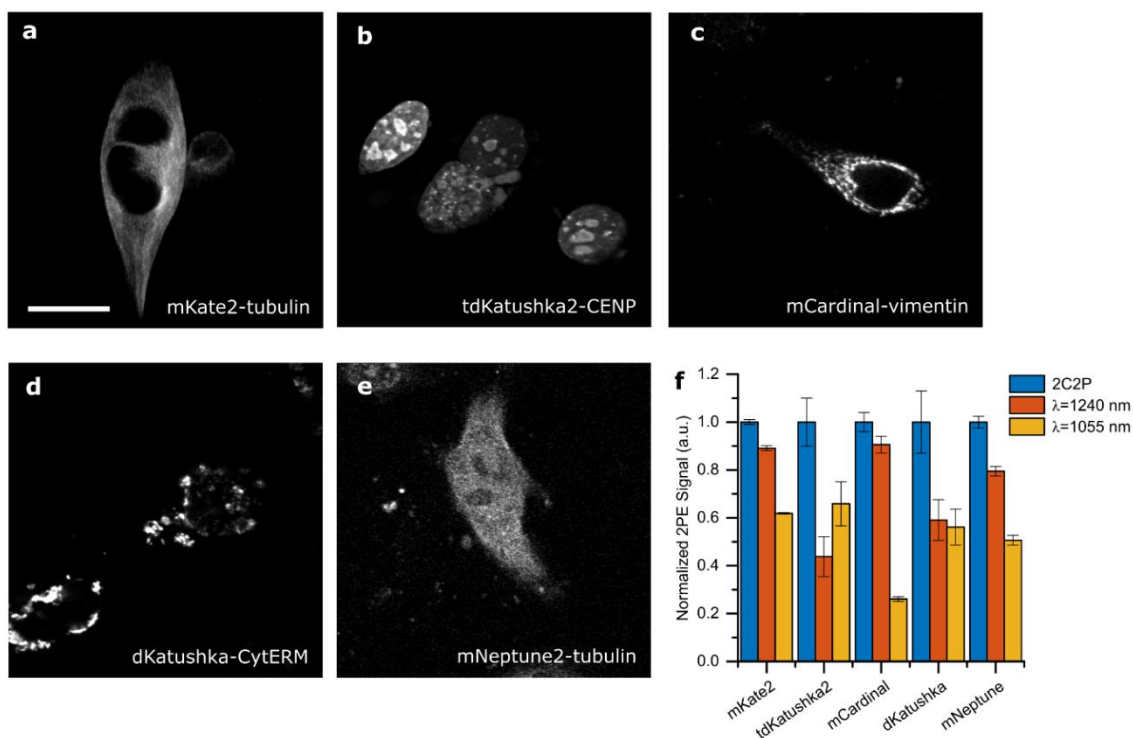


Figure 6.13 | Two-color excitation of far-red proteins

Two-color two-photon excitation images of HeLa cells transiently expressing mKate2-tubulin (FP185, Evrogen) (**Figure 6.13a**) tdKatushka2-CENPB-N-22¹⁰ (plasmid # 56033, Addgene), (**Figure 6.13b**) mCardinal-vimentin¹⁰ (plasmid # 56178, Addgene), (**Figure 6.13c**) dKatushka-cytERM (plasmid # 56027, Addgene), (**Figure 6.13d**) and

mNeptune2-tubulin (plasmid # 56150, Addgene) (**Figure 6.13e**). The scale bar is 7.5 μm . Comparison of detected fluorescence signal from the cell images in **a.-e.** under both 1C2P and 2C2P excitation (**Figure 6.13f**). The total power at the back aperture was kept constant with each excitation scheme, the PMT gain was the same for all conditions. The average power ranged from 4 mW to 16 mW depending on the brightness of the fluorophore and expression level in the cell. In all of the tested cells, 2C2P offers the highest signal level, on average 90% brighter than with 1C2P at $\lambda=1055$ nm. This brightness enhancement can be attributed to the higher 2P fluorescence cross section at the effective 2C2P wavelength of 1140 nm, compared with either of the 1C2P excitation wavelengths. The error bars are the standard deviation of the image signal.

6.6 TWO-COLOR MULTIPHOTON EXCITATION IMAGING

The following sections detail the experimental evaluation of the dual output Fiber pumped diamond Raman laser for use with multicolor excitation microscopy. Here we show that a newly discovered excitation regime, known as two-color three-photon, is possible. We also demonstrate very deep (>900 μm) imaging of vasculature in a mouse brain using two-color excitation. It is the first demonstration of two-color excitation *in vivo*, and the deepest demonstration of two-color excitation in any sample.

6.6.1 Two-color Three-photon Excitation of Spheroids

We evaluate 2C2P excitation by performing a multicolor imaging experiment in a spheroid of MCF-10A breast cancer cells. The spheroid, commonly used as a cancer tumor model, is a cluster of hundreds of cells arranged in 3D with dimensions of approximately $400 \times 400 \times 200$ μm^3 (See Chapter 3, **Figure 3.3**).

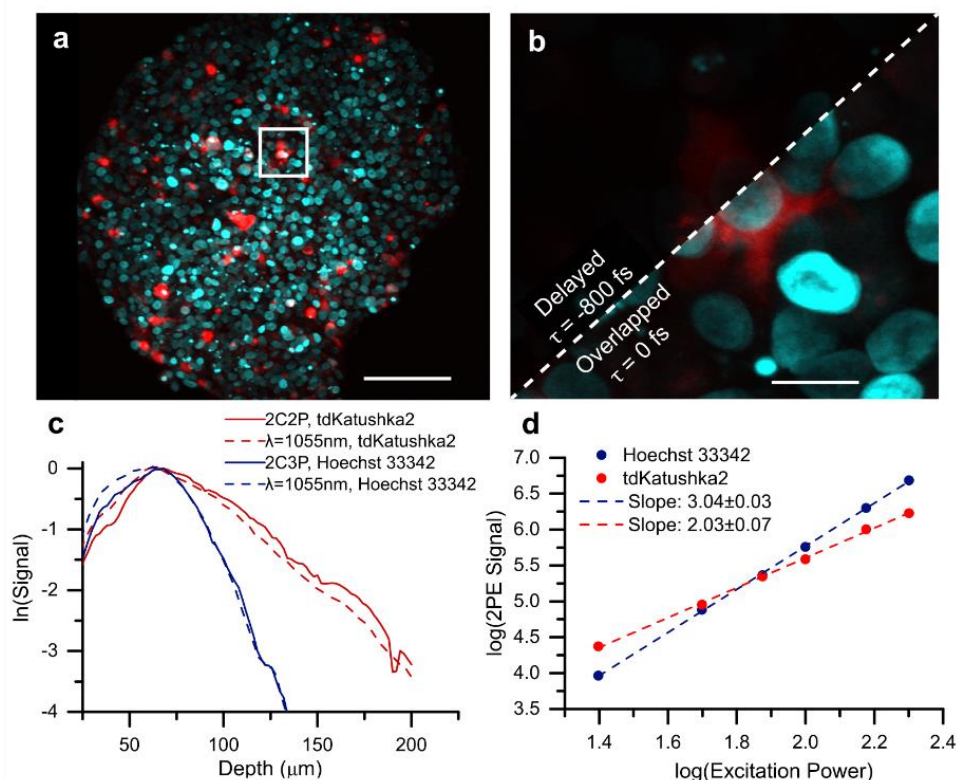


Figure 6.14 | Two-color three-photon excitation of spheroids

(a) Maximum intensity projection of a 200 μm thick spheroid with MCF-10A cells expressing tdKatushka2 (red) in vasodilator-stimulated phosphoprotein (VASP), and nuclei labelled with Hoechst 33342 (blue). Scale bar is 80 μm . (b) A 10 μm thick maximum intensity projection at 100 μm depth. The image is a zoom in of the white boxed region from panel (a) showing the effect of pulse synchronization on signal. The scale bar is 10 μm . (c) Mean image signal level versus depth for both color channels, tdKatushka2 (red), and Hoechst33342 (blue), and both excitation regimes, two-color excitation (solid line), and fiber amplifier only (dashed line). (d) Signal dependence versus excitation power for Hoechst 33342 (blue), and tdKatushka2 (red), using two-color excitation. tdKatushka2 undergoes two-photon excitation, while Hoechst33342 undergoes two-color three-photon excitation.

Multicolor imaging of two spectrally distinct labels is performed through transient expression of tdKatushka2 on the vasodilator-stimulated phosphoprotein (VASP) within the cytoplasm, and staining with Hoechst 33342 in the nucleus (**Figure 6.14a**). The effect of pulse delay can readily be seen (**Figure 6.14b**). 2C2P provides highly efficient excitation of tdKatushka2, a fluorescent protein with exceptional brightness $\sim 100 \text{ GM}^{11}$. Excitation

of tdKatushka2 is not easily accessible to standard Ti:S lasers due to its peak 2PE cross-section at 1100 nm. Even when compared with 1C2P excitation at 1055 nm, the 2C2P excitation has 40% higher signal level throughout the spheroid (**Figure 6.14c**). A number of other bright far-red fluorescent proteins are desirable for intravital microscopy, but cannot be efficiently excited by either ytterbium-based lasers or Ti:S lasers. Far-red fluorescent proteins such as mCardinal¹², mNeptune³⁶, and mKate2¹⁰, all have peak 2PE cross-sections within 10 nm of the effective 2C2P excitation wavelength of 1140 nm. For these recently developed far-red fluorescent proteins, 2C2P provides on average a 90% signal increase over 1C2P at 1055 nm (**Figure 6.13**).

Although this laser system is optimized for efficient excitation of far-red fluorophores, we also demonstrate that blue emitting fluorophores can be excited at these longer wavelengths through two-color three-photon excitation (2C3P). While 2C2P has been demonstrated as early as 1996,³⁷ and by several others,^{20,38} to our knowledge this is the first demonstration of 2C3P imaging. Using two-color excitation, the sample of Hoechst 33342 stained cells shows a power dependence (**Figure 6.14d**) with a slope of 3.04 ± 0.03 on a log-log scale, indicating a three-photon absorption process. We verify that this process is purely three-photon by performing the same experiment using only 1055 nm excitation, and also recover a slope of 3 (**Figure 6.15**). Direct (one-color) excitation accounts for approximately 40% of the signal from Hoechst 33342 (**Figure 6.11c**), so the remaining 60% of the signal can be inferred to be the product of 2C3P excitation. Two-color three-photon excitation has up to four discrete energy transitions, as opposed to three with 2C2P, and 2C3P offers an even more confined focus due to third-order dependence on excitation intensity³⁹. Considering these benefits, we predict potentially novel future applications of 2C3P.

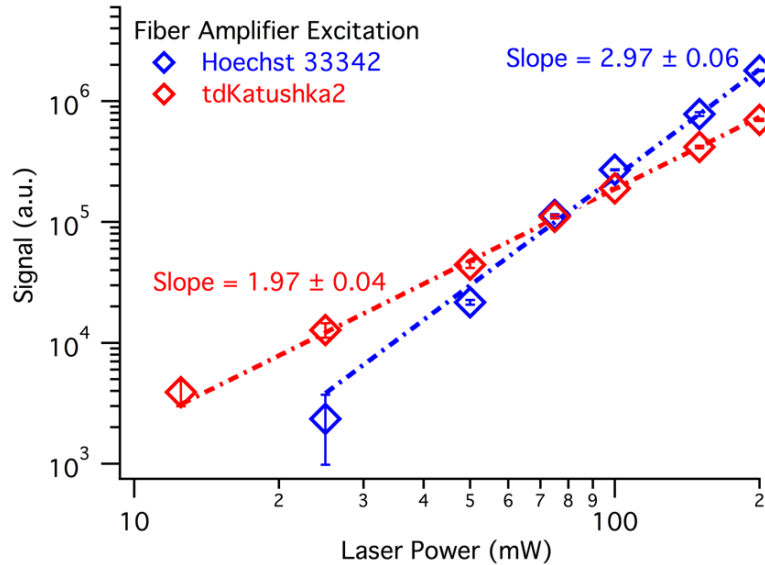


Figure 6.15 | Excitation dependency of tdKatushka2 and Hoechst 33342.

Log-log plot for tdKatushka2 and Hoechst33342 under 1055 nm excitation. The slope of tdKatushka2 is 1.97 indicating a two-photon process, while the slope for Hoechst is 2.97 indicating a three-photon process.

6.6.2 Deep Two-color Multiphoton Imaging in a Living Mouse Brain

Two-color two-photon microscopy is demonstrated *in vivo* with a series of stacks recorded in the same region in the brain of an adult live mouse, under three different excitation regimes (1) 2C2P $\tau=0$ fs, (2) 1C2P $\lambda=1055$ nm, and (3) 2C2P $\tau=600$ fs. The total excitation power at each plane was kept constant for each regime, with 20 mW for surface level imaging, and a maximum of 150 mW at depths beyond 400 μm . Texas Red is selected as a vasculature label for its high 2PE cross section at the 2C2P effective wavelength of 1140 nm. Verification that Texas Red is undergoing two-photon absorption was found through power dependence controls at both excitation wavelengths. The relative brightness of Texas Red is almost twice as high at 1140 nm compared to 1055 nm,⁴⁰ although it has not been characterized out to 1240 nm. With 2C2P overlapped pulses ($\tau=0$ fs) a depth of 960 μm was reached (**Figure 6.16a**). For the other two excitation regimes, a depth of only 800 μm can be achieved before the signal is too low to be detected.

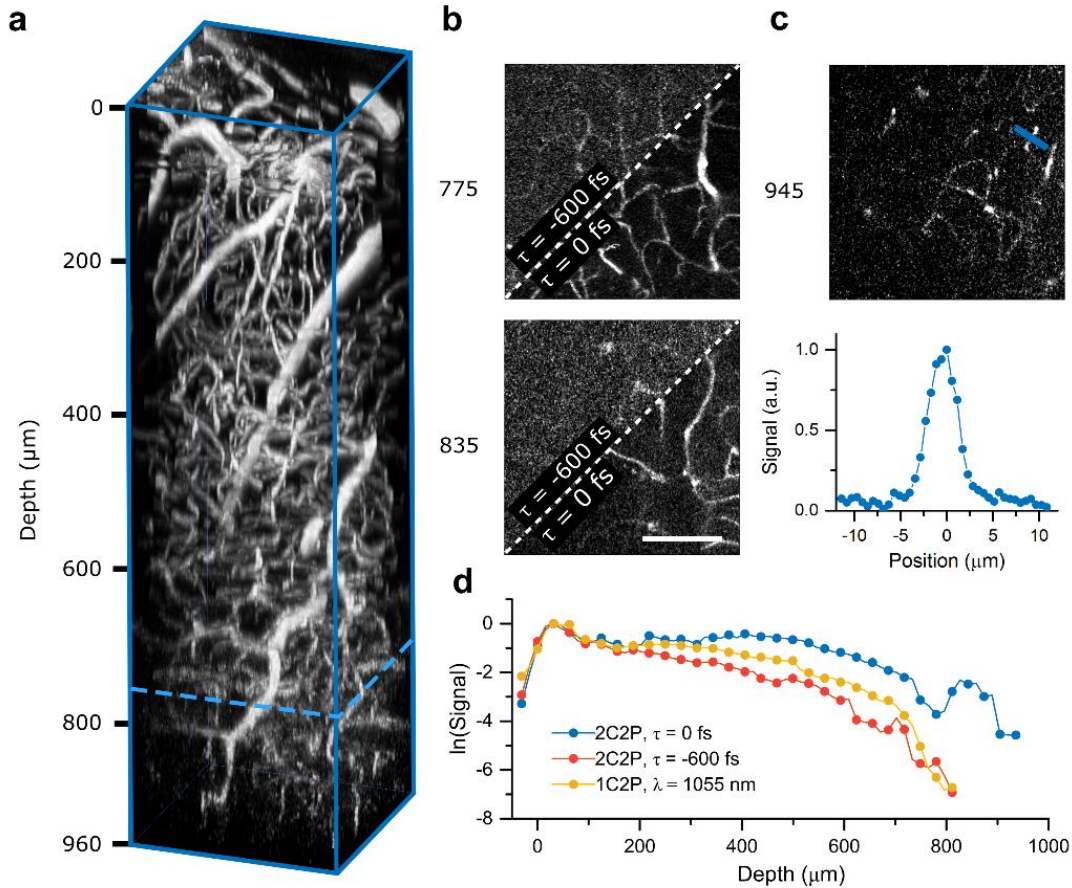


Figure 6.16 | Deep *in vivo* microscopy with two-color excitation.

(a) Three dimensional reconstruction of a vascular images taken with two-color two-photon excitation ($\lambda_1 = 1055$ nm, $\lambda_2 = 1240$ nm) in the brain of an adult mouse. The field of view is 300 μm and the stack depth is 960 μm . The dotted blue line is the approximate depth limit of 1C2P ($\lambda = 1055$ nm). (b) 2D plane maximum intensity projections of 20 μm thickness at 775 and 835 μm deep. The upper left section of each image shows the signal from 2C2P with pulses delayed $\tau = -600$ fs, while the bottom right section shows the signal acquired with overlapped pulses, $\tau = 0$ fs. (c) Maximum intensity projection of five images over a 20 μm thickness taken with overlapped 2C2P excitation at a mean depth of 945 μm . The blue line denotes the region where a line profile is displayed in the lower panel. The signal to background ratio calculated from the line profile is 17. (d) Natural logarithm of the mean signal level versus depth. Scale bar, 100 μm .

Incidentally, an imaging depth of $\sim 800 \mu\text{m}$ in the brain was previously reported by our group with Texas Red using a 1060 nm fiber oscillator.⁴¹ The effect of 2C2P allows for 20% deeper imaging than with the fiber amplifier alone, by virtue of the longer wavelength excitation, and better matched 2PE cross-section to Texas Red. To confirm that the improved signal is from 2C2P and not from direct 1240 nm excitation, a control stack was recorded with delayed pulses ($\tau = -600 \text{ fs}$). The effect of pulse delay dramatically reduces the signal-to-background ratio (SBR) and resulting image quality (**Figure 6.16b**). The SBR calculated using 2C2P ($\tau = 0 \text{ fs}$) at a depth of $945 \mu\text{m}$ was found to be 17 (**Figure 6.16c**), which is consistent with previous deep imaging demonstrations using longer wavelength excitation¹⁵. By quantifying the signal at each depth for all three excitation regimes, we find that 2C2P offers an average of $3\times$ more signal for images beyond $400 \mu\text{m}$ compared with the fiber amplifier alone (**Figure 6.16d**). However, the signal decay rate (slope = -0.006) is approximately the same for all three excitation regimes, implying that the fundamental imaging depth is not necessarily improved with 2C2P, just the signal level for a given excitation power.

Here we show that an imaging depth of nearly 1 mm can be achieved through 2C2P excitation of Texas Red in the cortical vasculature of a live mouse. The imaging depth with 2C2P is a 20% increase over using 1055 nm excitation alone. We also note that 1C2P excitation at 1055 nm is not fundamentally limited to shallower imaging depths, as we show that when matched with a better fluorophore, such as tdTomato, it is possible to image neural structure down to 1 mm in a live mouse brain (**Figure 6.17**).

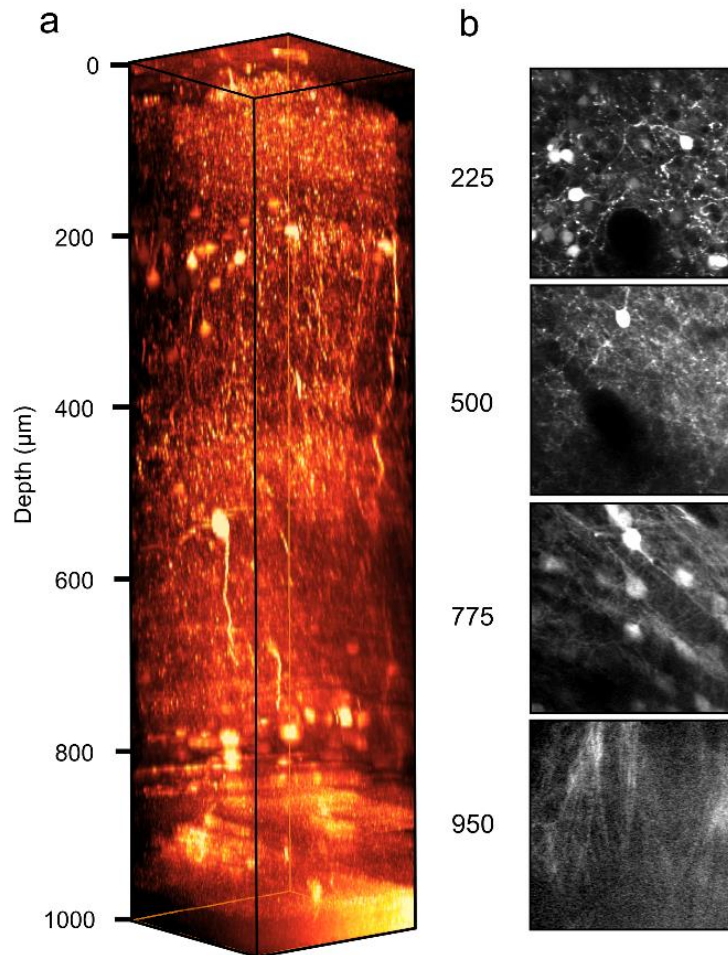


Figure 6.17 | Neuron *in vivo* images with Fiber Amplifier

a. *in vivo* stack in a live mouse using the fiber amplifier for 1C2P excitation ($\lambda=1055$ nm). Neurons are labelled with tdTomato through an adeno-associated virus injection. The injection causes local expression to all cell bodies within a region of the brain. **b.** Maximum intensity projection images of 10 μm thick slices at depths, 225 μm , 500 μm , 775 μm , and 950 μm , respectively.

The described dual output source allows for optimal excitation of most fluorophores over the range of 1000-1300 nm, making it a valuable tool for efficient multicolor imaging *in vivo*.

6.7 DISCUSSION

Two-color two-photon excitation is a relatively new approach for multicolor microscopy, as turnkey synchronized dual output sources have only become commercially available within the past few years. Yet, currently these dual output sources are hardly attainable for the typical biological imaging laboratory, primarily due to their cost and limited availability. For this reason, very few reports have detailed any form of 2C2P tissue microscopy. While a few reports have focused on the photophysical properties of 2C2P^{37,38}, and one demonstrates 2C2P with fluorescence lifetime imaging⁴², only one group has explored its use for multicolor imaging in tissue samples²⁰. In this report, we show that 2C2P with a diamond Raman laser is not only feasible for *in vivo* microscopy, but is often advantageous when compared with 1C2P. We demonstrate a 90% increase in signal for many common far-red fluorescent proteins, and 20% deeper imaging with Texas Red when compared with 1C2P excitation at 1055 nm.

Other than commercial laser sources for *in vivo* microscopy, several custom solutions have been developed by others. An output of 1250 nm was achieved by nonlinear generation in fiber with a 1070 nm seed⁴³. A Cr:forsterite laser tunable over 1220-1270 nm has also been used for harmonic generation microscopy⁴⁴. However, these approaches have significant limitations. For nonlinear generation in fiber, the pulse energy was limited to only 0.6 nJ which is not sufficient for *in vivo* applications. Furthermore, the nonlinear generation process is highly inefficient, making it difficult to use the seed laser as a second output for 2C2P. Cr:forsterite lasers suffer from alignment and implementation challenges because of their relatively complicated cavity and requirement for active cooling. Furthermore, they are not compatible with 2C2P, due to continuous wave pumping.

While it is clear that in the past two decades there has been no robust or cost effective means for generating two synchronized outputs needed to perform 2C2P, there are still a number of studies investigating the potential benefits of the approach. Several theoretical investigations have proposed 2C2P as a means to achieve superresolution^{45,46}, or to reduce background noise⁴⁷⁻⁴⁹. With the described laser system, some of these theorized studies could be experimentally verified. Additionally, with 2C3P excitation described herein, it could be possible to achieve enhanced results because of the higher order dependence on excitation intensity. Based on the simplicity of the fiber pumped diamond Raman laser design, we see no challenge for other groups to adopt this as a robust platform for development of 2C2P or 2C3P applications.

The results demonstrate that *in vivo* imaging is possible even with a relatively low power of 150 mW at depth. With the current level of excitation power, the images at depth are most likely power limited rather than limited by tissue scattering. When going beyond 960 μm the signal falls off dramatically, whereas the background remains relatively constant. However, there is no fundamental issue with scaling the output power of the diamond Raman laser up to Watt levels^{23,25}. Increasing pump power has the added advantage of increased nonlinearity in the diamond, which broadens the Raman output spectrum, resulting in an even more compressible pulse. With additional dispersion compensating elements in the cavity it is possible to reach 25 fs pulse-widths from a diamond Raman laser⁵⁰.

Many far-red dyes compatible with deep *in vivo* microscopy of vasculature have been characterized for peak 2PE cross-sections between 1200-1300 nm,²⁶ whereas most far-red fluorescent proteins compatible with neuron labelling have a peak 2PE cross-section in the range of 1000-1150 nm¹¹. When using a single output laser source, even a tunable one, there will always be a tradeoff in excitation efficiency between multicolor

labels, which in turn restricts the fundamental imaging depth with either, or both labels. Whereas, 2C2P with the fiber amplifier pumped diamond Raman laser allows for highly efficient excitation of both vascular and neural labelling strategies, through its near complete coverage of the 1000-1300 nm excitation range. At \$50,000 for all components, the cost of the system is an order of magnitude less than commercial dual output lasers, and nearly half that of a typical Ti:S laser. We expect the fiber pumped diamond Raman laser to be a highly desirable alternative to the OPO for simultaneous multicolor imaging *in vivo*. Additionally, this dual output laser system is a critical enabling tool to explore the future possibilities of 2C2P and 2C3P excitation microscopy.

6.8 REFERENCES

1. Zipfel, W. R., Williams, R. M. & Webb, W. W. Nonlinear magic: multiphoton microscopy in the biosciences. *Nat. Biotechnol.* **21**, 1369–77 (2003).
2. Helmchen, F. & Denk, W. Deep tissue two-photon microscopy. *Nat. Methods* **2**, 932–40 (2005).
3. Stosiek, C., Garaschuk, O., Holthoff, K. & Konnerth, A. In vivo two-photon calcium imaging of neuronal networks. *Proc. Natl. Acad. Sci. U. S. A.* **100**, 7319–24 (2003).
4. Tischbirek, C., Birkner, A., Jia, H., Sakmann, B. & Konnerth, A. Deep two-photon brain imaging with a red-shifted fluorometric Ca²⁺ indicator. *Proc. Natl. Acad. Sci. U. S. A.* **112**, 1–6 (2015).
5. Dana, H. *et al.* Sensitive red protein calcium indicators for imaging neural activity. *Elife* **5**, 1–24 (2016).
6. Sakadžić, S. *et al.* Two-photon high-resolution measurement of partial pressure of oxygen in cerebral vasculature and tissue. *Nat. Methods* **7**, 755–9 (2010).
7. Lecoq, J. *et al.* Simultaneous two-photon imaging of oxygen and blood flow in deep cerebral vessels. *Nat. Med.* **17**, 893–8 (2011).
8. Kazmi, S. M. S. *et al.* Three-dimensional mapping of oxygen tension in cortical arterioles before and after occlusion. *Biomed. Opt. Express* **4**, 1061–73 (2013).
9. Prakash, R. *et al.* Two-photon optogenetic toolbox for fast inhibition, excitation and bistable modulation. *Nat. Methods* **9**, 1171–9 (2012).
10. Shcherbo, D. *et al.* Far-red fluorescent tags for protein imaging in living tissues. *Biochem. J.* **418**, 567–574 (2009).
11. Drobizhev, M., Makarov, N. S., Tillo, S. E., Hughes, T. E. & Rebane, A. Two-photon absorption properties of fluorescent proteins. *Nat. Methods* **8**, 393–399 (2011).

12. Chu, J. *et al.* Non-invasive intravital imaging of cellular differentiation with a bright red-excitable fluorescent protein. *Nat. Methods* **11**, 572–8 (2014).
13. Dunn, A. K., Wallace, V. P., Coleno, M., Berns, M. W. & Tromberg, B. J. Influence of optical properties on two-photon fluorescence imaging in turbid samples. *Appl. Opt.* **39**, 1194–1201 (2000).
14. Oheim, M., Beaurepaire, E., Chaigneau, E., Mertz, J. & Charpak, S. Two-photon microscopy in brain tissue: parameters influencing the imaging depth. *J. Neurosci. Methods* **111**, 29–37 (2001).
15. Kobat, D., Horton, N. G. & Xu, C. In vivo two-photon microscopy to 1.6-mm depth in mouse cortex. *J. Biomed. Opt.* **16**, 106014 (2011).
16. Horton, N. G. *et al.* In vivo three-photon microscopy of subcortical structures within an intact mouse brain. **7**, 205–209 (2013).
17. Entenberg, D. *et al.* Setup and use of a two-laser multiphoton microscope for multichannel intravital fluorescence imaging. *Nat. Protoc.* **6**, 1500–20 (2011).
18. Yokoyama, H. *et al.* Two-photon bioimaging utilizing supercontinuum light generated by a high-peak-power picosecond semiconductor laser source. *J. Biomed. Opt.* **12**, 54019 (2007).
19. Brenner, M. H., Cai, D., Swanson, J. A. & Ogilvie, J. P. Two-photon imaging of multiple fluorescent proteins by phase-shaping and linear unmixing with a single broadband laser. *Opt. Express* **21**, 17256–64 (2013).
20. Mahou, P. *et al.* Multicolor two-photon tissue imaging by wavelength mixing. *Nat. Methods* **9**, 815–818 (2012).
21. Mahou, P., Vermot, J., Beaurepaire, E. & Supatto, W. Multicolor two-photon light-sheet microscopy. *Nat. Methods* **11**, 600–601 (2014).
22. Spence, D. J., Granados, E. & Mildren, R. P. Mode-locked picosecond diamond Raman laser. *Opt. Lett.* **35**, 556–558 (2010).
23. Murtagh, M., Lin, J., Mildren, R. P., McConnell, G. & Spence, D. J. Efficient diamond Raman laser generating 65 fs pulses. *Opt. Express* **23**, 15504–15513 (2015).
24. Trägårdh, J. *et al.* Two-Color, Two-Photon Imaging at Long Excitation Wavelengths Using a Diamond Raman Laser. *Microsc. Microanal.* 1–5 (2016).
25. Warrior, A. M. *et al.* Highly efficient picosecond diamond Raman laser at 1240 and 1485 nm. *Opt. Express* **22**, 3325–3333 (2014).
26. Kobat, D. *et al.* Deep tissue multiphoton microscopy using longer wavelength excitation. *Opt. Express* **17**, 13354–64 (2009).
27. Kruglov, V. I., Peacock, A. C., Harvey, J. D. & Dudley, J. M. Self-similar propagation of parabolic pulses in normal-dispersion fiber amplifiers. *J. Opt. Soc. Am. B* **19**, 461–469 (2002).
28. Dudley, J. M., Finot, C., Richardson, D. J. & Millot, G. Self-similarity in ultrafast nonlinear optics. *Nat. Phys.* **3**, 597–603 (2007).
29. Limpert, J. *et al.* High-power femtosecond Yb-doped fiber amplifier. *Opt. Express* **10**, 628–38 (2002).
30. Papadopoulos, D. N. *et al.* Generation of 63 fs 4.1 MW peak power pulses from a

- parabolic fiber amplifier operated beyond the gain bandwidth limit. *Opt. Lett.* **32**, 2520–2522 (2007).
31. Deng, Y., Chien, C.-Y., Fidric, B. G. & Kafka, J. D. Generation of sub-50 fs pulses from a high-power Yb-doped fiber amplifier. *Opt. Lett.* **34**, 3469–3471 (2009).
 32. Kruglov, V. I., Peacock, A. C., Harvey, J. D. & Dudley, J. M. Self-similar propagation of parabolic pulses in normal-dispersion fiber amplifiers. *J. Opt. Soc. Am. B* **19**, 461–469 (2002).
 33. Limpert, J. *et al.* High-power femtosecond Yb-doped fiber amplifier. *Opt. Express* **10**, 628–38 (2002).
 34. Millard, A. C., Fittinghoff, D. N., Squier, J. A., Müller, M. & Gaeta, A. L. Using GaAsP photodiodes to characterize ultrashort pulses under high numerical aperture focusing in microscopy. *J. Microsc.* **193**, 179–181 (1999).
 35. Murtagh, M., Lin, J., Mildren, R. P., McConnell, G. & Spence, D. J. Efficient diamond Raman laser generating 65 fs pulses. *Opt. Express* **23**, 15504–15513 (2015).
 36. Lin, M. Z. *et al.* Autofluorescent Proteins with Excitation in the Optical Window for Intravital Imaging in Mammals. *Chem. Biol.* **16**, 1169–1179 (2009).
 37. Lakowicz, J. R., Gryczynski, I., Malak, H. & Gryczynski, Z. Two-Color Two-Photon Excitation of Fluorescence. *Photochem. Photobiol.* **64**, 632–635 (1996).
 38. Quentmeier, S., Denicke, S., Ehlers, J.-E., Niesner, R. A. & Gericke, K.-H. Two-Color Two-Photon Excitation Using Femtosecond Laser Pulses. *J. Phys. Chem. B* **112**, 5768–5773 (2008).
 39. Hell, S. W. *et al.* Three-photon excitation in fluorescence microscopy. *J. Biomed. Opt.* **1**, 71–74 (1996).
 40. Bestvater, F. *et al.* Two-photon fluorescence absorption and emission spectra of dyes relevant for cell imaging. *J. Microsc.* **208**, 108–15 (2002).
 41. Perillo, E. P. *et al.* Deep in vivo two-photon microscopy with a low cost custom built mode-locked 1060 nm fiber laser. *Biomed. Opt. Express* **7**, 324 (2016).
 42. Robinson, T. *et al.* Analysis of DNA binding and nucleotide flipping kinetics using two-color two-photon fluorescence lifetime imaging microscopy. *Anal. Chem.* **86**, 10732–10740 (2014).
 43. Domingue, S. R. & Bartels, R. A. Three-photon excitation source at 1250 nm generated in a dual zero dispersion wavelength nonlinear fiber. *Opt. Express* **22**, 30777 (2014).
 44. Sun, C.-K. *et al.* Higher harmonic generation microscopy for developmental biology. *J. Struct. Biol.* **147**, 19–30 (2004).
 45. Hell, S. W. Improvement of lateral resolution in far-field fluorescence light microscopy by using two-photon excitation with offset beams. *Opt. Commun.* **106**, 19–24 (1994).
 46. Xiao, F., Wang, G. & Xu, Z. Superresolution in two-color excitation fluorescence microscopy. *Opt. Commun.* **228**, 225–230 (2003).
 47. Cambaliza, M. O. & Saloma, C. Advantages of two-color excitation fluorescence microscopy with two confocal excitation beams. *Opt. Commun.* **184**, 25–35

- (2000).
48. Blanca, C. M. & Saloma, C. Two-color excitation fluorescence microscopy through highly scattering media. *Appl. Opt.* **40**, 2722 (2001).
 49. Wang, C., Qiao, L., Mao, Z., Cheng, Y. & Xu, Z. Reduced deep-tissue image degradation in three-dimensional multiphoton microscopy with concentric two-color two-photon fluorescence excitation. *J. Opt. Soc. Am. B* **25**, 976 (2008).
 50. Lin, J. & Spence, D. J. 25.5 fs dissipative soliton diamond Raman laser. *Opt. Lett.* **41**, 1861–4 (2016).

Chapter 7: Conclusion

7.1 SUMMARY

Here I detail the progress made towards using nonlinear excitation methods to study biological specimen. The great utility of two-photon excitation is that it can be used to study a wide range of time and length scales relevant for biology, from mapping of the entire brain of a mouse¹, to study of the transit of a single EGF molecule through a cell². The novel particle tracking microscope technique (coined TSUNAMI), that I discussed (Chapters 2-4) is one such example of how two-photon excitation can be used to study biology at the extremely small (30 nm) length and fast (50 μ s) time scales necessary to uncover biology at the single particle level. I demonstrate that with advanced lasers such as the ytterbium fiber oscillator (Chapter 5), the ytterbium fiber amplifier, and diamond Raman laser (Chapter 6), that nonlinear microscopy can be utilized to great benefit for deep in vivo imaging of living mouse brain. Specifically, the dual output system detailed in Chapter 6 uses long wavelength excitation (1050 nm, 1240 nm) while still maintaining compatibility with dyes and proteins used in biology and neuroscience communities. The primary goal of this work is towards advancing nonlinear microscopy in the areas of biology and neuroscience. The detailed designs for all microscopes, lasers, and systems described herein provides a unique toolset for researchers wishing to employ nonlinear microscopy techniques to study biology in thick scattering samples.

7.1.1 Single Particle Tracking with Nonlinear Excitation

The novel technique known as, Tracking Single-particles Using Nonlinear And Multiplexed Illumination (TSUNAMI) allows for ultra-high resolution (30 nm, 50 μ s) study of single particles in thick biological samples. It offers a perfect case study in the power of nonlinear excitation. As the resolution is more than four orders of magnitude

smaller than the usable working depth of the technique, no other imaging method can offer this immense dynamic range of length scale (OCT offers only 1:1000 resolution vs depth ratio). Besides the use of nonlinear excitation, the other major driving principle of TSUNAMI, and other SPT techniques, is that we achieve ultra high resolution in time and space, at the expense of a single particle field-of-view. This drawback is a common theme in imaging techniques. No method has the capability to achieve high resolution, fast imaging, large field-of-view, and penetration depth all simultaneously. In **Chapter 2**, I detail the instrumentation and characterization, and demonstrate the various utilities of the method, such as, simultaneous lifetime measurement, tracking through 200 μm of scattering material, and post processing trajectories for higher time resolution. **Chapter 3** discusses the current applications for TSUNAMI in tracking endothelial growth factor receptors through cells and tumor models^{3,4}. Additionally, I discuss the progress made towards post-processing of these biological single-particle trajectories to classify the various modes of transport⁵. In Chapter 4, I discuss the current progress made towards improving and expanding the technique. Notably, I discuss the improved localization algorithm built upon maximum likelihood estimation (MLE) which achieves 1.7 times better axial localization compared to the traditional error signal approach⁶. Clearly, TSUNAMI is a powerful tool for nanometric investigation of living cells, and has already shown utility in several biological applications. I expect there will be many more applications and future work using TSUNAMI for nano-scale particle tracking in thick samples.

7.1.2 Near-Infrared Lasers for Nonlinear Microscopy

In this work I show that Fiber based oscillators and amplifiers offer compelling benefits over the Titanium Sapphire (Ti:S) lasers traditionally used for two-photon

microscopy. As described in **Chapter 5**, ytterbium fiber oscillators offer longer wavelength (1000-1100 nm) excitation without the need for active cooling, and can be built at the 1/10th the cost of a commercial Ti:S laser system. I demonstrate that a \$13,000, entirely homebuilt ytterbium fiber laser can be used for routine two-photon microscopy *in vivo*⁷. I demonstrate deep *in vivo* imaging to ~900 μm in a live mouse brain with the homebuilt laser. Furthermore, I compare the fiber laser emitting at 1060 nm to a commercial Ti:S laser tuned to 920 nm for imaging of yellow fluorescent protein (YFP) labelled neurons in a live mouse brain, and show that the Ti:S laser can reach 20% deeper into the brain, and visualize often hard to reach layer V neurons.

Building upon the homebuilt laser work, in **Chapter 6** I detail a homebuilt fiber amplifier pumped diamond Raman laser, which generates a dual output at 1055 nm and 1240 nm. I show that the homebuilt dual output source can be used for two-color two-photon (2C2P) microscopy by spatiotemporally overlapping their illumination at the focus (the first demonstration for a homebuilt system). Furthermore, I show, for the first time, the existence of a two-color three-photon (2C3P) excitation process. The 2C3P was performed on the UV dye Hoechst 33342 stained in a tumor model. The benefits of a such a dual output laser system are the large excitation range (1000-1300) without the need for tuning wavelength. The system offers a unique alternative to OPOs at a fraction of the cost, and can be reproduced without great effort by biological and neuroscience groups.

7.2 FUTURE DIRECTIONS

The wide array of nonlinear microscopy tools outlined in this work highlight the flexibility of nonlinear excitation in general. Some potential future directions are discussed, which I feel have the most impact to potentially uncover biological processes, or help aid medical research.

7.2.1 Combined Superresolution and 3D Tracking

As mentioned in **Chapter 4**, combining superresolution with TSUNAMI particle tracking has the potential to improve knowledge of how target molecules interact within the surrounding environment of the cell. The chosen superresolution method, single wavelength 2P STimulated Emission Depletion (STED) microscopy⁸, is relatively easy to implement. However, currently the challenge is to develop robust labelling strategies for live cells with compatible dyes (Atto647N, Atto633, SiR). Paul Selvin's SLO technique⁹ offers a promising route to intracellular labelling with the aforementioned dyes. The current challenge present with this project highlights the need to advance labelling strategies along with improvements in the optical tools for microscopy.

A combined STED-TSUNAMI system would allow for co-registration of single particle trajectories to sub-diffraction limited cell structure, such as actin, or tubulin. The 80 nm resolution of STED could allow for more accurate mapping of the cellular structure than is currently possible with diffraction limited imaging techniques¹⁰.

7.2.2 Dual Particle Tracking Microscopy

Modifying TSUNAMI to detect multiple spectral channels is a straightforward extension of the current work. However, the ability to detect two particles within the PSF offers dramatically more information about the targets than traditional SPT that could be used to study new and exciting problems in biology. For example, dual particle tracking could be used to study interactions between two targets, conformation changes in a dual labelled complex, rotational of a complex, or coincidence between a target and its surrounding environment. In Chapter 4, I highlight one such example of dual particle tracking to study binding distance between a doubly labelled DNA strand. The dual particle tracking approach for TSUNAMI offers many promising applications and future directions.

7.2.3 Tunable Long Wavelength lasers for Deep Imaging

Currently, the fiber pumped diamond Raman laser system offers coverage of the 1000-1300 nm wavelength range, and penetration depth up to 1 mm deep into live mouse brain. Improvements to this could be made in two areas, (1) deeper imaging with long wavelength, and (2) access to more dyes and proteins with different excitation wavelengths. The two areas of improvement are tied together, as longer wavelengths offer more access to common dyes through three-photon excitation. Around 1300-1400 nm many common fluorescent dyes and proteins switch from 2P to 3P excitation, and many of the green and orange emitting proteins that were not excitable at 1200 nm with 2P are able to be excited at ~1400 by 3P excitation. With a proper source, such as an optical parametric generator (OPG) which emits between 1300-1600 nm¹¹, it should be possible to create a dual output fiber amplifier pumped OPG which can access any common fluorescent protein used in neuroscience, while still maintain compatibility with deep in vivo microscopy through long wavelength excitation and high peak power (~100 kW). The ideal source although tunable from 1300-1600 nm could excite nearly any dye through wavelength mixing of the 1055 nm fiber amplifier excitation. For example if the source is tuned to 1400 nm, the 2P wavelengths are (1055 nm, 1200 nm, and 1400 nm), and the 3P wavelengths are (1055 nm, 1150 nm, 1260 nm, and 1400 nm), this system could offer nearly complete coverage of a 400 nm range without any need for tuning wavelength.

7.3 REFERENCES

1. Tsai, P. S. *et al.* Ultra-large field-of-view two-photon microscopy. *Opt. Express* **23**, 1825–1829 (2015).
2. Perillo, E. P. *et al.* Deep and high-resolution three-dimensional tracking of single particles using nonlinear and multiplexed illumination. *Nat. Commun.* **6**, 7874 (2015).
3. Perillo, E., Liu, Y.-L., Liu, C., Yeh, H.-C. & Dunn, A. K. Single particle tracking through highly scattering media with multiplexed two-photon excitation. *SPIE*

- BiOS* **9331**, 933107 (2015).
4. Perillo, E. P. *et al.* Deep and high-resolution three-dimensional tracking of single particles using nonlinear and multiplexed illumination. *Nat. Commun.* **6**, 7874 (2015).
 5. Liu, Y. *et al.* Segmentation of 3D Trajectories Acquired by TSUNAMI Microscope : An Application to EGFR Trafficking. *Biophysj* **111**, 2214–2227 (2016).
 6. Liu, C. *et al.* Improving z-tracking accuracy in the two-photon single-particle tracking microscope. *Appl. Phys. Lett.* **107**, 153701 (2015).
 7. Perillo, E. P. *et al.* Deep in vivo two-photon microscopy with a low cost custom built mode-locked 1060 nm fiber laser. *Biomed. Opt. Express* **7**, 324 (2016).
 8. Bianchini, P., Harke, B., Galiani, S., Vicidomini, G. & Diaspro, A. Single-wavelength two-photon excitation-stimulated emission depletion (SW2PE-STED) superresolution imaging. *Proc. Natl. Acad. Sci. U. S. A.* **109**, 6390–3 (2012).
 9. Teng, K. W., Ishitsuka, Y., Ren, P., Youn, Y. & Deng, X. Labeling proteins inside living cells using external fluorophores for microscopy. *Elife* 1–13 (2016). doi:10.7554/eLife.20378
 10. Andrews, N. L. *et al.* Actin restricts FcεRI diffusion and facilitates antigen-induced receptor immobilization. *Nat. Cell Biol.* **10**, 955–63 (2008).
 11. Linnenbank, H. & Linden, S. High repetition rate femtosecond double pass optical parametric generator with more than 2 W tunable output in the NIR. *Opt. Express* **22**, 18072–18077 (2014).

References

- Ahmed, W. W. & Saif, T. A. modulated by mechanical tension. 1–7 (2014).
doi:10.1038/srep04481
- Albrecht, D., Winterflood, C. & Ewers, H. Dual color single particle tracking via nanobodies. *Methods Appl. Fluoresc.* (2015). doi:10.1088/2050-6120/3/2/024001
- An, J., Kim, D., Dawson, J. W., Messerly, M. J. & Barty, C. P. J. Grating-less, fiber-based oscillator that generates 25 nJ pulses at 80 MHz, compressible to 150 fs. *Opt. Lett.* 32, 2010–2 (2007).
- Andrews, N. L. et al. Actin restricts FcεRI diffusion and facilitates antigen-induced receptor immobilization. *Nat. Cell Biol.* 10, 955–63 (2008).
- Anthony, S. M. & Yu, Y. Tracking single particle rotation : probing dynamics in four dimensions. *Anal. Methods* 7020–7028 (2015). doi:10.1039/C5AY00522A
- Arhel, N. et al. Quantitative four-dimensional tracking of cytoplasmic and nuclear HIV-1 complexes. *Nat. Methods* 3, 817–24 (2006).
- Baumgartl, M. et al. High average and peak power femtosecond large-pitch photonic-crystal-fiber laser. *Opt. Lett.* 36, 244–6 (2011).
- Beaurepaire, E., Oheim, M. & Mertz, J. Ultra-deep two-photon fluorescence excitation in turbid media. *Opt. Commun.* 188, 25–29 (2001).
- Bestvater, F. et al. Two-photon fluorescence absorption and emission spectra of dyes relevant for cell imaging. *J. Microsc.* 208, 108–15 (2002).
- Betzig, E. et al. Imaging Intracellular Fluorescent Proteins at Nanometer Resolution. *Science* (80-.). x, 1642–1646 (2006).
- Bevilacqua, F. et al. In vivo local determination of tissue optical properties: applications to human brain. *Appl. Opt.* 38, 4939–4950 (1999).

- Bianchini, P., Harke, B., Galiani, S., Vicidomini, G. & Diaspro, A. Single-wavelength two-photon excitation-stimulated emission depletion (SW2PE-STED) superresolution imaging. *Proc. Natl. Acad. Sci. U. S. A.* 109, 6390–3 (2012).
- Blanca, C. M. & Saloma, C. Two-color excitation fluorescence microscopy through highly scattering media. *Appl. Opt.* 40, 2722 (2001).
- Brenner, M. H., Cai, D., Swanson, J. A. & Ogilvie, J. P. Two-photon imaging of multiple fluorescent proteins by phase-shaping and linear unmixing with a single broadband laser. *Opt. Express* 21, 17256–64 (2013).
- Cambaliza, M. O. & Saloma, C. Advantages of two-color excitation fluorescence microscopy with two confocal excitation beams. *Opt. Commun.* 184, 25–35 (2000).
- Cang, H., Shan Xu, C. & Yang, H. Progress in single-molecule tracking spectroscopy. *Chem. Phys. Lett.* 457, 285–291 (2008).
- Cang, H., Wong, C. M., Xu, C. S., Rizvi, A. H. & Yang, H. Confocal three dimensional tracking of a single nanoparticle with concurrent spectroscopic readouts. *Appl. Phys. Lett.* 88, 223901 (2006).
- Cang, H., Xu, C. S., Montiel, D. & Yang, H. Guiding a confocal microscope by single fluorescent nanoparticles. *Opt. Lett.* 32, 2729–31 (2007).
- Chen, B.-C. et al. Lattice light-sheet microscopy: Imaging molecules to embryos at high spatiotemporal resolution. *Science* (80-.). 346, 1257998–1257998 (2014).
- Cheng, A., Gonçalves, J. T., Golshani, P., Arisaka, K. & Portera-Cailliau, C. Simultaneous two-photon calcium imaging at different depths with spatiotemporal multiplexing. *Nat. Methods* 8, 139–42 (2011).
- Chong, A., Renninger, W. H. & Wise, F. W. All-normal-dispersion femtosecond fiber laser with pulse energy above 20 nJ. *Opt. Lett.* 32, 2408–10 (2007).
- Chong, A., Renninger, W. H. & Wise, F. W. Properties of normal-dispersion femtosecond fiber lasers. *J. Opt. Soc. Am. B* 25, 140 (2008).

- Chu, J. et al. Non-invasive intravital imaging of cellular differentiation with a bright red-excitable fluorescent protein. *Nat. Methods* 11, 572–8 (2014).
- Cocucci, E., Aguet, F., Boulant, S. & Kirchhausen, T. The first five seconds in the life of a clathrin-coated pit. *Cell* 150, 495–507 (2012).
- Dahan, M. et al. Diffusion dynamics of glycine receptors revealed by single-quantum dot tracking. *Science* 302, 442–5 (2003).
- Dana, H. et al. Sensitive red protein calcium indicators for imaging neural activity. *Elife* 5, 1–24 (2016).
- de Bruin, K. et al. Cellular dynamics of EGF receptor-targeted synthetic viruses. *Mol. Ther.* 15, 1297–305 (2007).
- Deng, Y., Chien, C.-Y., Fidric, B. G. & Kafka, J. D. Generation of sub-50 fs pulses from a high-power Yb-doped fiber amplifier. *Opt. Lett.* 34, 3469–3471 (2009).
- Denk, W., Strickler, J. H. & Webb, W. W. Two-photon laser scanning fluorescence microscopy. *Science* 248, 73–76 (1990).
- Dertinger, T. et al. Two-focus fluorescence correlation spectroscopy: a new tool for accurate and absolute diffusion measurements. *Chemphyschem* 8, 433–43 (2007).
- Domingue, S. R. & Bartels, R. A. Three-photon excitation source at 1250 nm generated in a dual zero dispersion wavelength nonlinear fiber. *Opt. Express* 22, 30777 (2014).
- Drobizhev, M., Makarov, N. S., Tillo, S. E., Hughes, T. E. & Rebane, A. Two-photon absorption properties of fluorescent proteins. *Nat. Methods* 8, 393–399 (2011).
- Drobizhev, M., Tillo, S., Makarov, N., Hughes, T. E. & Rebane, A. Absolute Two-photon Absorption Spectra Of Orange And Red Fluorescent Proteins. *J. Phys. Chem. B* 113, 855–859 (2009).
- Dudley, J. M., Finot, C., Richardson, D. J. & Millot, G. Self-similarity in ultrafast nonlinear optics. *Nat. Phys.* 3, 597–603 (2007).

- Dunn, A. K., Wallace, V. P., Coleno, M., Berns, M. W. & Tromberg, B. J. Influence of optical properties on two-photon fluorescence imaging in turbid samples. *Appl. Opt.* 39, 1194–1201 (2000).
- Durr, N. J. et al. Two-photon luminescence imaging of cancer cells using molecularly targeted gold nanorods. *Nano Lett.* 7, 941–5 (2007).
- Entenberg, D. et al. Setup and use of a two-laser multiphoton microscope for multichannel intravital fluorescence imaging. *Nat. Protoc.* 6, 1500–20 (2011).
- Fakhri, N. et al. High-resolution mapping of intracellular fluctuations using carbon nanotubes. *Science* 344, 1031–5 (2014).
- Fermann, M. E. & Hartl, I. Ultrafast fibre lasers. *Nat. Photonics* 7, 868–874 (2013).
- Friedrich, J., Seidel, C., Ebner, R. & Kunz-Schughart, L. A. Spheroid-based drug screen: considerations and practical approach. *Nat. Protoc.* 4, 309–24 (2009).
- Fujimoto, J. G., Pitris, C., Boppart, S. A. & Brezinski, M. E. Optical Coherence Tomography : An Emerging Technology for Biomedical Imaging and Optical Biopsy 1. *Neoplasia* 2, 9–25 (2000).
- Fujiwara, T., Ritchie, K., Murakoshi, H., Jacobson, K. & Kusumi, A. Phospholipids undergo hop diffusion in compartmentalized cell membrane. *J. Cell Biol.* 157, 1071–81 (2002).
- Gebhardt, J. C. M. et al. Single-molecule imaging of transcription factor binding to DNA in live mammalian cells. *Nat. Methods* 10, 421–6 (2013).
- Gelles, J., Schnapp, B. & Sheetz, M. Tracking kinesin-driven movements with nanometre-scale precision. *Nature* 331, 450–453 (1988).
- Germann, J. A. & Davis, L. M. Three-dimensional tracking of a single fluorescent nanoparticle using four-focus excitation in a confocal microscope. *Opt. Express* 22, 9830–9834 (2014).
- Griffin, E., Odde, D. & Seydoux, G. Regulation of the MEX-5 gradient by a spatially segregated kinase/phosphatase cycle. *Cell* 146, 955–68 (2011).

- Grutzendler, J., Kasthuri, N. & Gan, W.-B. Long-term dendritic spine stability in the adult cortex. *Nature* 420, 812–816 (2002).
- Ha, T. et al. Single-molecule fluorescence spectroscopy of enzyme conformational dynamics and cleavage mechanism. *Proc. Natl. Acad. Sci. U. S. A.* 96, 893–8 (1999).
- Hayakawa, C., Venugopalan, V., Krishnamachari, V. & Potma, E. Amplitude and Phase of Tightly Focused Laser Beams in Turbid Media. *Phys. Rev. Lett.* 103, 43903 (2009).
- Heinze, K. G., Koltermann, a & Schwille, P. Simultaneous two-photon excitation of distinct labels for dual-color fluorescence crosscorrelation analysis. *Proc. Natl. Acad. Sci. U. S. A.* 97, 10377–82 (2000).
- Hell, S. W. et al. Three-photon excitation in fluorescence microscopy. *J. Biomed. Opt.* 1, 71–74 (1996).
- Hell, S. W. Improvement of lateral resolution in far-field fluorescence light microscopy by using two-photon excitation with offset beams. *Opt. Commun.* 106, 19–24 (1994).
- Helmchen, F. & Denk, W. Deep tissue two-photon microscopy. *Nat. Methods* 2, 932–40 (2005).
- Hernández, I. C. et al. Two-Photon Excitation STED Microscopy with Time-Gated Detection. *Sci. Rep.* 1–9 (2016). doi:10.1038/srep19419
- Hinde, E., Cardarelli, F., Digman, M. A. & Gratton, E. In vivo pair correlation analysis of EGFP intranuclear diffusion reveals DNA-dependent molecular flow. *Proc. Natl. Acad. Sci. U. S. A.* 107, 16560–16565 (2010).
- Hofer, M., Fermann, M. E., Haberl, F., Ober, M. H. & Schmidt, a J. Mode locking with cross-phase and self-phase modulation. *Opt. Lett.* 16, 502–504 (1991).
- Horton, N. G. et al. In vivo three-photon microscopy of subcortical structures within an intact mouse brain. *7*, 205–209 (2013).

- Horton, N. G. et al. In vivo three-photon microscopy of subcortical structures within an intact mouse brain. *7*, 205–209 (2013).
- Huang, B., Jones, S. A., Brandenburg, B. & Zhuang, X. Whole-cell 3D STORM reveals interactions between cellular structures with nanometer-scale resolution. *Nat. Methods* *5*, 1047–1052 (2008).
- Ji, N., Magee, J. & Betzig, E. High-speed, low-photodamage nonlinear imaging using passive pulse splitters. *Nat. Methods* *1–6* (2008).
- Juette, M. F. & Bewersdorf, J. Three-Dimensional Tracking of Single Fluorescent Particles with Submillisecond Temporal Resolution. *Nano Lett.* 4657–4663 (2010).
- Juette, M. F., Rivera-Molina, F. E., Toomre, D. K. & Bewersdorf, J. Adaptive optics enables three-dimensional single particle tracking at the sub-millisecond scale. *Appl. Phys. Lett.* *102*, 173702 (2013).
- Karatekin, E. et al. Analysis of Transient Behavior in Complex Trajectories : Application to Secretory Vesicle Dynamics. *91*, 3542–3559 (2006).
- Katayama, Y. et al. Real-time Nanomicroscopy via Three-Dimensional Single-Particle Tracking. *Chemphyschem* *10*, 2458–2464 (2010).
- Kawakami, R. et al. Visualizing hippocampal neurons with in vivo two-photon microscopy using a 1030 nm picosecond pulse laser. *Sci. Rep.* *3*, 1014 (2013).
- Kazmi, S. M. S. et al. Three-dimensional mapping of oxygen tension in cortical arterioles before and after occlusion. *Biomed. Opt. Express* *4*, 1061–73 (2013).
- Khatter, H., Myasnikov, A. G., Natchiar, S. K. & Klaholz, B. P. Structure of the human 80S ribosome. *Nature* (2015). doi:10.1038/nature14427
- Kieu, K., Renninger, W. H., Chong, a & Wise, F. W. Sub-100 fs pulses at watt-level powers from a dissipative-soliton fiber laser. *Opt. Lett.* *34*, 593–5 (2009).
- Kim, D. U. et al. Two-photon microscopy using an Yb(3+)-doped fiber laser with variable pulse widths. *Opt. Express* *20*, 12341–9 (2012).

- Kim, K. H. et al. Multifocal multiphoton microscopy based on multianode photomultiplier tubes. *Opt. Express* 15, 11658–78 (2007).
- Kis-Petikova, K. & Gratton, E. Distance measurement by circular scanning of the excitation beam in the two-photon microscope. *Microsc. Res. Tech.* 63, 34–49 (2004).
- Kobat, D. et al. Deep tissue multiphoton microscopy using longer wavelength excitation. *Opt. Express* 17, 13354–64 (2009).
- Kobat, D., Horton, N. G. & Xu, C. In vivo two-photon microscopy to 1.6-mm depth in mouse cortex. *J. Biomed. Opt.* 16, 106014 (2011).
- Kruglov, V. I., Peacock, A. C., Harvey, J. D. & Dudley, J. M. Self-similar propagation of parabolic pulses in normal-dispersion fiber amplifiers. *J. Opt. Soc. Am. B* 19, 461–469 (2002).
- Kusumi, A., Tsunoyama, T. a, Hirosawa, K. M., Kasai, R. S. & Fujiwara, T. K. Tracking single molecules at work in living cells. *Nat. Chem. Biol.* 10, 524–32 (2014).
- Lagerholm, C., Andreade, D., Clausen, M. & Eggeling, C. Convergence of lateral dynamic measurements in the plasma membrane of live cells from single particle tracking and STED-FCS. *J. Phys. D Appl. Phys.* 50, (2017).
- Lakowicz, J. R., Gryczynski, I., Malak, H. & Gryczynski, Z. Two-Color Two-Photon Excitation of Fluorescence. *Photochem. Photobiol.* 64, 632–635 (1996).
- Lecoq, J. et al. Simultaneous two-photon imaging of oxygen and blood flow in deep cerebral vessels. *Nat. Med.* 17, 893–8 (2011).
- Lee, J. Y., Finkelstein, I. J., Crozat, E., Sherratt, D. J. & Greene, E. C. Single-molecule imaging of DNA curtains reveals mechanisms of KOPS sequence targeting by the DNA translocase FtsK. *Proc. Natl. Acad. Sci. U. S. A.* 109, 6531–6 (2012).
- Lee, K., Cui, Y., Lee, L. P. & Irudayaraj, J. Quantitative imaging of single mRNA splice variants in living cells. *Nat. Nanotechnol.* 9, 474–480 (2014).

- Lefrançois, S., Kieu, K., Deng, Y., Kafka, J. D. & Wise, F. W. Scaling of dissipative soliton fiber lasers to megawatt peak powers by use of large-area photonic crystal fiber. *Opt. Lett.* 35, 1569–71 (2010).
- Lessard, G. a., Goodwin, P. M. & Werner, J. H. Three-dimensional tracking of individual quantum dots. *Appl. Phys. Lett.* 91, 224106 (2007).
- Levi, V., Ruan, Q. & Gratton, E. 3-D particle tracking in a two-photon microscope: application to the study of molecular dynamics in cells. *Biophys. J.* 88, 2919–28 (2005).
- Limpert, J. et al. High-power femtosecond Yb-doped fiber amplifier. *Opt. Express* 10, 628–38 (2002).
- Lin, J. & Spence, D. J. 25.5 fs dissipative soliton diamond Raman laser. *Opt. Lett.* 41, 1861–4 (2016).
- Lin, M. Z. et al. Autofluorescent Proteins with Excitation in the Optical Window for Intravital Imaging in Mammals. *Chem. Biol.* 16, 1169–1179 (2009).
- Linnenbank, H. & Linden, S. High repetition rate femtosecond double pass optical parametric generator with more than 2 W tunable output in the NIR. *Opt. Express* 22, 18072–18077 (2014).
- Liu, C. et al. 3D single-molecule tracking using one- and two-photon excitation microscopy. *Proc. SPIE* 8950, 1–9 (2014).
- Liu, C. et al. Improving z-tracking accuracy in the two-photon single-particle tracking microscope. *Appl. Phys. Lett.* 107, 153701 (2015).
- Liu, Y. et al. Segmentation of 3D Trajectories Acquired by TSUNAMI Microscope : An Application to EGFR Trafficking. *Biophysj* 111, 2214–2227 (2016).
- Lowe, A. R. et al. Selectivity mechanism of the nuclear pore complex characterized by single cargo tracking. *Nature* 467, 600–3 (2010).
- Mahou, P. et al. Multicolor two-photon tissue imaging by wavelength mixing. *Nat. Methods* 9, 815–818 (2012).

- Mahou, P., Vermot, J., Beaurepaire, E. & Supatto, W. Multicolor two-photon light-sheet microscopy. *Nat. Methods* 11, 600–601 (2014).
- Mason, T. G. & Weitz, D. A. Optical Measurements of Frequency-Dependent Linear Viscoelastic Moduli of Complex Fluids. *Phys. Rev. Lett.* 74, 1250–1253 (1995).
- Matsuzaki, M., Honkura, N., Ellis-Davies, G. C. R. & Kasai, H. Structural basis of long-term potentiation in single dendritic spines. *Nature* 429, 761–766 (2004).
- Maus, M. et al. An experimental comparison of the maximum likelihood estimation and nonlinear least-squares fluorescence lifetime analysis of single molecules. *Anal. Chem.* 73, 2078–86 (2001).
- McHale, K., Berglund, A. J. & Mabuchi, H. Quantum dot photon statistics measured by three-dimensional particle tracking. *Nano Lett.* 7, 3535–9 (2007).
- Meroz, Y. & Sokolov, I. M. A toolbox for determining subdiffusive mechanisms. *Phys. Rep.* 573, 1–29 (2015).
- Millard, A. C., Fittinghoff, D. N., Squier, J. A., Müller, M. & Gaeta, A. L. Using GaAsP photodiodes to characterize ultrashort pulses under high numerical aperture focusing in microscopy. *J. Microsc.* 193, 179–181 (1999).
- Moneron, G. & Hell, S. W. Two-photon excitation STED microscopy. *Opt. Express* 17, 14567–73 (2009).
- Murtagh, M., Lin, J., Mildren, R. P., McConnell, G. & Spence, D. J. Efficient diamond Raman laser generating 65 fs pulses. *Opt. Express* 23, 15504–15513 (2015).
- Myong, S., Rasnik, I., Joo, C., Lohman, T. M. & Ha, T. Repetitive shuttling of a motor protein on DNA. *Nature* 437, 1321–5 (2005).
- Negrean, A. & Mansvelder, H. D. Optimal lens design and use in laser-scanning microscopy. *Opt. Express* 5, 11277–11291 (2014).
- Nishimura, N. et al. Targeted insult to subsurface cortical blood vessels using ultrashort laser pulses: three models of stroke. *Nat. Methods* 3, 99–108 (2006).

- Oheim, M., Beaufepaire, E., Chaigneau, E., Mertz, J. & Charpak, S. Two-photon microscopy in brain tissue: parameters influencing the imaging depth. *J. Neurosci. Methods* 111, 29–37 (2001).
- Papadopoulos, D. N. et al. Generation of 63 fs 4.1 MW peak power pulses from a parabolic fiber amplifier operated beyond the gain bandwidth limit. *Opt. Lett.* 32, 2520–2522 (2007).
- Park, H. Y. et al. Visualization of dynamics of single endogenous mRNA labeled in live mouse. *Science* 343, 422–4 (2014).
- Patting, M., Wahl, M., Kapusta, P. & Erdmann, R. Dead-time effects in TCSPC data analysis. *Proc. SPIE* 6583, 658307-658307–10 (2007).
- Perillo, E. P. et al. Deep and high-resolution three-dimensional tracking of single particles using nonlinear and multiplexed illumination. *Nat. Commun.* 6, 7874 (2015).
- Perillo, E. P. et al. Deep in vivo two-photon microscopy with a low cost custom built mode-locked 1060 nm fiber laser. *Biomed. Opt. Express* 7, 324 (2016).
- Perillo, E., Liu, Y.-L., Liu, C., Yeh, H.-C. & Dunn, A. K. Single particle tracking through highly scattering media with multiplexed two-photon excitation. *SPIE BiOS* 9331, 933107 (2015).
- Prakash, R. et al. Two-photon optogenetic toolbox for fast inhibition, excitation and bistable modulation_S1. *Nat. Methods* 9, 1171–9 (2012).
- Pyenta, P. S., Schwille, P., Webb, W. W., Holowka, D. & Baird, B. Lateral Diffusion of Membrane Lipid-Anchored Probes before and after Aggregation of Cell Surface IgE-Receptors. *J. Phys. Chem. A* 8310–8318 (2003).
- Quentmeier, S., Denicke, S., Ehlers, J.-E., Niesner, R. A. & Gericke, K.-H. Two-Color Two-Photon Excitation Using Femtosecond Laser Pulses. *J. Phys. Chem. B* 112, 5768–5773 (2008).

- Robinson, T. et al. Analysis of DNA binding and nucleotide flipping kinetics using two-color two-photon fluorescence lifetime imaging microscopy. *Anal. Chem.* 86, 10732–10740 (2014).
- Rust, M. J., Bates, M. & Zhuang, X. imaging by stochastic optical reconstruction microscopy (STORM). 3, 793–795 (2006).
- Sackmann, E., Ra, J. O. & Heinrich, D. Temporal Analysis of Active and Passive Transport in Living Cells. 248103, 1–4 (2008).
- Sahl, S. J., Leutenegger, M., Hilbert, M., Hell, S. W. & Eggeling, C. Fast molecular tracking maps nanoscale dynamics of plasma membrane lipids. *Proc. Natl. Acad. Sci.* 107, 6829–6834 (2010).
- Sakadžić, S. et al. Two-photon high-resolution measurement of partial pressure of oxygen in cerebral vasculature and tissue. *Nat. Methods* 7, 755–9 (2010).
- Saxton, M. J. & Jacobson, K. Single-particle tracking: applications to membrane dynamics. *Annu. Rev. Biophys. Biomol. Struct.* 26, 373–99 (1997).
- Schönle, A. & Hell, S. W. Heating by absorption in the focus of an objective lens. *Opt. Lett.* 23, 325 (1998).
- Schrandt, C. J., Kazmi, S. M. S., Jones, T. a & Dunn, A. K. Chronic monitoring of vascular progression after ischemic stroke using multiexposure speckle imaging and two-photon fluorescence microscopy. *J. Cereb. Blood Flow Metab.* 35, 933–942 (2015).
- Shank, C. V., Fork, R. L., Yen, R., Stolen, R. H. & Tomlinson, W. J. Compression of femtosecond optical pulses. *Appl. Phys. Lett.* 40, 761–763 (1982).
- Shav-Tal, Y. et al. Dynamics of single mRNPs in nuclei of living cells. *Science* 304, 1797–800 (2004).
- Shcherbo, D. et al. Far-red fluorescent tags for protein imaging in living tissues. *Biochem. J.* 418, 567–574 (2009).

- Sigismund, S. et al. Clathrin-mediated internalization is essential for sustained EGFR signaling but dispensable for degradation. *Dev. Cell* 15, 209–19 (2008).
- Simson, R., Erin, D. & Jacobson, K. Detection of Temporary Lateral Confinement of Membrane Proteins Using Single-Particle Tracking Analysis. *Biophys. J.* 69, 989–993 (1995).
- Spence, D. J., Granados, E. & Mildren, R. P. Mode-locked picosecond diamond Raman laser. *Opt. Lett.* 35, 556–558 (2010).
- Spiess, E., Bestvater, F., Heckel-Pompey, A. & K. -photon excitation and emission spectra of the green fluorescent protein variants eCFP,. *J. Microsc.* 217, 200–204 (2005).
- Spille, J.-H., Kaminski, T., Königshoven, H.-P. & Kubitscheck, U. Dynamic three-dimensional tracking of single fluorescent nanoparticles deep inside living tissue. *Opt. Express* 20, 19697–707 (2012).
- Stosiek, C., Garaschuk, O., Holthoff, K. & Konnerth, A. In vivo two-photon calcium imaging of neuronal networks. *Proc. Natl. Acad. Sci. U. S. A.* 100, 7319–24 (2003).
- Sun, C.-K. et al. Higher harmonic generation microscopy for developmental biology. *J. Struct. Biol.* 147, 19–30 (2004).
- Taira, K., Hashimoto, T. & Yokoyama, H. Two-photon fluorescence imaging with a pulse source based on a 980-nm gain-switched laser diode. *Opt. Express* 15, 2454–2458 (2007).
- Takasaki, K. T., Ding, J. B. & Sabatini, B. L. Live-cell superresolution imaging by pulsed STED two-photon excitation microscopy. *Biophys. J.* 104, 770–7 (2013).
- Tang, S., Liu, J., Krasieva, T. B., Chen, Z. & Tromberg, B. J. Developing compact multiphoton systems using femtosecond fiber lasers. *J. Biomed. Opt.* 14, 30508 (2009).

- Teng, K. W., Ishitsuka, Y., Ren, P., Youn, Y. & Deng, X. Labeling proteins inside living cells using external fluorophores for microscopy. *Elife* 1–13 (2016).
doi:10.7554/eLife.20378
- Theer, P., Hasan, M. T. & Denk, W. Two-photon imaging to a depth of 1000 microm in living brains by use of a Ti:Al₂O₃ regenerative amplifier. *Opt. Lett.* 28, 1022–4 (2003).
- Thompson, M. a, Lew, M. D., Badieirostami, M. & Moerner, W. E. Localizing and tracking single nanoscale emitters in three dimensions with high spatiotemporal resolution using a double-helix point spread function. *Nano Lett.* 10, 211–8 (2010).
- Thompson, R. E., Larson, D. R. & Webb, W. W. Precise nanometer localization analysis for individual fluorescent probes. *Biophys. J.* 82, 2775–83 (2002).
- Tischbirek, C., Birkner, A., Jia, H., Sakmann, B. & Konnerth, A. Deep two-photon brain imaging with a red-shifted fluorometric Ca²⁺ indicator. *Proc. Natl. Acad. Sci. U. S. A.* 112, 1–6 (2015).
- Trägårdh, J. et al. Two-Color, Two-Photon Imaging at Long Excitation Wavelengths Using a Diamond Raman Laser. *Microsc. Microanal.* 1–5 (2016).
- Tsai, P. S. et al. Ultra-large field-of-view two-photon microscopy. *Opt. Express* 23, 1825–1829 (2015).
- Ulbrich, M. H. & Isacoff, E. Y. Subunit counting in membrane-bound proteins. *Nat. Methods* 4, 319–21 (2007).
- Unruh, J. R. et al. Two-photon microscopy with wavelength switchable fiber laser excitation. *Opt. Express* 14, 9825–9831 (2006).
- van den Broek, B., Ashcroft, B., Oosterkamp, T. H. & van Noort, J. Parallel nanometric 3D tracking of intracellular gold nanorods using multifocal two-photon microscopy. *Nano Lett.* 13, 980–6 (2013).

- Wang, C., Qiao, L., Mao, Z., Cheng, Y. & Xu, Z. Reduced deep-tissue image degradation in three-dimensional multiphoton microscopy with concentric two-color two-photon fluorescence excitation. *J. Opt. Soc. Am. B* 25, 976 (2008).
- Wang, Q. & Moerner, W. E. Single-molecule motions enable direct visualization of biomolecular interactions in solution. *Nat. Methods* 11, 555–8 (2014).
- Warren, S. C. et al. Rapid Global Fitting of Large Fluorescence Lifetime Imaging Microscopy Datasets. *PLoS One* 8, (2013).
- Warrier, A. M. et al. Highly efficient picosecond diamond Raman laser at 1240 and 1485 nm. *Opt. Express* 22, 3325–3333 (2014).
- Wells, N. P. et al. Time-resolved three-dimensional molecular tracking in live cells. *Nano Lett.* 10, 4732–7 (2010).
- Welsher, K. & Yang, H. Multi-resolution 3D visualization of the early stages of cellular uptake of peptide-coated nanoparticles. *Nat. Nanotechnol.* 9, 198–203 (2014).
- Wirtz, D. Particle-tracking microrheology of living cells: principles and applications. *Annu. Rev. Biophys.* 38, 301–26 (2009).
- Xiao, F., Wang, G. & Xu, Z. Superresolution in two-color excitation fluorescence microscopy. *Opt. Commun.* 228, 225–230 (2003).
- Xu, C. & Wise, F. W. Recent advances in fibre lasers for nonlinear microscopy. *Nat. Photonics* 7, 875–882 (2013).
- Xu, C., Guild, J., Webb, W. & Denk, W. Determination of absolute two-photon excitation cross sections by in situ second-order autocorrelation. *Opt. Lett.* 20, 2372 (1995).
- Xu, K., Zhong, G. & Zhuang, X. Actin, Spectrin, and Associated Proteins Form a Periodic Cytoskeletal Structure in Axons. *Science* (80-.). 452–457 (2013).
- Yildiz, A. et al. Myosin V walks hand-over-hand: single fluorophore imaging with 1.5-nm localization. *Science* 300, 2061–5 (2003).

Yokoyama, H. et al. Two-photon bioimaging utilizing supercontinuum light generated by a high-peak-power picosecond semiconductor laser source. *J. Biomed. Opt.* 12, 54019 (2007).

Zinter, J. P. & Levene, M. J. Maximizing fluorescence collection efficiency in multiphoton microscopy. *J. Opt. Soc. Am. B* 19, 5480–5486 (2011).

Zipfel, W. R., Williams, R. M. & Webb, W. W. Nonlinear magic: multiphoton microscopy in the biosciences. *Nat. Biotechnol.* 21, 1369–77 (2003).